THESIS

USING IN SITU COSMOGENIC RADIONUCLIDES TO CONSTRAIN MILLENIAL SCALE DENUDATION RATES AND CHEMICAL WEATHERING RATES ON THE COLORADO FRONT RANGE

Submitted by

Jonathan Garber

Department of Geosciences

In partial fulfillment of the requirements

For the Degree of Master of Science

Colorado State University

Fort Collins, Colorado

Summer 2013

Master's Committee:

Advisor: Ellen Wohl

Sara Rathburn
Jeffrey Niemann
Clifford Riebe

ABSTRACT

USING IN SITU COSMOGENIC RADIONUCLIDES TO CONSTRAIN MILLENIAL SCALE DENUDATION RATES AND CHEMICAL WEATHERING RATES ON THE COLORADO FRONT RANGE

Multiple authors have delineated the Colorado Front Range (COFR) landscape into distinct elevational zones with respect to contemporary geomorphologic processes, landscape development, and sediment dynamics in bedrock canyons. Several studies have estimated denudation rates using rates of post-fire erosion, alpine soil erosion, beaver dam sedimentation, and cosmogenic tor erosion, but comparison is limited due to differences in the time scale captured by different measurements. I address this gap by using cosmogenic ^{10}Be to measure denudation rates in three process domains: flat Front Range summits, five unglaciated watersheds above the latest Pleistocene terminal glacial moraine, and five watersheds below the moraine.

Two paired bedrock outcrop and soil samples were taken on flat summits in Rocky Mountain National Park. Bedrock samples were taken from a low-lying bedrock outcrop and large boulder with accompanying colluvial soil samples from the surrounding surface. Fluvial sediment was collected for ^{10}Be analysis from the outlets of 10 watersheds. I also conducted soil surveys in each basin to examine relationships between physical characteristics, depth of regolith, and hillslope position. Low outcrops and regolith from a glacial col saddle are denuding at four times the rate of previously published tor data, while regolith from a summit flat is eroding much more slowly and at similar rates to summit flats elsewhere in the Rockies.

Basins are denuding at similar rates to cosmogenic radionuclide (CRN)-derived, basin-averaged rates in the Boulder Creek watershed and show no difference between hydroclimatic process domains. Basin morphometric parameters are not significantly related to these denudation rates. The denudation rates span into the Late Pleistocene, and are an order of magnitude lower than Holocene sedimentation rates. This implies a large increase in Holocene COFR erosion in basins not glaciated during the Pleistocene, and could reflect stronger monsoonal rain systems generating more debris flows. Denudation rates increase with the percent of coarse material processed, alluding to grain size dependency of CRN concentrations. This pattern appears to be affected by valley confinement at the sampling location. Regolith is deeper and shows a more typical pattern along hillslope fall lines on upper basins, implying that weathering rates may be higher and disturbance less frequent.

Bulk geochemistry of bedrock and regolith on Big Horn Flats contains the signal of Zr-rich dust inputs that may indicate the importance of Mojave Desert source areas during the Pleistocene. Millennial-scale weathering rates assuming no dust deposition (5.8 – 10 t/km^2yr) are similar to modern estimates, but uncertainty from dust inputs cannot be constrained.

ACKNOWLEDGEMENTS

I never would have been able to accomplish this research without the generosity, patience, and expertise of many individuals. I would first like to thank my advisor, Dr Ellen Wohl, of picking me for this project, and guiding me along the way. Next I would like to thank Dr. Cliff Riebe, who let me use his state of the art facilities, and for giving me a lot of guidance. Many others up in Laramie were also instrumental in giving me advice, training, and a place to stay including: Cliff and Chicory, Bill and Jill, Will White, Jesse Hahm, Claire Lukens, Robert Mahon, and Tracy O’Flanigan. I would like to thank my field assistant, Matt Sparacino, for digging ~240 soil pits for me. I also received field help from Kyle Grimsley, Nick Sutfin, Amanda White and Field Dog Suki. Many people helped me in the lab at CSU including Matt, Amanda, Olivia, Eve, Eric, Emily, and Jen. Finally I would like to thank the CSU Fluvial Family and friends in Fort Collins and beyond for helping me through a wild and sometimes stressful journey, and my parents for always stoking my interest in science.

TABLE OF CONTENTS

ABSTRACT……………………………………………………………………………………………..ii

ACKNOWLEDGEMENTS………………………………………………………………………….iv

1 Introduction…………………………………………………………………………….……1
- 1.1 Process domains of the Front Range…………………………………………………4
- 1.2 Conceptual model……………………………………………………..……………..6
- 1.3 Short term erosion rates of the COFR……………………………………………….9
  - 1.3.1 Summits…………………………………………………………………………9
  - 1.3.2 High elevation zones…………………………………………………………10
  - 1.3.3 Low elevation zones…………………………………………………………11
- 1.4 The role of regolith……………………………………………………………………13
- 1.5 Chemical denudation and dust deposition on the COFR…………………………14

2 Objectives and Hypotheses…………………………………………………………...16

3 Study Area and Physiography…………………………………………………………...18
- 3.1 Climate and vegetation……………………………………………………………..18
- 3.2 Underlying lithology…………………………………………………………………18

4 Methods…………………………………………………………………………………….20
- 4.1 CRN methodology…………………………………………………………………..20
  - 4.1.1 CRN field sampling…………………………………………………………20
  - 4.1.2 CRN sample preparation……………………………………………………..21
- 4.2 CRN sample analysis …………………………………………………………………22
  - 4.2.1 Snow production scaling……………………………………………………..24
  - 4.2.2 Production and attenuation scaling: peak samples………………………26
  - 4.2.3 Production and attenuation scaling: basins………………………………..27
  - 4.2.4 Error from radioactive decay…………………………………………………28
- 4.3 Soil sampling…………………………………………………………………………...29
- 4.4 Bulk geochemistry……………………………………………………………………..30
- 4.5 Basin morphometry……………………………………………………………………32
- 4.6 Statistics………………………………………………………………………………...34

5 Results……………………………………………………………………………………..35
- 5.1 Cosmogenic radionuclides…………………………………………………………35
  - 5.1.1 Peak bedrock and regolith samples………………………………………...35
  - 5.1.2 Basin-averaged denudation rates…………………………………………...36
- 5.2 Estimation of fire disturbance recurrence interval…………………………………37
- 5.3 Testing Hypothesis 1…………………………………………………………………38
- 5.4 Basin morphometry data……………………………………………………………...38

5.4.1 Testing Hypothesis 2: Basin Morphometry……39
5.4.2 Sample grain size……39
5.5 Testing Hypothesis 2: Regolith Depth Patterns……40
5.5.1 Regolith grain size……41
5.6 Big Horn Flats geochemistry……42

6 Discussion……47
6.1 Peak denudation……47
6.2 Basin denudation, morphometry, and regolith……48
6.3 Basin-averaged denudation in context……51
6.4 Chemical weathering and dust deposition……53

7 Conclusion……55
7.1 Future Work……56

8 Tables……57

9 Figures……69

10 Works Cited……88

Appendix A Supplemental CRN Data……102

Appendix B Supplementary Snow depth data……111
B.1 Snow Data……111

Appendix C Additional regolith data visualization and scripts……122

Appendix D Supplemental Morphometric Parameter Data……126

Appendix E Bulk Geochemical Data……128

1 Introduction

The origin of the modern Rocky Mountain landscape dates back 65 million years to the Laramide Orogeny, when the shallow subduction of the Farallon plate thrust Neoproterozoic basement on top of Mesozoic sediments, leaving a landscape much like the Tibetan plateau (Gregory and Chase, 1994). During the Eocene, a broad pediment was formed on the flanks of the ancestral Rockies, relics of which are mapped today as the Rocky Mountain or Subsummit surface (Scott and Taylor, 1986; Anderson et al., 2006). Apatite fission track data on the Colorado Front Range imply 2.3 km of denudation since the beginning of the Cenozoic, implying a long term denudation rate of 35m/Myr over the history of the modern range (Kelley and Chapin, 2004). Fission track data (Pazzaglia and Kelley, 1998) have also shown that high rates of exhumation occurred between the end of the Laramide Orogeny and the beveling of the Rocky Mountain surface. The peak surfaces largely have been preserved because they were on the footwall of the extensional faulting of the Rockies in the Miocene, which produced horst and graben structures that form the park features (i.e., North, Estes, and South Park). During the late Neogene and Quaternary, both glacial cycles at the headwaters, and fluvial incision from the trunk streams, have driven COFR landscape evolution, and many workers have constrained the rates and patterns of these landscape drivers.

Stratigraphic datums have been used to quantify fluvial incision and landscape evolution of the COFR and the Rocky Mountains during the Late Cenozoic (Dethier, 2001; McMillan et al., 2006). McMillan et al. (2006) used sedimentary units to reconstruct the basin fill surface and incision depth of major streams bounding the COFR, as well as determining age constraints for sedimentary and volcanic units on top of the basin fill sequence to constrain surface and abandonment ages and Quaternary incision rates of the Rocky Mountains and Colorado Plateau. Dethier (2001) used Lava Creek B tephra localities deposited on fluvial gravels and terraces to constrain fluvial incision rates. Both of these studies found increased incision with proximity to active tectonic regions (Yellowstone Hotspot and the Rio Grande Rift) and mantle velocity anomalies, giving evidence of local tectonic and epeirogenic controls on late Cenozoic incision. Dethier (2001) also attributed increased glacial and snowmelt runoff during the late Quaternary as driving the regional incision pulse. These studies show that both epeirogenic and climatic activity may have driven the exhumation of the Denver basin and COFR bedrock canyons.

Cosmogenic radionuclides (CRNs) have been used to constrain late Pleistocene fluvial incision and basin fill histories on the COFR. Dühnforth et al. (2012) measured CRN concentrations of terrace soils on the flanks of the COFR in order to constrain incision on tributaries to the South Platte River. CRN concentrations show that the lower terrace flights are much younger than previously extrapolated ages assuming steady incision. Terrace abandonment ages also correspond with intense interglacial periods in the global climate record, showing that downstream fluvial incision is linked to decreases in sediment supply and increases in discharge from glacial retreat. CRN age constraints of younger fill terraces in Middle Boulder Creek Canyon (Schildgen et al., 2002) show a similar pattern of initial fill, and abandonment following the onset of glacial retreat. This flight of terraces showed abandonment associated with Pinedale and Bull Lake glacial retreat. These studies show that, although the onset of Late Cenozoic incision may be due to epeirogenic uplift, shorter wavelength cycles of incision are predominantly due to glacio-fluvial coupling.

Upstream of these incising canyons, Pleistocene glaciers have left a significant imprint on the headwaters of the COFR, leaving glacial headwalls, U shaped valleys, and glacial drift deposits from Pinedale, Bull Lake, and earlier glaciations (Madole et al., 1998). ^{10}Be concentrations in glacial moraine boulders and glacial polish also document the retreat of Pinedale glaciation in the Green Lakes valley of the COFR (Dühnforth and Anderson, 2011).

The retreat began at ~18 kyr and glacier mass balance models of the retreat show that the moisture regime was relatively constant during the glacial cycles on the COFR, and most of the glaciation was driven by temperature depression.

Despite knowledge of how the general characteristics of Cenozoic geologic history have shaped the contemporary Rocky Mountain landscape, relatively little is known of rates of Quaternary landscape change. The focus of this thesis is quantifying rates of Quaternary landscape change for selected components of the landscape within the Colorado Front Range in order to understand the role of contemporary geomorphic processes and geomorphic history on denudation rates of the COFR.

In an attempt to link glacial, fluvial, and Rocky Mountain surface evolution on the COFR, Anderson et al. (2006) created a numerical model for long term (10^6 yr) landscape evolution by separating the landscape into three 1-dimensional components: (i) flat summit surfaces, (ii) valleys above the terminal moraine, and (iii) bedrock canyons. Anderson et al. (2006) inferred that the summit surfaces are eroding at an extremely low rate and are mostly disconnected from the rest of the landscape. The only significant erosion comes from backwearing of glacial headwalls into the surface, and the only major contribution to downslope geomorphic processes that these surfaces make is windblown snow onto glaciers, therefore increasing input to the glacial mass balance on the lee side of the peaks, and increasing glacial erosion. Below these surfaces are valleys that are intermittently glaciated, with nearly vertical headwalls that flow into valleys that are over-flattened by glacial erosion, and periodically discharge large amounts of water and sediment when glaciers retreat. Below the moraines, the streams are influenced by pulses of water and sediment from glaciers upstream, as well as base level lowering from South Platte incision making its way upstream. This has caused cycles of incision and aggradation within the bedrock canyons observed by Schildgen et al. (2002). The model effectively shows the interactions between the high alpine surfaces, glacial valleys, and fluvial canyons, but is based on inference rather than extensive quantification of process rates, and fails to take into account the hillslope-stream coupling due to the model's one-dimensionality. Long term erosion rates of the type developed in this thesis can help verify and calibrate the model to better understand the long term landscape evolution of the COFR. Data collected for this thesis quantify the denudation rates of the summit surfaces, and basins adjusting to glacial and fluvial incision, to understand the three-dimensional interplay of these landscape drivers.

1.1 Process domains of the Front Range

The landscape of the COFR is governed by an orographic hydroclimatic gradient in which average annual precipitation increases with altitude and average temperature decreases. This altitudinal gradient influences the vegetation, soils, and hydrology of the Front Range, as well as contemporary geomorphic processes. Workers have tried to divide the landscape into elevational zones where similar geomorphic processes are dominant.

Caine (1984) reviewed previous studies of geomorphic process studies on the COFR. These studies focused on processes in the Indian Peaks region of the Front Range (glaciers and rock glaciers, talus, mass wasting, surface erosion). Using the available data, he separated the Indian Peaks region into four morphodynamic zones: high alpine peaks, alpine tundra, subalpine forest, and montane forest, each with a unique set of geomorphic processes. The relative distributions of processes are illustrated in Table 1.

In the high alpine zone, coarse sediment transport is dominated mostly by episodic rockfall and talus development. This zone has few fine sediment or geochemical outputs. The lower alpine zone consists of low relief surfaces and interfluves above the tree line, and is characterized by more soil development, mass wasting, and surface erosion from snowmelt runoff. Below the treeline is the subalpine forest, which Caine interpreted as the least active zone, with infrequent catastrophic mass wasting events resulting from forest fires with recurrence intervals greater than a century. The montane forest zone has suffered severe anthropogenic change, and therefore the natural geomorphic processes are hard to distinguish. However, Caine interpreted this zone as having high rates of chemical weathering and fluvial erosion from high intensity precipitation events. This framework suggests that the morphodynamic zones follow the altitudinal gradients in vegetation and climate. However, Caine (1984) included the caveat that there is still great spatial heterogeneity of processes in each zone, which complicates differentiation. The studies reviewed in Caine's (1984) summary focused on very short time scales, and little is known about how these process domains affect the long term denudation of the COFR.

Montgomery (1999) first defined the concept of process domains as an alternative explanation to the river continuum concept of the influence of geomorphology on ecosystems. He defined a process domain as a portion of the watershed where a distinct suite of geomorphic processes that are a function of the lithology, topography, and climate govern the types of riverine and riparian habitat: changes in these suites are abrupt. Process domains are analogous to Caine's morphodynamic zones, but Montgomery made a more explicit connection between physical processes and biotic communities.

Wohl (2010) applied the process domain concept to the upper Cache la Poudre basin on the COFR, inferring that the process domains reflect differences in sediment dynamics in each zone. Sediment dynamics can be defined as the processes by and rates at which sediment is generated, stored, and delivered to the stream. Wohl (2010) separated the upper watershed into eight zones, four above (glacial), and four below (fluvial) the terminal moraine (~2300 m elevation). First-order channels are defined as colluvial hollows (glacial) and ephemeral streams (fluvial). Higher-order valleys are separated into confined, partially confined, and unconfined as a measure of hillslope coupling, and space to store sediments on floodplains and terraces. Confined valleys generally have much coarser sediment, since hillslopes directly input sediment through debris flows and rockfall. The main difference between the glacial and fluvial zones is the hydroclimatology, where the glacial zone is almost exclusively dominated by the snowmelt flood, and the fluvial zone is subject to flash floods and rare high intensity rainfall events that can cause catastrophic floods. Wohl (2010) concluded that these process domains are useful at locating places in bedrock canyons that may store a large amount of sediment, as well as the relative frequency of sediment entrainment and distance moved. However, this was largely a conceptual paper with no quantification based on actual measurements of sediment dynamics because such measurements do not yet exist at time scales longer than a few years. There has been no effort to assess potential differences in long term surface lowering rates – sediment production -- between these domains, for example.

In this study, I am using the three zones in the Anderson et al. (2006) model as "process domains." Peak surfaces are dominated by periglacial weathering, with low amounts of surface erosion. Unglaciated basins above the Pinedale terminal moraine are responding to glacial base level fall, and have a colder, wetter modern climate. Basins below the terminal moraine are responding to bedrock canyon incision, and are warmer and drier (Grimm et al., 1995; Veblen and Donnegan, 2005). These three units of landscape show great variability in their landscape history and contemporary processes, but little is known of how this variability affects the erosion of each group over longer timescales.

1.2 Conceptual model

Climate and tectonics are the two major driving factors of denudation in mountain ranges, (Montgomery and Brandon, 2002; Willett et al., 2006) (Figure 1). Tectonic uplift causes rapid fluvial incision (Burbank et al., 1996). Orogenic processes also can increase rock erodibility through brittle deformation and jointing. Climate change causes base level lowering through glaciation, downstream incision and aggradation from glacial outwash cycles, and sea level change (Schildgen et al., 2002; Reusser et al., 2004; Dühnforth and Anderson, 2011; Dühnforth et al., 2012). Climate also has a first-order control on the precipitation and temperature regime in the system, which directly affects the production of regolith, including freeze-thaw weathering and chemical weathering, as well as precipitation-induced disturbances (flash floods, debris flows). Base level lowering can increase basin relief as well as hillslope gradients across erosional process thresholds to increase denudation rates. CRN-derived incision rates and basin-averaged denudation rates have been used to document landscape response to tectonic (Burbank et al., 1996; Montgomery and Brandon, 2002; Binnie et al., 2006) and glacial incision (Stock et al., 2009). Tributary stream gradients also increase in order to stay connected with the trunk stream, and CRN denudation rates have been shown to respond to channel steepness index in quickly eroding catchments responding to incision (Safran et al., 2005; Ouimet et al., 2009). Incision erodes banks and colluvial hollows, therefore releasing regolith from storage. The studies above give evidence of the drivers and response to CRN basin-averaged denudation, but few studies have documented how and why basin erosion responds in that way. In order to understand basin-averaged processes responding to tectonics or climate, one must first delineate the processes that go into denuding a basin.

In order to denude a landscape, rock must first be converted into transportable material via physical and chemical weathering, and incorporated into the active regolith. Rates and forms of physical and chemical weathering depend on climate (hydrology, temperature, biological processes) and geology (mineralogy, texture, fracture sets), as well as the thickness of overlying material. Humped soil production implies that weathering increases as regolith depth increases to a point where enough regolith has accumulated that regolith production begins to decrease (Carson and Kirkby, 1973). Weathered saprolite and colluvium are introduced or recycled into the active regolith by biologic mixing processes (i.e., burrowing, tree throw), as well as physical mixing processes (i.e., frost heave) and surface erosion. Active regolith is transported to and stored on hillslopes, colluvial hollows, and valley bottoms. This regolith must then be entrained and transported out of the basin. The processes required to denude a basin can be separated into categories of production, storage, and transport of regolith (Figure 2). Complex intra and inter-unit interactions occur between these processes, and the driving forces on the landscape can also change the processes with time and space. CRN concentrations in fluvial sediment reflect all of these three groups of processes, as well as memory of past change in the factors driving denudation (Granger et al., 1996; Parker and Perg, 2005; Heimsath, 2006; Schaller and Ehlers, 2006).

The main driving force on the COFR during the scope of this study is climate. Uplift by isostatic rebound is assumed to be constant. Paleoglacial studies have shown that climate change on the COFR significantly affects the temperature regime, but not the amount of precipitation during the Pleistocene glacial periods (Brugger, 2006; Dühnforth and Anderson, 2011). Models of frost weathering on the Front Range have yielded increased weathering and transport rates due to cooler glacial climates (Anderson et al., 2012). However, climate-induced denudation fluctuations imprint themselves most effectively on CRN concentrations only if the denudation rates are high, the period of climate-induced denudation fluctuations are long, and the amplitudes are small (Schaller and Ehlers, 2006).

The conceptual framework used in this thesis research assumes that (i) climate is the main driving force on the COFR during the Quaternary, (ii) spatial variations in climate are effectively delineated based on elevation, and (iii) quantification of Quaternary denudation rates can therefore be differentiated based on process domains of summit surfaces and glacial (above 2300 m elevation) and fluvial (below 2300 m elevation) basins. Table 2 illustrates the details of how the conceptual model outlined can be applied to the three process domains that are the foci of this study.

1.3 Short term erosion rates of the COFR

This section summarizes estimates and measurements of erosion and denudation rates in the literature. Mass erosion rates have been converted to denudation rates assuming a rock density of 2.65 g/cm^3 and sedimentary deposit density of 1.8 g/cm^3. Actual rates, timescales, and elevations of studies are provided in Table 3. The following descriptions of the studies are organized by summit, above glacial limit, and below glacial limit units that are guiding this thesis. Studies range from single season soil trap studies to CRN-derived denudation rates.

1.3.1 Summits

Several studies have constrained erosion rates in the summit and high alpine zone. Bovis and Thorn (1981) measured short term (1 summer) alpine interfluve erosion rates (using Gerlach sediment traps) in three land cover types, dry tundra, tundra meadows, and late-lying snow patches. The majority of the soil loss came from hollows with late-lying snow patches. Small et al. (1997; 1999) constrained erosion rates for bedrock tors, and regolith on western US summits, including some COFR summits, using ^{10}Be and ^{26}Al CRN concentrations (Table 3). These are maximum erosion rates, assuming that the tors eroded at a steady state. Chipping lengths of talus surrounding the outcrop were measured to model the error from episodic denudation. Small et al. (1999) sampled regolith on summit flats of the Wind River Range, Wyoming. The CRN concentration profile was homogenous and showed that regolith was well mixed. These two studies give two end-member time scales for denudation on the highest points of the COFR landscape. However, the short time span of Bovis and Thorn (1981) means that the rate is wrought with uncertainty, and the measurement of tors on the COFR landscape presents a minimum surface lowering rate, since the relief between the tor crest and the summit surface implies the separation of geomorphic processes.

1.3.2 High elevation zones

Polvi and Wohl (2012) used ground penetrating radar (GPR) and ^{14}C dating from boreholes and augering to estimate beaver-induced sedimentation rates of 0.5 – 1.4 mm/yr (over 4000 yr). This provides a lower-bound estimate of denudation rate above the study area of Beaver Meadows in Rocky Mountain National Park (RMNP), from the assumption that all of the sediment eroded was deposited by beaver-dam-induced aggradation over that time period. Menounos (2000) constrained the debris flow chronology at Sky Pond in RMNP. He used ^{14}C geochronology, lichenometry, and soil development to constrain debris flow deposit age. He found that debris flow activity was highest during the mid-Holocene and a warmer climate, and postulated that warmer climate increased the occurrence of monsoon moisture and convective storm triggers for debris flows. The sedimentation of Beaver Meadows can be considered a minimum denudation rate constraint, assuming that all of the sediment transported out of the Beaver Brook watershed was trapped in the beaver meadows. Although beaver meadow sedimentation is a significant part of this landscape, this assumption may be unfounded. The debris flow sedimentation study may only be relevant in glaciated basins, which were not included in this study.

CRN geochemistry has been used in the Sangre de Cristo Range in Southern Colorado to calculate the denudation rates from a small alpine unglaciated wash. Using ^{10}Be to ^{26}Al ratios in cave sediment, along with ^{10}Be concentrations in modern stream sediment, Refsnider (2010) calculated modern and paleo denudation rates of Marble Mountain in the Sangre de Cristo Range. Spanish Gulch is underlain by sedimentary rock, and cave sediment showed an order of magnitude increase in denudation rates from the Pliocene (~5 Myr BP) (Table 3) to the present. This study presents an exciting look into Late Neogene denudation, but the small spatial scale of the study limits its comparison.

1.3.3 Low elevation zones

Moody and Martin (2001) measured post-fire erosion rates on two COFR basins below the terminal moraine within the montane forest zone after the Buffalo Creek wild fire. They measured interrill erosion with Gerlach sediment traps, rill erosion with field measurements and aerial photos, and in-channel erosion and aggradation by calculating stream cross sectional area change. Sediment rating curves were also constructed post-fire using Helley-Smith bedload samplers and suspended load samplers. Measured post-fire erosion rates were up to 240 times the background sediment yield. These background rates are from sediment rating data for the Buffalo Creek watershed pre-fire (Williams and Rosgen 1989). The majority of sediment came from low-order stream/drainage erosion, and as much as 67% of the eroded sediment was deposited in and around the higher-order channels in the watershed. The hillslope relaxation time was < 2 yrs, and both basins were close to returning to background sediment yields after the 4 years of the study. This study shows the significance of forest fire disturbance on lower montane zone geomorphology. However, there are few constraints on longer term denudation rates in this region to put these disturbances into context with the landscape evolution of the COFR, as well as estimate long time scale recurrence intervals of these events. Dethier and Lazarus (2006) constrained basin-averaged denudation rates using ^{10}Be CRN geochronology on small unglaciated basins on the COFR, Laramie, and Medicine Bow Ranges. They found that denudation rate correlated weakly with mean basin slope and relief.

These studies report denudation rates over a range of timescales (10^0-10^3) in various morphodynamic zones of the COFR. However, the variety of timescales, methods, and processes quantified limits direct comparison of denudation between process domains. Bovis (1978) set Gerlach traps in alpine tundra, subalpine forest, and montane forest environments in order to compare soil erosion between morphodynamic zones. Soil loss over 1 year was an order of magnitude higher in the montane forest and alpine tundra environments than the subalpine forest. This is one of the few studies that attempted to directly compare erosion rates between defined process domains using a single method. However, the limited period of measurements and area observed limited the power of these comparisons. Short term denudation rate measurements usually contain high amounts of uncertainty and generally are less accurate due to failure to measure large magnitude events and periodicity of sediment transport and storage. CRN-derived denudation rates generally span a long enough time to incorporate extreme events and periodicity of sediment transport, and provide a better way to compare the denudation rates of these three zones.

Despite the issues with comparing rates across time scales and measurement methods, a pattern emerges from the reported measurements that helps to drive this study. Denudation rates of peak tors and summit regolith production rates are significantly slower than any other rates measured in the COFR, and rates of fluvial incision that span well into the Pleistocene show the fastest rates of incision. The CRN basin-averaged denudation rates are between these two extremes, but no attempts have been made to contrast these measurements between basins above and below the terminal moraine. Shorter timescale measurements and observations show that basins below the terminal moraine lying mostly within the montane ecosystem are subject to more frequent disturbance from wild fires (Veblen and Donnegan, 2005) and more intense convective storms (Grimm et al., 1995), while many other studies have noted that the subalpine forest zone, lying mostly above the terminal moraines, has the least geomorphic activity. Above tree line, mass wasting processes from avalanches and debris flows as well as periglacial processes dominate, but the flat peak surfaces are largely detached from the rest of the landscape. With this pattern in mind, my research will attempt to compare the long term denudation rates between summit flats, basins above the Pleistocene terminal moraine which contain both subalpine forest and alpine tundra, and basins below the moraine that flow into bedrock canyons and contain mostly upper montane forest land cover type. CRN-derived denudation rates integrate all of the denudation processes of these domains and I allow me to discern the effect of long term climate and landscape history on the landscape evolution of the COFR.

1.4 The role of regolith

When small alpine and subalpine basins on the COFR are considered in the context of the conceptual model above, one can see how denudation rates may vary through time and with elevation (Figure 1). Of the three categories of processes that denude landscapes (Figure 2), the pattern of regolith storage is the most accessible unit to measure, and is important because it is the intermediary between production and transport. Regolith depth, texture, and chemistry have been theorized to respond to denudation and landscape evolution (Birkeland et al., 2003). The amount of soil development and horizonation (Birkeland et al., 2003) has been linked to denudation rates and landscape stability on the COFR. Models of disturbance and soil development have postulated that longer recurrence intervals of large disturbances will allow hillslope sequences of soils to form (Tonkin and Basher, 1990). Studies are just beginning to understand the influence of base level change on hillslope regolith patterns. Incision has been shown to affect characteristics such as soil thickness and texture (Yoo et al., 2011). Reduction in incision at the hillslope base can generate thicker regolith at the bottom of hillslopes, and decrease chemical weathering in depositional zones (Yoo et al., 2009). These studies show that the physical and chemical nature of regolith can be used to elucidate current processes and past landscape change. Therefore, it is important to understand regolith patterns as a link to the processes that denude a catchment.

1.5 Chemical denudation and dust deposition on the COFR

Significant contemporary solute flux data have been collected from streams in the alpine and subalpine zones of the COFR (Clow and Sueker, 2000). However, most previous studies emphasize the lack of understanding in the COFR. Sueker et al. (2001) used solute concentration and stream gage data to estimate the chemical weathering rates of different minerals, and compared these to the basin physical characteristics. This study elucidated some surprising trends, such as that the amount of vegetation cover is inversely correlated with chemical weathering, most likely due to uptake by plants, and the relative rate of physical weathering that exposes new mineral faces to weathering. This goes against the basic idea that soil cover and vegetation increase chemical weathering rates (Ritter et al., 2002). Dethier and Lazarus (2006) calculated weathering rates below the glacial limit in the Boulder Creek watershed using CRN basin-averaged erosion rates, short term solute fluxes, density measurements, and weathering depth interpretations from well logs. With this information, they constructed a box model to estimate the production of saprolite and grus. They found that the formation of grus (1.6 – 6.4 cm/kyr) from saprolite balances the CRN-derived denudation rates, but the conversion of bedrock into saprolite (0.3-1.6 cm/kyr) is much lower. Sueker et al. (2001) were limited to the temporal span of the solute record, while Dethier and Lazarus (2006) had to make assumptions about well drilling records to estimate saprolite thicknesses. These studies provide insight in the chemical denudation processes of the COFR, but have yet to constrain the long term chemical weathering rates of the mountain range.

The rates and patterns of chemical weathering on the COFR are further complicated by significant dust inputs. Clow and Sueker (2000) suggested that much of the dissolved calcium ions observed in stream geochemistry measurements are derived from eolian-deposited calcite, since bedrock in the region is relatively low in calcite. Thorn and Darmody (1985) collected eolian dust input and deflation on snow fields and lag surfaces on the COFR and postulated that sources could be both locally derived and distant, such as the Mount St. Helens volcano. Ley et al. (2004) measured dust deposition rates over 1 year on the Green Lakes Valley, COFR using dust traps. They measured a mineral dust deposition rate of 5.2 t/km^2/yr. The short timescale of these measurements limit their accuracy, in that yearly climate fluctuations can significantly affect yearly dust deposition rates (Reheis and Kihl, 1995). Muhs and Benedict (2006) compared the bulk geochemistry of the silt and sand fractions of COFR moraine soil to silt fractions of North and Middle Park alluvium, and found that these localities could be a potential source of much of the eolian silt. In the San Juan Mountains, soil geochemistry is shown to be significantly governed by eolian inputs, with much of the chemical weathering acting on the eolian-sourced minerals. None of these studies have attempted to constrain the rate of eolian deposition over long timescales on the COFR. Ferrier et al. (2011) presented a framework to estimate eolian deposition rates with CRN-derived soil production rates, and the elemental geochemistry of the rock, soil, and dust source. With this method, I can constrain the dust deposition rate on COFR peaks and assess the relative importance of dust and bedrock inputs of elements into the COFR ecosystem.

2 Objectives and Hypotheses

The geomorphic history of the COFR landscape has created a variety of landforms that vary by elevation. The hydroclimatic gradient with elevation generates a diverse set of geomorphic processes acting on a relatively homogenous bedrock substrate. Some workers have organized the COFR landscape into process domains, based on geomorphic history as well as hydroclimatology. Others have constrained denudation rates in some of these zones, although over different timescales and using different methods that prevent a robust comparison between domains. The research proposed here will address these gaps by: systematically comparing denudation rates across process domains using ^{10}Be CRN geochemistry; relating denudation rates to basin geomorphic attributes; and assessing the relationship between denudation and process domain and how that relationship propagates over millennial timescales.

My primary objectives are to (1) use ^{10}Be cosmogenic radionuclide (CRN) geochronology to constrain denudation rates in three process domains of the COFR: (i) summit outcrops and regolith, (ii) fluvial sediment from basins above the terminal moraine (2,300 m elevation), and (iii) fluvial sediment from basins below the moraine, and (2) quantitatively compare basin morphology and the nature of hillslope regolith between the three process domains. I collected 14 samples of ^{10}Be and measured soil development on two low bedrock outcrops and adjacent regolith, and ten basins, five above and five below the terminal moraine. I measured basin-averaged morphologic parameters using 10 m DEMs, ArcGIS, and MATLAB. Thirty regolith depth measurements were taken along six transects in each basin to characterize regolith depth patterns. With these data, I test the following hypotheses:

H1. The three process domains are eroding at different rates, such that CRN-derived long-term denudation rates will differ significantly among the three sample populations.

H2. Differences in long-term denudation between the two lower-elevation process domains are reflected in significantly different basin morphology and regolith depth.

H3. The majority of silt-size particles in Rocky Mountain Surface regolith are deposited from eolian processes.

3 Study Area and Physiography

3.1 Climate and vegetation

The COFR climate is in many ways a product of the landscape itself. The COFR is on the lee side of the Southern Rockies relative to the prevailing westerlies, and in the rain shadow of much of the western-sourced moisture. The rain shadow effect of the COFR, along with its position in the continental interior far from maritime moisture sources, leads to a semi-arid climate. The main sources of precipitation include summer convective precipitation from the Gulf of Mexico and summer monsoon flow from Gulf of California moisture, as well as Pacific-sourced cyclonic weather systems during the fall, winter, and spring. The flanks of the COFR also create an orographic gradient where mean annual precipitation increases and temperature decreases with increasing elevation (Barry, 1973) (Figure 3). However, rainfall intensity peaks at 2300 m for summer convective precipitation because air masses moving northwest from the Gulf of Mexico run out of moisture as they proceed upslope (Grimm et al., 1995).

The spatial heterogeneity of climate on the COFR orographic climate pattern creates unique zones of vegetation communities. Veblen and Donnegan (2005) separate these into distinct zones of vegetation, with forest communities trending from semi arid ponderosa pine in the lower montane zone through Douglas fir and sub alpine forests dominated by Engelmann spruce. Above the treeline, alpine tundra species thrive, with a few krummholz trees near the tree line (Figure 3).

3.2 Underlying lithology

The bedrock lithology underlying most of the basins in the study area is part of the suite of Paleoproterozoic metamorphic rocks, including knotted biotite – muscovite mica schists, which are interbedded with mica-poor quartzo-feldspathic schists. There are also Paleoproterozoic trondjhemite intrusions in Big Thompson Canyon, which are plagioclase-rich and leucocratic, with ~5% biotite. The Longs Peak Granite (locality of Silver Plume Granite) also underlies some study sites, and is a microcline-rich monzogranite with trace amounts of biotite. Quaternary alluvial and colluvial surficial deposits lie at the base of hillslopes and in valley bottoms. The Longs Peak Granite can also include mapped and unmapped metamorphic xenoliths, as well as some pegmatitic intrusions. Although these rocks show a range of petrologic diversity, workers have commonly assumed that these rocks have similar erosional strengths (Ehlen and Wohl, 2002). However, shear zones have been mapped in areas of wider valleys and shallower dipping slopes, showing that structural geology may have some control on topographic evolution (Ehlen and Wohl, 2002; Wohl, 2008).

The soil sequences in this region vary significantly with elevation and aspect. Ustolls and Cryolls (A/Ej,Bw,C) dominate on south-facing aspects and Cryalfs (O/E/Bt/Bw) dominate on north-facing aspects in the montane zone (1700 – 2700 m). At higher elevations, aspect plays less of a role and Cryelfs (A/Bw/C) dominate (Birkeland et al., 2003).

The watersheds and peaks I sampled for CRN geochemistry all lie in Rocky Mountain National Park or the Arapaho Roosevelt National Forest. The Trail Ridge peak site (TR) is located on the saddle of Forest Canyon Pass above the head of the Big Thompson River. The Bighorn Flats peak site (BHF) is located northwest of Ptarmigan Pass on the southern edge of the Big Horn Flat section of the Rocky Mountain surface. Sampled basins lie within the Big Thompson, Cache la Poudre, and North St Vrain watersheds. Catchments above the terminal moraine were unglaciated during the last glacial cycle (Madole et al., 1998). All basins are low order and have areas between ~2 – 10 km^2.

4 Methods

4.1 CRN methodology

The following sections describe the steps I took to select sampling locations, collect samples, and prepare the samples for measurement of ^{10}Be concentrations

4.1.1 CRN field sampling

Ten fluvial, 2 bedrock, and 2 colluvial samples were collected in Fall 2011. I sampled low outcrops and boulders in order to measure rates that are geomorphically connected to the summit surface. I collected bedrock samples using a rock hammer and chisel. Care was taken to sample from the top of the outcrop, and only chips from the top 4 cm were kept for subsequent analysis. I measured strike and dip to adjust the cosmogenic production rate before damaging the outcrop. Using a clinometer or Brunton compass inclinometer, I measured topographic shielding for each outcrop sample. This involved crouching down to bring my eye level to the same elevation with the outcrop surface and measuring the angle to the top of the horizon at 45 degree azimuth intervals around a compass rose. Chipping lengths were estimated by measuring the intermediate diameter of chips around the outcrop if evidence of episodic erosion was apparent (i.e., the presence of many chips). Soil pits were dug adjacent to the outcrop/boulder, and the assumption was made that the colluvial soil was well mixed, similar to Small et al.'s (1999) observations. Colluvial samples were collected on randomly selected parts of the surface using a trowel.

Fluvial samples were collected at basin outlets of small basins in RMNP, Big Thompson Canyon, and Cache la Poudre Canyon. I chose basins that were easily accessible (i.e., entire basin was in RMNP or national forest), between 1 – 10 km^2 in area, and between ~35 and 45%

slope. I sampled five unglaciated basins above the Pleistocene terminal moraine in RMNP, and 5 basins below the terminal moraine flowing into the Big Thompson and Cache la Poudre Canyons. Using a trowel, I used a random walk method to collect fluvial sediment over a ~5 m reach of the stream, taking care that no significant tributary entered that reach. Care was taken to avoid collecting sediment from bank failure to avoid bias from potentially unmixed bank sediment.

4.1.2 CRN sample preparation

I dried regolith and fluvial sediment samples in an oven at ~90 degrees C, and estimated mineral composition through visual estimation with a hand lens. The sample was then split using a splitter, to create two geochemically identical samples. I used a clean bucket and tap water rinse, and stirring rod to float off organics of organic-heavy sediment and colluvial soil. After drying again, I separated fluvial and colluvial samples into four size classes using stainless steel sieves and a ro-tap sieve shaker. Large grains were crushed with a clean or jaw crusher in order to more easily fit in the pulverizing mill. Grain size fractions were ground to sand (between 250 – 500 µg in intermediate diameter) using a pulverizing mill. Samples were then recombined to have the same mass distribution of grain sizes, in order to minimize grain size controls on ^{10}Be concentrations.

I used standard procedures to purify the sample into quartz and prepare ^{10}Be targets for measurement at the Purdue PRIME Laboratory Accelerator Mass Spectrometer (AMS) (Kohl and Nishiizumi, 1992). In order to remove unwanted minerals, organic impurities and meteoric ^{10}Be, I performed HNO_3 leaches, magnetic and paramagnetic separation, froth flotation, 5% HF-HNO_3 leaches, heavy mineral separation, and 1% HF-HNO_3 ultrasonic leaches. I examined aliquots of sample for purity by measuring %Al, a proxy for quartz purity, using an atomic absorption spectrometer or an inductively coupled plasma mass spectrometer.

Once the sample was purified, I added a known mass of ^{9}Be carrier and dissolved the quartz-concentrated HF and HNO_3 in a water bath. Once the sample was completely dissolved, I converted the sample into chlorides through HF, H_2SO_4, and HCL dry downs. I added NaOH to samples dissolved in HCl in order to raise the pH of the sample and precipitate Fe and Ti. I ran samples through 5 ml cation exchange columns to separate Be from other cations, then precipitated and dried down $Be(OH)_2$. To convert the samples to BeO, I fired them for 1 hour at 900 degrees C. I then mixed the samples with niobium powder and packed them into accelerator mass spectrometer (AMS) targets. Samples were then sent to the PRIME lab AMS to measure the $^{10}Be/^{9}Be$ atom ratio.

4.2 CRN sample analysis

AMS measurements are converted from the ratio to concentrations using the mass of quartz dissolved, the mass of ^{9}Be added, and blank measurement. First, the number of ^{9}Be atoms in the spike is calculated:

$$m_{sp} * \rho_{sp} * C_{9Be} = m_{9Be} \qquad \text{(Equation 1)}$$

Where m_{sp} is the mass of the spike added, ρ_{sp} is the density of the spike, C_{9Be} is the concentration of ^{9}Be in the spike, and m_{9Be} is the mass of ^{9}Be added to the sample from the spike. This is converted to atoms:

$$\frac{m_{9Be}*Av}{Molw_{9Be}} = At_{9Be} \qquad \text{(Equation 2)}$$

Where Av is Avogadro's constant ($6.02*10^{23}$ atoms/mol), $Molw_{9Be}$ is the molecular weight of ^{9}Be (9.01318 g/mol), and At_{9Be} is the total number of atoms of ^{9}Be added to the sample. The concentration of ^{10}Be in the sample can then be calculated:

$$N = \frac{At_{9Be}(R_s - R_b)}{m_s} \qquad \text{(Equation 3)}$$

Where R_s and R_b are ratios of $^{10}Be/^{9}Be$ from the AMS for the sample and blank, respectively, m_s is the mass of quartz, and N is the concentration of ^{10}Be in the quartz (atoms/g). This concentration can be used to calculate regolith and bedrock outcrop denudation rates.

$$N = \sum \frac{P}{\lambda + \frac{\rho D}{\Lambda}} \qquad \text{(Equation 4)}$$

Where P is the production rate, λ is the radioactive decay constant ($1/\tau_{10Be}$), τ_{10Be} is the radioactive mean life of ^{10}Be, ρ is the density of the rock, D is the denudation rate, and Λ is the attenuation length of ^{10}Be production. For basin-averaged denudation rates, radioactive decay must be neglected, and the production rates have to be scaled to the entire basin (Granger and Riebe, 2007):

$$N = \sum \frac{\langle P \rangle \Lambda}{\rho \langle D \rangle} \qquad \text{(Equation 5)}$$

Where <D> is the basin-averaged denudation rate, and <P> is the basin-averaged production rate. These denudation rate models assume steady denudation rates over timescales long enough to exhume rock that has been completely shielded from cosmogenic production. Therefore, there is a timescale attached to these rates that is related to the Λ of the production reactions:

$$T = \frac{\Lambda}{\rho D} \qquad \text{(Equation 6)}$$

Where T is the timescale that the rate spans. In this study, the Λ for spallation (160 g/cm^2) was used for all timescale calculations.

If no erosion is assumed, then exposure ages (T_e) of bedrock surfaces can be calculated with the following equation:

$$N(T_e) = N_{in} e^{-\lambda T_e} + \sum \frac{P}{\lambda} * (1 - e^{-\lambda T_e}) \qquad \text{(Equation 7)}$$

Where N_{in} is the inherited radionuclide concentration from previous transport, assumed to be 0 for bedrock exposure.

These functions are summations of all production reactions of the radioactive nuclide. For ^{10}Be production in quartz, this includes spallogenic production, fast muon production, slow muon production, negative muon production, and thermal neutron production (Gosse and Phillips, 2001). The production rate for each of these reactions scales with atmospheric pressure (Stone, 2001), latitude (Dunai, 2000), and significant snow cover (Gosse and Phillips, 2001; Schildgen et al., 2005). P and Λ also scale with slope of the surface and topographic shielding along the horizon (Dunne et al., 1999).

4.2.1 Snow production scaling

Persistent snow pack can shield quartz crystals from secondary cosmogenic rays and retard the production of ^{10}Be in underlying quartz from spallation and muonogenic reactions (Gosse and Phillips, 2001; Schildgen et al., 2005). Snow shielding correction factors for CRN production can be calculated assuming a mean annual snow depth and density, or snow water equivalent (SWE) (Gosse and Phillips, 2001). In order to constrain SWE depths over time, workers have used Snotel snowpack data (http://www.wcc.nrcs.usda.gov/snotel/SNOTEL-brochure.pdf, 2012), as well as process-based conservation of energy snow pack modeling over cosmogenic (10^3 – 10^5 yr) time scales (Schildgen et al., 2005). Other studies have ignored or assumed that snow cover is an insignificant scaling factor for cosmogenic production.

The Colorado Front Range accumulates deep snow packs each winter, which show large variability in space and time. With increasing precipitation and decreasing temperature gradients with elevation (Barry, 1973), one might expect to see mean annual SWE increasing with elevation. Because of the altitudinal spread of the ridgetops and basins in this study, using one proximal Snotel station to characterize all of the data would potentially lead to unrealistically low snow shielding on the peaks, and unrealistically high snow shielding in the lower basins. A more effective approach would be to construct a relationship between SWE and elevation to more accurately predict snow shielding of CRN production.

In order to address this problem, I have taken mean annual estimates for 10 Snotel sites in Larimer, Boulder, and Grand Counties that are close to the study region to create a regression between SWE and elevation. All but one of these Snotel sites fall in the Poudre, Big Thompson, and St Vrain drainage basins. Lake Irene is in the upper CO river basin (Map 1). In order to calculate mean annual SWE, daily historic SWE values were acquired from each Snotel (http://www.wcc.nrcs.usda.gov/snow/, Data in Appendix B). I used the mean of each year's monthly mean to calculate the yearly mean for that year:

$$\overline{SWE}_{yr} = 1/12 \sum_{i=1}^{12} \overline{SWE}_{month} \quad \text{(Equation 8)}$$

I defined mean SWE at the Snotel station as the mean of all the yearly means in the record:

$$\overline{SWE}_{tot} = \frac{1}{n} \sum_{i=1}^{n} \overline{SWE}_{yr} \quad \text{(Equation 9)}$$

Where n is the total number of record years for that Snotel. I also calculated variance (s^2), standard deviation (s), and the coefficient of variance as a percentage of the mean (s/SWE), for total mean SWE in order to estimate variability and uncertainty in the data sets.

I performed a linear regression between the mean SWE and elevation using the ten sites, with elevation as the predictor and SWE as the response variable. The unweighted linear regression using the LinearModel.fit function in Matlab produced an R^2 value of 0.7126. The residuals showed a cone shape. The Breusch-Pagan (BP) statistic was calculated to test for homoscedacity of variances (6.334), which is greater than the alpha = 0.05, n-1 = 9 X^2 statistic = 3.325 (Ott and Longnecker, 2010). Therefore, a weighted least squares regression was calculated using variance as a weight. Variance varies widely, but % variance and % standard deviation of the mean seem to be relatively similar. The weighted least squares regression passed the BP test with a BP statistic of 0.102, but there still is a somewhat conical shape in the residual plot. The Snotel data contain a wide variety in numbers of years on record. This could potentially be a problem since Snotel sites with few years of record might not be a representative sample of snow patterns through time, in that they do not contain points from both swings of the decadal oscillations. Variance shows no relationship with number of observations or elevation and %Cv shows a weak inverse relationship with number of records, which may be in part due to outliers. Linear best fit lines generated in Excel show the trends and correlation coefficients (Appendix B). Because of the lack of relationship between uncertainty, the number of observations, and elevation, I decided to use the unweighted linear regression between SWE and elevation to scale ^{10}Be production rates (Figure 5).

4.2.2 Production and attenuation scaling: peak samples

Bedrock and peak regolith sample production rates were scaled to calculate denudation rates. Latitude and longitude were calculated from field GPS points, and elevations were extracted from 10 m DEMs as a proxy for atmospheric pressure. For each bedrock sample, inclinometer measurements of the horizon were used to calculate topographic shielding (Dunai, 2000) (< 2%). The SWE linear model described above was used to calculate mean annual SWE for each site.

Shielding factors, latitude, longitude, elevation, concentration, and standard were input into the CRONUS model (Balco et al., 2008) to calculate denudation rates and exposure ages (Appendix A). The CRONUS model scales the production rate to latitude (Dunai, 2000), as well as atmospheric pressure, using elevation and longitudinal climate data. The model also propagates the AMS measurement uncertainty through subsequent calculations. Abundant coarse talus surrounding the Trail Ridge outcrop suggested episodic erosion, so I measured 100 clast intermediate diameters as “chipping lengths” to calculate episodic erosion uncertainty using the Small et al. (1997) model.

4.2.3 Production and attenuation scaling: basins

Because production scales nonlinearly with snow depth, elevation and slope, using basin average parameters for these values to scale nuclide production could significantly bias estimates (Granger and Riebe, 2007). Therefore, in order to scale P and Λ more accurately, basins were delineated using 10 m DEMs and production rates for each 10 m pixel in the basin were scaled using elevation, SWE, and slope (Dunai, 2000), which was calculated using the topotoolbox gradient8 function (Schwangart and Kuhn, 2010). I calculated mean latitude for each basin from a 10 m grid. P was not scaled to latitude for each pixel because the empirical relationship is relatively insensitive to small changes in latitude (Dunai, 2000). Mean annual precipitation (MAP) was calculated from USGS StreamStats (Capesius and Stephens, 2009), which uses the PRISM model. This was used to calculate a chemical erosion factor (CEF) for each basin (Riebe and Granger, 2012), which scales the denudation rate for quartz enrichment due to chemical weathering. CEF is a function of MAP using a linear model, so a basin-averaged MAP can be used and calculation of CEFs for each pixel is unnecessary. The coarse spatial resolution of the PRISM model (800 m) also limits the calculation of CEF for each pixel.

For these calculations, uncertainty from the AMS measurements, as well as prediction intervals from the SWE and CEF linear models, must be incorporated in the calculations. Because mean annual SWE and MAP are correlated via elevation, these uncertainties cannot be analytically propagated through the calculations. I used Monte Carlo simulations to avoid this caveat and estimate $\langle D \rangle$ and T using the following equation:

$$\langle D \rangle = \left(\frac{P_{sp}(L,Z,\theta,\widetilde{SWE})\Lambda_{sp}^{*}(\theta)+P_{m1}(L,Z)\Lambda_{m1}+P_{m2}(L,Z)\Lambda_{m2}+P_{fm}(L,Z)\Lambda_{fm}}{\rho_{rock}}\right) * \widetilde{N_{10Be}} * \widetilde{CEF} \qquad \text{(Equation 10)}$$

Variables with tildes are varied for each trial. Each simulation consisted of 500 trials to estimate a basin-averaged denudation rate and associated time span. The simulation randomly selected a ^{10}Be concentration from a Gaussian distribution between the error bounds of the analytical uncertainty, and CEFs from a Gaussian distribution between the 95% prediction intervals for each trial. For each DEM pixel, the simulation randomly selected a mean annual SWE depth for each trial from a Gaussian distribution between the 95% prediction intervals of the linear model. Latitude (Dunai, 2000), elevation (Stone, 2000), and slope scaling (Dunne et al., 1999) remained constant for each trial. Fast and slow muon reactions were scaled to elevation (Rossi, 1948) and latitude (Dunai, 2000). Snow is insignificant for muon production reactions, because the Λ/ρ values are two orders of magnitude larger than SWE. The means and standard deviations for each Monte Carlo simulation were reported and used for further analysis (Figure 6).

4.2.4 Error from radioactive decay

The assumption of no radioactive decay in basin average CRN yields artificially high denudation rates, and the extent of bias is a function of P and T of the rate. In order to estimate the uncertainty from radioactive decay, I used equation 8 to calculate concentrations for denudation rates between 10 and 40 mm/kyr, with given production rates. I then calculated denudation rates assuming that the basin was a steadily eroding bedrock surface (equation 4):

$$0 = \left(\frac{P_{sp}^{*}}{\lambda+\frac{\rho\langle D_{\lambda}\rangle}{\Lambda_{sp}^{*}}} + \frac{P_{m1}}{\lambda+\frac{\rho\langle D_{\lambda}\rangle}{\Lambda_{m1}}} + \frac{P_{m2}}{\lambda+\frac{\rho\langle D_{\lambda}\rangle}{\Lambda_{m2}}} + \frac{P_{fm}}{\lambda+\frac{\rho\langle D_{\lambda}\rangle}{\Lambda_{fm}}}\right) - N_{10Be} \qquad \text{(Equation 11)}$$

I used the Matlab function lsqnonlin to converge on a solution for $\langle D_{\lambda} \rangle$ using nonlinear least squares curve fitting. Curves of % error from radioactive decay versus denudation rate were calculated using the basin-averaged production rates from the Monte Carlo simulations of basins with highest and lowest mean elevations, as well as the median elevation basin of each group. The calculations ignored CEF. This analysis gives an estimate of the percent over-prediction of denudation rate for basin-averaged denudation rates.

4.3 Soil sampling

During the summer of 2012, I returned to the basins to conduct hillslope regolith surveys. I sampled three transects of 10 regolith pits each, five along the left bank hillslope and five along the right bank hillslope (Figure 7). Transects were evenly spaced along the mainstem of the stream, judged to be representative hillslopes of the basin, and of a feasible length to sample. I laid out the transects as straight lines along the fall line from the stream to the local divide, which was a ridge, a plunging intermediate ridge, or a local bedrock tor with significant relief in a plunging divide. I dug regolith pits at the divide, and at 0.2, 0.4, 0.6, and 0.8 times the hillslope length from the divide. This strategy was utilized to characterize the toposequence of regolith. I used horizontal hillslope lengths calculated from UTM GPS coordinates of the ridge and the channel in order to map pit locations. For smaller, less forested hill slopes, a laser range finder and compass were used to locate soil pits. For longer transects, I calculated UTM coordinates for each soil pit along a horizontal line between the ridge and stream. At each soil pit location, I measured local slope, aspect, regolith depth (h_R), type and thickness of understory and tree vegetation, local (10^0 m) slope morphology, underlying material, landform, types and depths of profile layers, and evidence of disturbances (Table 6). Photos were also taken of each site and pit. I collected ~0.5 kg samples of the soil for grain size analysis.

I measured grain size distributions on a subset of soil by dry sieving. Soils were first dried overnight in an oven at ~90 degrees C. These samples were then geochemically split using a riffle splitter. Sieve aperture openings were spaced every 1 φ from -4 to 4 φ. Gradistat V8 (Blott and Pye, 2001) Excel Visual Basic worksheet calculated grain size statistics using weights recovered from each sieve.

4.4 Bulk geochemistry

I collected 10 surface regolith (Figure 8C) samples and 3 bedrock float samples from within ~20m of the Big Horn Flats sampling site for x-ray fluorescence spectrometry (XRF) bulk geochemical measurements. In order to just sample fresh bedrock, I cut float samples with a rock saw and chipped off the weathering rinds on the sides of the cut slices with a chisel and hammer. I then crushed the fresh bedrock samples with a hammer and a cast iron plate. Crushed rock and soil samples were geochemically split with a riffle splitter three times into a ~50 g aliquot. I pulverized samples into powder using a shatterbox. In order to burn off organics and excess water, I fired the powdered samples in a Thermoline Furnace at ~550° C for >12 hours. I created pellets for XRF trace element analysis by mixing ~4 g of powder with a binding agent, and pressing it into a pellet.

The XRF analysis returned the concentrations of major and trace elements in the rocks and soil. Assuming that an element is chemically immobile, such as zirconium and titanium, I calculated the dimensionless mass transfer coefficient ($\tau_{j,w}$) from the parent rock to the soil (Brimhall and Dietrich, 1987; Anderson et al., 2002)

$$\tau_{j,w} = \frac{C_{j.w}C_{i.p}}{C_{i.w}C_{j.p}} - 1 \qquad \text{(Equation 12)}$$

Where $C_{j,w}$ and $C_{j,p}$ are the concentrations of an element in the weathered and parent material, respectively, and $C_{i,w}$ and $C_{i,p}$ are the concentrations of an immobile element in the weathered and parent material, respectively. Positive values of $\tau_{j,w}$ quantify the amount of enrichment that an element has due to preferential chemical weathering of other elements, or due to the influx from another source (i.e., dust). Negative values of $\tau_{j,w}$ quantify the relative decrease in the concentration of the element, or its chemical weathering intensity. Combined with CRN-derived denudation rates or soil production rates, the chemical weathering rates can be constrained (Riebe et al., 2003):

$$W_j = E(C_{j.p} - C_{j,w}\frac{C_{i.p}}{C_{i.w}}) \qquad \text{(Equation 13)}$$

Where W_j is the chemical mass flux rate of element j, and E is the mass erosion rate or soil production rate per unit area derived from CRN geochemistry (D or <D>*ρ_r). This method assumes that the parent rock geochemistry is relatively uniform and there are no eolian inputs. The eolian input assumption is obviously violated at our study site, so I used dust chemistry from the literature (Muhs and Benedict, 2006; Sweeney et al., 2007; Reheis et al., 2009) and the method set forth in Ferrier et al. (2011) to calculate dust deposition rates (P_d):

$$P_d = \frac{P_r f_d}{1-f_d} \qquad \text{(Equation 14)}$$

Where P_r is the CRN-derived soil production rate (D* ρ_r) and f_d is the fraction of the regolith parent material that is dust. f_d can be calculated assuming two immobile elements and knowing their concentrations in rock, dust, and regolith.

$$f_d = \left(\frac{C_{i1,p}}{C_{i1,w}} - \frac{C_{i2,p}}{C_{i2,w}}\right) * [\frac{C_{i1,p}-C_{i1,d}}{C_{i1,w}} - \frac{C_{i2,p}-C_{i2,d}}{C_{i2,w}}]^{-1} \qquad \text{(Equation 15)}$$

Where C is the concentration of immobile elements, the subscripts *i1* and *i2* correspond to immobile elements 1 and 2, respectively, and the subscripts *p*, *w*, and *d* correspond to parent rock, weathered material (regolith or soil) and dust, respectively. This method assumes one known dust source, and the denominator of the equation must be sufficiently small to be precise.

4.5 Basin morphometry

I extracted basin morphometric parameters for each basin from a 10 m DEM of the study region downloaded from the USGS seamless server. Stream profiles were also extracted in USGS StreamStats (Capesius and Stephens, 2009) down to the canyon outlets. Outlet points were GPS data from field collection. Basins were delineated using outlet points, 10 m DEMs, and the Hydrology Toolbox in ArcGIS 10. DEMs were clipped to the drainage basins using the Extract by mask tool, and converted into ASCII files for use in Matlab.

I calculated mean hillslope gradient (HS) in two ways, using ArcGIS and Matlab. Using Topotoolbox, I generated a 10 m resolution gradient matrix, and extracted possible stream pixels by deleting all of the pixels with accumulation raster (Acc) values greater than 100, meaning that the drainage area of that pixel is greater than 10^4 m^2, which is assumed to be the lower limit of drainage area for COFR channel heads (Henkle et al., 2011). The lower limit was used to also remove colluvial hollow valley bottoms. This method assumes that these pixels (~10 m wide) encompass the whole valley bottom. I also used a second method to buffer out more valley bottom pixels. Stream pixels (Acc>100) were converted to poly lines in ArcGIS. I buffered them by 20 m, and removed the buffered slope pixels from the calculation. There was no significant difference in the two methods of calculating mean hillslope gradient, so I used the results from the first method in subsequent analyses. Percent area greater than 30 degrees was also calculated to estimate how much of the basin was above thresholds for landsliding (Burbank et al., 1996) and debris flow initiation (Godt and Coe, 2007). I also calculated the proportion of hillslopes that face south ($\%HS_{South}$) by extracting the pixels in a Topotoolbox-derived aspect matrix that faced between 180 and 270°.

Topotoolbox contains functions for extracting basin morphometric parameters. With these tools I calculated relief (R), hypsometric index (Hind) (Willgoose and Hancock, 1998), hypsometric integral (Hint), and drainage density (DD). In order to calculate drainage density, one must assume a channel head minimum contributing area so as to include unmarked streams. I conservatively assumed a minimum contributing area of 10^5 m^2 (Henkle et al., 2011).

Frankel and Pazzaglia (2005, 2006) have used the ratio of volume removed to drainage area (RVA) to compare landscapes affected by uplift and base level lowering. Tectonic uplift rates correlate with RVA metrics and RVAs are thought to decrease along with erosion rates after uplift ceases. I calculated RVA for each basin using methods outlined in http://gis4geomorphology.com/ratio-of-volume-to-area-rva/. Negative values in the volume removed raster were reset to 0, assuming that the modern topography that protruded through the interpolated surface was present in the interpolated paleosurface.

Relief ratio (RR) has been shown to scale with reservoir sedimentation rates in the high plains of Wyoming (Hadley and Schumm, 1961). To test this over cosmogenic timescales, I calculated relief ratio using three different basin length metrics. The first method used the Topotoolbox flowpathdistance function to calculate the longest horizontal flowpath distance. The second method draws straight line segments from the highest point to the outlet, while generally following the flow path of the main stem stream. The third method draws a straight line between the highest point in the basin and the basin outlet. Relief was divided by all three of these horizontal distances to calculate relief ratio. RR calculated with a straight line was used for subsequent analyses.

I extracted basin outlet slopes from StreamStats (Capesius and Stephens, 2009) and calculated the steepness index at the basin outlet (Hack, 1973; Ouimet et al., 2009) and concavity ratio (C_r). Concavity ratio is the ratio of area underneath the longitudinal profile minus the area under a triangle drawn from the top and bottom of the profile, divided by the longitudinal profile integral.

4.6 Statistics

I used t–tests to test the hypotheses that the two populations of basins were denuding at different rates, and had differences in their morphometric properties. I used the multivariate cluster analysis, categorization and regression (CART) analysis, multivariate regression, and stepwise multivariate regression (Everitt and Dunn, 2001) to attempt to predict denudation rate using basin-averaged morphometric parameters, as well as fluvial sediment grain size parameters.

In order to understand the toposequence of regolith evolution, I used multivariate ANOVAs 1-way analyses, Kruskal Wallis tests, and their multiple comparisons to compare regolith depth, median grain size, and % silt and clay regolith data collected. I separated the soil data from upper basins and lower basins in these analyses. Regolith data were further tested to compare differences in the above parameters with aspect, hillslope position, vegetation type, and underlying materials. Principal Component Analysis (PCA) was used to constrain similarities in between dust and BHF regolith, in order to understand dust provenance on the COFR.

5 Results

5.1 Cosmogenic radionuclides

In this section, I present the results from the ^{10}Be CRN geochemical analysis, including the measured concentrations, as well as the inferred rates and time scales. The Purdue PRIME lab AMS returned $^{10}Be/^{9}Be$ ratios for each samples, as well as blanks to constrain potential contamination (Table 7). The uncertainty from the AMS measurement was propagated through the calculation of N_{Be} in order to estimate the internal uncertainty. Shielding factors, CRONUS inputs, and CRONUS outputs are presented below for the Trail Ridge (TR) and Big Horn Flats (BHF) sites.

5.1.1 Peak bedrock and regolith samples

The peak bedrock and soil samples had sufficiently low values of slope and topographic shielding for these factors to be ignored, but there was a significant snow shielding factor. The Big Horn Flats boulder (Figure 9) rose 1 m above the regolith surface, higher than the modeled mean annual SWE depth, and therefore production was not scaled for snow shielding. The other peak samples showed a 15% decrease in scaling. Strike and dip measurements showed that bedrock surfaces were relatively flat and the slope scaling factor is negligible. The Trail Ridge bedrock sample had two dipping sides and a corner that pointed upward (Figure 9). This geometry was assumed to be flat and no slope shielding correction factor was applied. The Trail Ridge soil and bedrock pits both have relatively similar N's and D's, which shows that the bedrock outcrop and surrounding regolith surface are geomorphically connected. Intermediate diameters of talus clasts surrounding the TRx outcrop were measured to estimate uncertainty from episodic denudation (mean chipping length = 6 mm). This range was estimated by adding the relative uncertainty from CRONUS outputs (~10.4%) to the maximum denudation rate from the Small et al. (1997) model, and subtracting the relative uncertainty from the minimum denudation rate. Calculated exposure age for TRx is ~16 kyr, assuming no denudation.

The N's and modeled D's of the paired boulder and regolith samples of Big Horn Flats are significantly different from each other, implying they are denuding at significantly different rates, or that the boulder recently underwent significant episodic erosion due to periglacial processes. The CRN concentrations could also be recording the unearthing and exposure of this boulder to the surface. A minimum exposure age (T_e) for BHFx is ~20 kyr, which would mean it was exposed before the glacial retreat. The top of BHFx would still be exposed to the atmosphere at that point, assuming that it has maintained its altitude, and assuming steady state regolith production and denudation of the surrounding soil (9.3 mm/kyr). Surrounding smaller boulders indicate that this large boulder does significantly backwear from the sides episodically, but there was less evidence of significant episodic spalling of blocks from the top. In the field, a joint spacing of ~ 1 m was measured on the boulder. Therefore, assuming 1 m episodic erosion events, the uncertainty in denudation rate can be estimated (Small et al., 1997). This estimates a range of ~44 to ~20 mm/kyr for the boulder surface denudation rate incorporating the relative errors from the CRONUS model.

5.1.2 Basin-averaged denudation rates

Monte Carlo simulations used to calculate basin-averaged denudation rates and uncertainties report coefficients of variation between 5 and 9%. This shows that the prediction interval for snow depth did not affect calculation of denudation rates too far above normal errors associated with this method (~10-20%). However, the basin-averaged rates are slow enough that significant biases are coming from the assumption of no radioactive decay. The sensitivity analysis shows that the assumption of no radioactive decay over-estimates these denudation rates from between 2 – 5% (Figure 11). This over-estimate is within the standard errors from the

Monte Carlo simulations, but must be taken into account when interpreting the rates. Figure 11 shows that slower rates are overestimated more than faster rates, which means that any apparent spread in rates from the data in this study may actually be larger.

The time scale that these rates represent spans the last glacial maximum of COFR Pinedale glaciation. Therefore, climate was significantly cooler during the beginning of this denudation rate. Because these rates span several climatic events, including the last glacial maximum and the younger Dryas, these rates represent a mix of driving factors and therefore may not be able to represent a clear climate-induced denudation signal. The colder Pleistocene climate that these rates capture means that modern estimates of SWE for catchments are likely underestimates for the entire duration of denudation, therefore overpredicting the actual <D>.

5.2 Estimation of fire disturbance recurrence interval

Using the lower basin denudation rate group mean (26.3 mm/kyr), and the results of Moody and Martin’s (2001) study of the Buffalo Creek fire, I can estimate the recurrence interval of large, stand-killing fires. This estimate is based on the assumption that post-fire denudation is the only major disturbance process, and that the magnitude, relaxation time (4 yr), and background erosion rates observed at the Buffalo Creek fire are correct. The recurrence interval required to create the cosmogenic denudation rates (26.1mm/kyr) is ~500 yrs. This assumes that the background rate is constant, and that each major fire increases the denudation rate to that observed in the Buffalo Creek fire for 4 years following a fire. If I assume that the post-fire denudation rate decreases linearly from post-fire peak to background in 4 yrs, the fire recurrence interval is ~250 yrs.

5.3 Testing Hypothesis 1

Means of peak rates are significantly higher than means of the basins, and the means of the two basins are not significantly different from each other. The statistical power of comparing the peaks to the basins is low, because of the low number of peak sites tested. BHFx was kept out of this statistical comparison, due to uncertainty in the interpretation of the N_{10Be}. The similarity of the two groups of basins is surprising, since they have very different ecosystems and suites of geomorphic processes. There does seem to be a pattern among the set of ten basins, where there is a group of quickly eroding basins ($\langle D \rangle > 28$ mm/kyr) and a group of slowly eroding basins ($\langle D \rangle < 25$ mm/kyr). The question is why these two groups, which include basins from the upper and lower process domains, are denuding at different rates. I use sediment sample texture and basin morphometric data to understand the differences in denudation.

5.4 Basin morphometry data

Basin-averaged denudation rates correlate weakly with some basin morphometric parameters. There are no strong linear correlations between the whole population and any basin morphometric parameters. However, separating the upper and lower basins, certain patterns emerge. All high linear correlation R^2 values were checked to determine whether a single large value was leveraging the best fit line. The linear correlation assumes that all of these relationships are linear, which may not be correct. The parameters most correlated with the upper basin denudation rates are % south facing slope (negative), basin area, hypsometric integral, and relief ratio (negative) (Table 10, Figure 12). The lower basins show much lower R^2 values, with RR (negative), DD, and HS being the highest. Additional morphometric parameters are in Appendix D.

The results of the multivariate tests were similarly inconclusive. The CART analysis chose the hypsometric index (HI) to separate the quickly and slowly eroding basins, and included no other branches in the tree. An HI of 0.56 separated the fast and slowly eroding basins, which would mean that the more slowly eroding group is more “mature,” in a Davisian sense, and may be further along in its response to base level drivers. A forward stepping multivariate regression was also used to select more variables that may be relevant. Eight variables were input into the parameter based on previous relationships reported (S, Relief, RR) and theorized (RVA), as well as results that are relevant to this study (C_r , $\%HS_{South}$, $\%HS_{>30°}$). The stepwise linear regression included none of the variables selected for the analysis (Table 10). $\%HS_{South}$ reported the lowest P value for being included in the model.

5.4.1 Testing Hypothesis 2: Basin Morphometry

Although differences in denudation rates between upper and lower basins are not supported by the data, I compared the morphometric parameters of the two basins to test whether basin morphometry has evolved differently to set the same denudation rate. The morphometric parameters were also compared between basins using t-tests to evaluate the differences in parameters between the upper and lower group of basins. Significant differences are found in relief and all related parameters (RR, Hind). Upper basins also have significantly higher drainage density (DD).

5.4.2 Sample grain size

The grain size of the sample appears to influence the denudation rate of the basin. <D> increases with the relative amounts of the largest grain size fraction (d>4 mm), a relationship which has been noted in multiple studies. This means that sediment with the largest grain sizes has lower concentrations of ^{10}Be. A combined CART analysis with both % grain size parameters and morphometric parameters generated one branch with % of sample between 250 and 500 µm, which separates the quickly eroding basins from the slowly eroding basins. However, R^2

values are highest between the highest grain size fraction and <D>. Circumstantial evidence shows the relationship between denudation rate and coarse grain size is also controlled by the valley type process domain (Wohl, 2010) at the sampling outlet. Basin outlet sampling locations were classified as confined if hillslopes abutted against both banks in the channel, and partially confined if there was a floodplain, or significant surface at or slightly above the channel bank top on either side of the channel. Samples collected in confined channels were coarser, and showed a greater variability in inferred denudation rates, including all of the quickly eroding basins. Partially confined reaches show less variability in denudation rate, the samples contained less coarse material, and the correlation between <D> and $\%d_{>4mm}$ was higher (Figure 13).

5.5 Testing Hypothesis 2: Regolith Depth Patterns

Although there are not significant differences in <D> between the upper and lower populations of basins, the patterns of regolith thickness are different. I have compared hillslope regolith depths (h_R) to local aspect, local slope, hillslope position (%HL), and underlying materials to understand the storage and transport of regolith on hillslopes in each group of basins. This analysis uses regolith depth as a proxy for regolith development. The number and thickness of soil horizons within each regolith was low, with little variability, so I assumed that all of this top layer of material was active regolith and therefore has minimal soil horizonation. Regolith depths, however, are the result of transport processes up and downslope of the site, as well as production of regolith at the site itself. Therefore, deeper regolith potentially contains the signal of stability, higher weathering rates, and the relative balance of deposition to erosion. It is therefore important to think of all of these factors when examining hillslope regolith patterns.

Values of h_R are significantly larger on hillslopes in the upper basins than the lower basins (Figure 14A). Both a t test ($p = 5.1*10^{-9}$) and a Wilcoxon rank sum test ($p = 2.1*10^{-8}$) reject the null hypothesis that regolith depths from the upper basins and lower basins are from the same normal distribution. Mean upper basin hillslope regolith depth is significantly larger by 6 cm than mean low basin hillslope regolith depth. An F-test also rejected the null hypothesis that the two groups have equal variances ($p = 0.012$). Therefore, lower basin regolith depths show greater variability than upslope soils.

ANOVA and Kruskal Wallace tests for h_R depths at different hillslope positions in the upper basins show that there is a significant difference between peak regolith depths and the lowest two hillslope positions, at 60 and 80% hillslope length from the divide. Lower basins show no significant variation in regolith depth along the hillslope length. The variations in mean regolith between hillslope sites is at most 5 cm in lower basins (Figure 14C). Both groups show the highest variability at 40% of hillslope downslope of the divide. Upper basins show no significant difference in regolith depths with aspect, although mean h_R values on south and north aspects are slightly higher than other aspects. Likewise, there are no significant differences between h_R with aspect, although flat surfaces have lower h_R values. Both upper and lower basins show significantly lower h_R values on bedrock. Both groups also show significantly higher h_R on saprolite, and lower h_R on top of buried colluvium. Upper basins have deeper soils on mass wasting deposits, and the h_R values on top of lower basin mass wasting deposits have the highest standard deviation.

5.5.1 Regolith grain size

Regolith textural analyses were calculated in two ways. Whole samples and the fine earth fraction ($d<2mm$) were each analysed in Gradistat. I compared subsamples of the two groups of regolith from each basin, as well as grain size analyses from BHF Regolith. BHF regolith samples were much finer, although the low sample size limits statistical comparison. Lower basins had lower median grain sizes (D50) than upper basin regolith, and higher amounts of silt size particles than upper basins. No discernible trend is apparent between grain size metrics and hillslope position in this data set.

5.6 Big Horn Flats geochemistry

This section covers the pressed pellet trace element and major element geochemistry for 10 Big Horn Flats regolith samples and 3 bedrock float samples. Additional data are contained in Appendix E. The major elements and titanium (Ti) estimates are accurate to within ~10%. For chemical weathering and dust deposition calculations, I used the mean of the rock, regolith, and dust compositions and propagated the standard deviations through each calculation. This assumes that the distributions are normal, so the standard deviation is valid, and that the variables are uncorrelated. Elements with reported nondetects from the XRF were ignored from the analysis. I converted oxide % weight concentrations into elemental parts per million (ppm) by multiplying the concentration by the proportion of the elemental proportion of the molecular weight, and multiplying that by 10^4 to convert from parts per 100 (%) to ppm.

I calculated τ for each element reported in the XRF analysis using both Zirconium (Zr) and titanium (Ti) as immobile tracer elements (Figure 15). All elements are depleted with respect to Zr, indicating significant chemical weathering (Figure 15). Elements are less depleted with respect to Ti. Zr and chromium are both enriched with respect to Ti (Figure 15). The calculated chemical weathering rate using the method of Riebe et al. (2003) (Equation 13) and the ratio of Zr in rock and regolith (W_{Zr}) is 10.9 ±3.4 t/km^2 yr assuming that Zr is immobile and has not been affected by dust inputs. W_{Ti} is 6.1±1 t/km^2 yr, which is much lower than $W_{Zr.}$ In an ideal weathering situation, Ti/Zr should not vary significantly from the parent material if the two elements are both truly chemically immobile, and not preferentially eroded. Therefore, the disconnect in the amount of weathering calculated from the two elements as well as a lower regolith Ti/Zr (6.2±1.8) than the parent material (8.3±1.3) implies preferential erosion of Ti or the input of eolian dust that is relatively enriched in Zr. The latter is more likely the case, since eolian dust inputs have been attributed to soil development on the COFR (Muhs and Benedict, 2006).

Big Horn Flats is situated downwind of several major dust-producing areas, and workers have constrained dust sources in the Colorado Rocky Mountains including North and Middle Parks (Muhs and Benedict, 2006), the Colorado Plateau and Great Basin (Lawrence et al., 2010), Mount Saint Helens volcanoes (Thorn and Darmody, 1985), and Asia (Neff, 2008). In order to constrain the provenance of eolian dust deposited on Big Horn Flats, I compared the geochemical signal of BHF regolith and bedrock to dust geochemical data from North and Middle Park, CO (NP&MP) (Muhs and Benedict, 2006), Modern dust inputs into the San Juan Mountains (SJ) (Lawrence et al., 2010), loess-forming sediment from eastern Washington (EF) (Sweeney et al., 2007), and modern dust from southern Nevada and California (Reheis et al., 2009). Reheis et al. (2009) performed a cluster analysis on samples to separate dust into geographic groups using geochemical signatures. The analysis clustered the samples into 4 groups, Amargosa (Am), East Mojave (E Mo), North, Owens Valley (OV) and Southeast Nevada (SE N). These groups were all compared to BHF regolith and bedrock as possible dust sources. This analysis is limited due to different geochemical techniques used in each study, which report some trace elements and not others. For instance, ICP-MS data from Lawrence et al. (2010) significantly underestimate Zr concentration (Lawrence, 2013, pers. comm.), which would throw off any subsequent P_d calculations. Likewise, XRF pellets from this study and loose XRF powder from Muhs and Benedict (2006) provide less accurate estimates of major element and Ti concentrations. Regardless of the limitations, it is still useful to compare the chemistry of these data and attempt to constrain dust sources.

PCA analyses were performed on all of the shared geochemical elements reported (K, Ca, Fe, Ti, Zr, Ce, La, Ba, Y, Sr) and just the trace elements (Ti, Zr, Ce, La, Ba, Y, Sr). The southern Nevada data were left out of this analysis because only major element and Zr concentrations were reported. The full PCA (Figure 16) shows the BHF regolith plotted between bedrock and the group of dust samples along PC score 3, which is primarily governed by K. This shows that regolith composition may be influenced by all the dust sources that plot together along PC 3. PC 1 and PC 2 do not separate the regolith and the rock at all, implying that Ca and Fe explain less of the variance between the regolith and rock. PC 1 does significantly separate the BHF samples from the dust samples. The trace-element-only PCA (Figure 17) analysis shows regolith data plotting closer to the North Park dust data along PC 1, which is primarily controlled by Ti. Component 3, however, skews the bedrock closer toward dust. Both PCA analyses show the possible influence of the North Park silt geochemistry, so I calculated dust deposition rates using the Ti and Zr concentrations in the BHF bedrock, regolith, and dust.

The f_d calculated for NP&MP dust is negative, which is an impossible result similar to Ferrier et al. (2011), who attributed it to variable source rock from what was collected upslope of the sampling area. Since BHF is on a very flat surface, with nothing but Silver Plume Granite outcropping for tens of meters around the sampling location, the possibility of alternate source material is unlikely. Figure 18 shows that the BHF regolith samples are much more enriched in Zr compared to Ti than any of the dust data, which means that most of the dust sources cannot address the offset of Zr- and Ti-derived chemical weathering rates. Four dust trap locations in the Eastern Mojave Desert (Reheis et al., 2009) do show a low Ti/Zr ratio (4.68±1.4) (Figure 18). The concentrations of Zr and Ti in this dust is significantly lower than the regolith, which means that significant chemical weathering has taken place if this dust is the sole inputl I attempted to estimate dust deposition of these sources, but f_d (0.60 ±0.063) is very large, due to a small denominator in the calculation (Equation 15). Ferrier et al. (2011) showed that this method becomes inaccurate when the denominator in Equation 15 is small. Therefore, an accurate estimate of dust deposition is not possible.

5.6.1 Testing Hypothesis 3

Studies have suggested the significance dust deposition in the alpine zone of the COFR. (Thorn and Darmody 1985; Ley et al., 2004; Muhs and Benedict, 2006), and BHF sediment samples contain on average 9 - 23% silt sized particles, which is much higher than basin soils in this study (~1%). However, geochemical data provide no chemical enrichments that are seen in other soils, which means that chemical weathering is strong enough to remove any dust enrichment of elements except for chromium, which has been shown to adsorb to eolian dust (Lawrence et al, 2010). This enrichment implies some dust inputs, along with the change in Ti/Zr ratios between rock and regolith. However, since I am unable to quantify dust deposition rates, I cannot adequately address this hypothesis.

However, I can use modern dust input estimates and BHF regolith texture to test this hypothesis. Assuming that the CRN regolith production flux (24.5 t/km^{2}yr) pertains to the physical production of regolith coarser than silt, and the deposition flux from Ley et al. (2004) (5.2 t/km^{2}yr) provides all of the silt sized particles to the regolith, we can estimate the silt size fraction of the regolith:

$$\%Silt = \frac{P_d}{(P_r + P_d)} \qquad \text{(Equation 16)}$$

This equation assumes no chemical weathering, and steady state regolith production, dust deposition, and no preferential erosion due to grain sizes. Percent silt size can also be estimated from the W's calculated above, assuming that chemical weathering is only occurring on the coarser than silt fraction of the regolith, an assumption that is made in the calculation of W (Riebe et al, 2003):

$$\%Silt = \frac{P_d}{(P_r - W + P_d)} \qquad \text{(Equation 17)}$$

Calculating % silt assuming no chemical weathering, W_{Zr} and W_{Ti} yields ~17%, ~28%, and ~22% respectively. These overestimate of % silt means that chemical weathering of the silt is occurring, which is very likely, or that millennial scale dust deposition fluxes are lower than measured by Ley et al. (2004). This same estimate can be made using average basin sediment production rates from this study (69 t/km^{2}yr), assuming no chemical weathering yields 6% silt, which is much larger than the regolith textures measured in this study (~0.8% silt). It is likely that dust deposition rates are significantly lower below the tree line which results in an over estimate of silt content. These calculations show that hypothesis three is possible, even with some chemical weathering of silt. However, better constraints on long term dust deposition rates would allow for a quantitative assessment of this research question.

6 Discussion

6.1 Peak denudation

Of the peak rock and soil denudation rates measured in the study, only the BHF regolith production rates match nearby CRN peak rates in the Rocky Mountains (Small et al., 1999). This implies that perhaps summit flat soil production rates are slow and similar to Wind River Range subsummit surfaces. Assuming that the BHFx boulder top has been exposed and not eroded, and that the regolith denudation rate surrounding it has been constant, reconstructing 20 kyr of erosion would not cover up the boulder that reaches 1m above the current surface. At most, the boulder would be ~80 cm above the current surface, and completely exposed to cosmic rays. Therefore, both the maximum erosion and minimum exposure age are poor models to describe the CRN concentration in this boulder, and a second CRN isotope concentration could further deconvolute the exposure history.

Rates of bedrock and regolith production on the TR saddle are four times as fast as any other rate previously published. Although the sample size is too low to make a significant conclusion, one could infer that this saddle or glacial col is connected to glacial incision on both sides, and therefore is responding with higher denudation rates. The TRx minimum exposure age could imply that there was glacial or firn ice covering the surface and outcrop until the glacial recession began, but evidence of a significant talus pile around the outcrop shows that there has been significant erosion as well (Figure 9). It is also likely that the SWE correction is an underestimate and therefore the <D> values reported here are overestimates, but the magnitude of difference between the saddle and peak surfaces in tors is such that more data should be collected to discern the pattern between the two landforms.

6.2 Basin denudation, morphometry, and regolith

The two groups of basins are eroding at the same rates, even though each group has unique sets of geomorphic processes and histories. This could be due to the fact that the rates extend back into the Pleistocene (Figure 10), when the climate was significantly cooler, the lower basins may have had ecosystems and disturbance regimes more similar to modern upper basins, and larger areas in the upper basins were above tree line and subject to more intense periglacial weathering. Anderson et al. (2012) modeled frost weathering processes on COFR hillslopes and found that weathering and erosion increased during glacial minimum cycles. The apparent pairing of glacial retreat and downstream fluvial incision (Schildgen et al., 2001; Dühnforth et al., 2012) implies that base level changes affecting the two groups of basins are similar in timing if not magnitude, and might not affect the denudation differently.

Although they are both eroding at the same rate, the two populations are significantly different in some morphometric parameters. Higher relief in the upper basins may be the result of being on the upthrown side of Miocene extensional faulting, which uplifted the slowly eroding Rocky Mountain Surface that has maintained higher ridges. Higher drainage density in the upper basins could reflect the higher precipitation amounts in these basins.

Values of <D> measured in this study are very weakly correlated with some basin morphometric parameters, and the two groups of basins respond differently to different morphometric parameters. Although much has been mentioned on the slope and ecosystem asymmetry of north- and south-facing slopes in the COFR montane zone, the relative amount of south-facing hillslopes is negatively correlated with upper basin denudation rates. This could potentially be due to higher snow accumulations on north-facing hillslopes, providing greater amounts of water to weather and denude the upper basins. The lower basin denudation rates are less linked to their morphology. Examples in the literature of long term denudation rates relating to topographic metrics usually relate to faster denudation rates and more pronounced driving forces, including tectonic incision and intense glaciation (Burbank et al., 1996; Stock et al., 2009; Ouimet et al., 2009). These tectonically active landscapes evolve quickly enough so that topography can respond to denudation rates.

The slower rates measured in this study, and relatively weak glaciation and lack of active tectonics in the COFR, may prevent clear relationships between morphometry and denudation rates. Relationships in the literature between hillslope gradients and denudation rates have shown threshold responses to denudation rate at ~30° hillslope gradients. The basins in this study all have less than 20% of basin area that are steeper than the threshold, providing one reason for slower denudation and the weak relationship between HS and <D>. The relationship between relief and denudation for this study does not follow the linear relationship seen in other data sets of lower erosion rates (Montgomery and Brandon, 2002). The threshold response seen in this model at R = ~1000 m does not appear in my dataset, which could be due to the fact that orographic processes are weaker on the COFR due to moisture limitations, so higher relief basins do not have the erosional advantage of higher discharges.

Much stronger correlations between the fraction of coarse gravel sampled (%d>4 mm and %d>2 mm) and denudation rate imply a disconnect in source area and transport processes between coarse and fine sediment (Matmon et al., 2003; Niemi et al., 2005; Belmont et al., 2007). The sediment provenance mechanism, in which the rate of grain size reduction occurs more rapidly than downslope transport, occurs in regions where chemical weathering is intense and hillslope creep is the dominant process (Matmon et al., 2003; Belmont et al., 2007) Likewise, deep-seated landslides can bring buried coarse clasts directly into the channel. Deep-seated landslides are rare in unglaciated basins on the COFR, but proximal sources of coarser sediment could be a significant factor, since most streams in this study are small enough to move larger sediment rarely in large floods or debris flows. Therefore, the majority of coarse sediment in a reach at a given time could be locally sourced, as opposed to coming from far upstream. The provenance mechanism is supported by the differences in partially confined and confined sampling sites. Local hillslope materials with relatively low concentrations of CRN are being supplied from adjacent hillslopes in confined reaches, while partially confined reaches are supplied by a better mix of watershed material from upstream, as well as material released from storage on the flood plain deposited by large flows, which would more likely come from upstream. This trend needs to be explored further by measuring grain-sized fraction CRN concentrations in confined, partially unconfined, and unconfined reaches.

Regolith is significantly deeper on upper basin hillslopes, which fits the conceptual model set forth in this study (Table 3, Figure 2) because weathering rates are potentially higher and disturbance less frequent in the upper basins. Upper basin hillslopes also seem to have a more organized distribution of regolith depths along hillslope transects. The lower depths in the upper hillslope (erosion zone), the higher variability midslope (transition zone), and the deeper regolith at the bottom of the hillslope (deposition zone) resemble the k-cycle of hillslope soil development (Butler, 1982). The relative development of hillslope regolith patterns implies a longer recurrence interval for hillslope denudation events (Tonkin and Basher, 1990). Welter (1995) found similar patterns of shallow regolith on crests and deeper regolith on footslopes of colluvial hollow hillslopes in the Rampart Range in southern Colorado. The lack of pattern on lower basin hillslopes, as well as shallower regolith depths, speaks to higher recurrences of erosional disturbances that remove regolith from hillslopes before diffusive processes have time to distribute regolith along a hillslope. Lower and more varied regolith depths on mass wasting deposits also imply less time for regolith mixing and buildup on mass wasting deposits and more frequent mass wasting events.

6.3 Basin-averaged denudation in context

Placing denudation rates cited in this study in the context of other rates measured on the COFR (Figure 19) shows that CRN-derived denudation rates on the COFR are generally lower than longer term incision rates on the COFR and exhumation rates in the early Cenozoic. They are similar to net post-Laramide denudation rates (~36 mm/kyr, Kelley and Chapin, 2004). Holocene and modern erosion rates are also larger, but have more variability and are governed by large infrequent events such as debris flows. This decrease in denudation from the Cenozoic reflects the end of major mountain building, and the slowing denudation as landscape evolution continues and tectonic forcing diminishes. The variability of recent denudation rates speaks to the short term temporal variability and importance of large events, such as fire (Moody and Martin, 2001), which are not often accounted for in short term denudation measurements. Holocene sedimentation rates in cirque tarns and beaver meadow complexes are an order of magnitude higher than CRN-derived denudation rates. These are minimum denudation rate constraints assuming that all of the sediment eroded from upstream is deposited in these sedimentary units. This apparent large increase in denudation rates during the Holocene could be reflecting a transient response to climate change. However, the order of magnitude increase presents a clear trend, and CRN <D> values in this report include some from this period of increased denudation. If the rates I have measured are in fact a time average of denudation rate of the basin over ~20 – 30 kyr, and Holocene denudation rates are an order of magnitude higher, then Pleistocene rates are likely significantly lower than the average implied by the ^{10}Be concentrations. However, in a changing erosional regime, <D> values may be biased to the earlier part of the denudation history because ^{10}Be concentrations are lagging in their response to this change in erosion rate (Parker and Perg, 2005). Consequently, the Holocene increase in erosion rates may not be reflected in the CRN concentrations.

This increase in debris flow erosion during the Holocene recorded in lake sediments on the COFR (Menounos, 2000) has been attributed to the increased regularity of monsoonal precipitation bringing intense convective rainfall that triggers the major erosion events in upper alpine regions (Godt and Coe, 2006) and lower montane zones (Moody and Martin, 2001). Therefore, although frost action weathering may have been higher during the late Pleistocene due to cooler climate (Anderson et al., 2012), the apparent lack of increase moisture means that freeze-thaw weathering on the COFR may still be moisture limited (Thorn, 1979). Debris flows that move most of the sediment out of the basins were less frequent. Therefore, Pleistocene denudation rates may have been lower due to fewer erosional disturbances.

Both estimates of fire recurrence intervals are longer than reported recurrence intervals for montane zone stand-killing fires (<100 yrs) (Veblen and Donnegan, 2005), and within the same order of magnitude of subalpine forest recurrence intervals (>100 yrs). This suggests that the Buffalo Creek fire was an unusually large disturbance, and that many stand-killing fires do not receive the rainfall intensity to cause erosion of that magnitude. The data may also suggest that Holocene and late Pleistocene stand-killing fire erosion event recurrence intervals were higher in the lower alpine and upper montane forest than they are today. This would make sense in the context of a warming Holocene climate with increased monsoon convective precipitation.

The <D> values reported here an order of magnitude lower than most tectonically active ranges, and more akin to older orogens such as the Great Smoky Mountains (Matmon et al., 2003). It is surprising that a higher relief, glaciated mountain range can be denuding at the same rate as an unglaciated, less pronounced mountain range that is three times as old. However, the Appalachians are much closer to maritime moisture masses, as well as ocean base level fall and subsequent fluvial incision. Higher moisture availability and incision could create the same erosive power despite less potential energy (topographic relief), while COFR erosion regimes have been moisture-limited during the Quaternary, which limits both weathering and disturbance regimes.

6.4 Chemical weathering and dust deposition

The geochemical data reported here suggest long term non-eolian chemical weathering rates that are similar to modern rates generated from stream chemistry (5.8 – 12 $t/km^2/yr$ assuming 44% calcite and 56% oligoclase weathering) (Sueker et al., 2001). The lower Ti/Zr ratio can mean one of two things: preferential weathering and erosion of Ti-bearing minerals, or deposition of lower Ti/Zr dust. One could speculate that Ti, being in slightly more magnetic minerals, could be more affected by lightning disturbance, a process theorized to be significant on these surfaces (Anderson et al., 2006). However, it is much more likely that the Ti/Zr shift is the result of dust deposition. Dust from the Eastern Mojave desert (Reheis et al., 2009) is one potential upwind source that can explain lower Ti/Zr in regolith. Dust geochemical signatures from this region have lower Ti/Zr than BHF bedrock, but the compositions are similar enough that calculation of an accurate dust deposition rate is impossible using Ti and Zr concentrations. Mojave dust has been attributed to silt in soils on the Colorado Plateau (Goldstein et al., 2008) which lies in between the COFR and the Mojave Source area, indicating a dust trajectory with COFR in the path. Analysis of dune migration in the Basin and Range also shows a dominant eolian transport trajectory towards the COFR from southeastern California and Nevada (Jewell and Nicoll, 2011). However, a single source area is probably not that likely over the timescale of cosmogenic denudation for the COFR, and mixtures of Ti and Zr-enriched dust further complicate interpretation. More work is needed to separate out multiple dust inputs in order to constrain uncertainty associated with dust deposition rates and chemical weathering element fluxes on COFR summit surfaces.

The relative lack of evidence of North and Middle Park eolian silt deposition is surprising, since evidence suggests significant inclusions appear on young moraines (Muhs and Benedict, 2006). However, this could be another artifact of the timescale of deposition. The regolith production rate spans well into the Pleistocene, although that includes periods when the quartz crystals were bedrock and saprolite. One could estimate regolith residence time assuming steady state and assuming a uniform regolith depth (~25 cm measured in the field). This depth translates to a one-dimensional residence time of ~27 kyr over which this regolith has accumulated dust. Therefore, it covers twice as much time as the dust deposition record on the COFR moraines, and extends well into the Pleistocene. Paleoclimatic evidence has suggested that the southern summer location of the jet stream drove more dry air masses from the Pacific to Colorado (Friedman et al, 1988). These air masses may have crossed the source area of the Eastern Mojave Desert more often, and brought low Ti/Zr silt to the COFR.

7 Conclusion

CRN-derived rates measured in this study show that differences in modern hydroclimatology, basin morphology, and base level forcing do not significantly control denudation rates over timespans of 10^4 years on the COFR. This is because the timespan of the rates makes it harder to link differences in climate to denudation when each group has been subject to mixed climate factors. Base level lowering from glaciation and downstream fluvial incision has occurred in concert, so recent landscape evolution may be affecting these basins in the same way. Although these two groups of basins are denuding at the same rates, the pattern of regolith thickness is more pronounced on upper level basins, which implies that large scale erosional disturbances are less frequent.

CRN-derived denudation rates are an order of magnitude lower than Holocene sedimentation rates in the area, implying that denudation was much lower in the late Pleistocene in non-glaciated basins, even though freeze-thaw weathering of sediment may have increased. This is likely due to decreases in monsoonal moisture patterns that bring intense convective rainfall that is responsible for the majority of debris flows on the COFR. The warmer climate in the late Holocene likely increased the occurrence of wildfire, which is an important trigger for large erosional disturbances. This southern jet stream may have changed the provenance of eolian silt onto COFR summit flats, depositing silt with low Ti/Zr ratios. Long term denudation rates on the COFR are much lower than other regions with similar relief, and the rates are similar to older, less pronounced mountain ranges. The COFR may be eroding more slowly in the Quaternary due to its distance from moisture sources, which generates a drier climate and therefore less intense weathering, and glaciation. The distance from the ultimate base level limits topographic rejuvenation from sea level fall and incision. This point alludes to the possibility that mid-continent mountain ranges may have more topographic longevity because of their distance from moisture sources.

7.1 Future Work

Four questions that have arisen from this study are grain size dependencies on CRN concentrations in the COFR, the potential patterns in the denudation of ridgetop landforms, the apparent increase in denudation during the Holocene epoch, and the potential for multiple dust sources and origins low Ti/Zr inputs into the COFR. Grain-size-separated CRN concentrations from confined and unconfined reaches could reveal the relative importance of different sediment sources within each process domain. Similarly, a large sample size of denudation and soil production rates on saddles and subsummit surfaces may elucidate the evolution of ridgetop morphology. The apparent order of magnitude increase in Holocene denudation is supported by limited data, and more measurements of Holocene denudation would allow us to better understand the influence of climate on the erosion of the COFR.

8 Tables

Table 1: Morphodynamic zones delineated in Caine (1984) and the relative contributions of each process

Elevation Zone	Glacial Process	Rock Glacier Flow	Talus Activity	Mass Wasting	Surface Erosion	Solute transport	Channel Activity	Lake sedimentation
High Alpine	Slight	Slight	Medium	Slight	Slight	Slight	None(?)	Slight
Alpine Tundra	None	Slight	Slight	High	High	Medium	Slight	Slight
Subalpine Forest	None	None	None	Slight	Slight	Medium	Medium	Slight
Montane Forest	None	None	None	Slight	High	Medium	High	High

Table 2: Summary of the differences in driving forces and denudation processes between the three process domains in this study. The bottom row shows the relative magnitudes of each of these processes, where W stands for the relative rate of weathering and regolith production, R_d stands for the relative storage of regolith on the peaks and in the basins, and D represents the relative frequency and magnitude of disturbances, which dictate the actual erosion from each process domain. This table shows that past work from the COFR dictates that, at least in recent time, lower basins are potentially denuding at a higher rate than the rest of the basins, although upper basins may have higher regolith storage and production rates. However, much of this is inference and more work is needed to quantify differences in denudation rates. This also shows that regolith storage may elucidate the coupling between differences in weathering and disturbance in the two groups of basins. The size of the letter in the bottom row represents the relative magnitude of that component relative to the other basins. D stands for disturbance regime, W stand for weathering and regolith production, and R_d represents regolith storage

		Peak Surfaces	**Upper Basins**	**Lower Basins**
Climate	**Past**	• Colder • More snowfall	• Colder in the past • Lower tree line • Higher amounts of snowfall • Possibly higher periglacial weathering	• Warmest and driest • Colder than present
	Present	• Coldest and windiest point, highest amount of snowfall	• Colder than lower basins • Higher amounts of precipitation, mostly from snow	• Warmest and driest • Highest occurrence of intense convective rainfall
Geologic History		• Upthrust on footwall of graben complex • Glacial cirques carved into sides of peaks	• Late Pleistocene glacial incision • Overflattened longitudinal profiles inhibit fluvial incision	• Late Pleistocene fluvial incision. • Incision-aggradation cycles connected to glaciations
Regolith Production		• Highest amount of periglacial weathering possibly exposing fresh mineral surfaces and enhancing chemical weathering.	• Higher periglacial and frost weathering than lower basins, along with possible higher chemical weathering from increased moisture	• Hotter and drier climate brings about less frost weathering and chemical weathering
Regolith Storage		• Extensive periglacial deposits and potential to build grussy regolith and eolian deposition.	• Higher weathering and lower disturbance frequency may mean higher regolith storage and higher pattern of storage	• Lower weathering rates, and higher rates of disturbance imply lower storage. Also less thick forests and vegetation to stabilize vegetation
Disturbance		• Rockfall and backwearing of headwalls, as well as eolian deflation of fine material.	• Less frequent fires and intense convective rainfall events to trigger debris flows and flash floods. • Frequent tree blowdowns may trigger greater regolith incorporations	• Higher recurrence of stand killing wildfires and intense convective rainfall means higher recurrence of debris flow disturbances.
Results		$D\ W\ R_d = E$	$D\ W\ R_d = E$	$D\ W\ R_d = E$

Table 3: Compilation of published rates of denudation on the COFR, See text for description of each study. Italicized script represents fluvial incision rates.

Study (type)	**Timescale (yr)**	**Elevation (m)**	**Rate (mm/kyr)**	**Uncertainty (mm/kyr)**
Bovis and Thorn (1981)	1.0E+00	3300	100	0
Moody and Martin (2001)	4.0E+00	1880	2500	0
Moody and Martin background	4.0E+00	1880	5.75	4.25
Polvi and Wohl (2012) [ǂ]	1.0E+03	2500	340	100
Menounos (2000) [ǂ,t]	1.1E+04	3000	160[t]	23[t]
Schildgen et al. (2002)	1.6E+05	2000	350	250
Refsnider (2011) (Spanish Gulch Sediment)	1.3E+05	3801	45.4	1.82
Dethier et al., (2006)	3.0E+04	1900	25	8
Refsnider (2010) (Marble Mtn Summit Bedrock)	2.4E+04	3930	24.7	1.01
Small et al. (1997)	7.5E+04	4000	7.1	1.2
Dethier (2001)	6.0E+05	1200-3000	85	15
Dühnforth et al. (2012)	9.5E+05	1685	400	300
Refsnider (2011) (2 Pleistocene cave deposits)	1.15E+06	3801	37.1	4.1
Refsnider (2011) (Pliocene cave deposit)	4.91E+06	3801	4.85	1.09
Pazzaglia and Kelley (1998)	5.2E+07	2810	145	25
McMillan et al. (2006)	5.0E+06	1685	160	79
[ǂ]Assuming that sediment ρ_b = 1.8 g/cm^3 , [t]Time weighted average of debris flow sedimentation rates				

Table 4: List and attributes of the 10 basins sampled in this study. Attributes were extracted using USGS StreamStats. Basins below the terminal moraine are shaded.

Basin	Outlet lat/lon (X° Y' Z'')	Basin Area (km^2)	Mean Elevation (m)	Mean Slope (%)	MAP* (cm)
Beaver Brook	40 22 28 N 105 36 58 W	5.98	2918	36.5	77.2
Big Horn Creek	40 24 32 N 105 35 39 W	3.094	2945	37.8	66.4
Wind River	40 19 34 N 105 34 57 W	10.9	2982	36.9	86.2
Cabin Creek	40 14 40 N 105 32 32 W	5.304	3303	45	98.3
Rock Creek	40 10 25 N 105 31 34 W	10.97	3060	35.9	81.6
Bobcat Gulch	40 26 27 N 105 20 44 W	2.18	2294	35.2	49.1
Jug Gulch	40 28 52 N 105 18 16 W	4.06	2188	37.6	49.2
Spruce Gulch	40 28 50 N 105 18 17 W	6.76	2370	34.3	52
Greyrocks Gulch[p]	40 41 46 N 105 17 39 W	2.366	2067	46.6	47.5
Skin Gulch[p]	40 40 04 N 105 23 50 W	5.122	2361	37.9	53
***: MAP = Mean Annual Precipitation, [p]: Basin is in Cache La Poudre Canyon Watershed**					

Table 5: List of Snotel sites, their SWE, uncertainty, and number of observations

Snotel site	Elevation (m)	Mean annual SWE (cm)	Number of observations	Coefficient of variation (%)
Bear Lake	2896	15.9±4.7	32	14.8
Black Mountain	2719	9.3±1.7	2	83.3
Copeland Lake	2621	3.0±1.3	31	4.3
Deadmans	3115	17.5±4.7	33	14.3
Hourglass Lake	2859	9.0±2.4	4	60.0
Joe Wright	3085	23.8±6.1	23	26.7
Long Draw	3042	16.4±9.3	3	311.4
Wild Basin	2914	14.3±3.7	8	45.7
Willow Park	3261	16.8±5.6	33	16.9
Lake Irene	3261	24.7±7.7	31	25.0

Table 6: Description of attributes observed at each regolith pit dug for this study.

Observation	Categories	Category description
Local slope and aspect	-	Local slope measured as a trend and plunge with either a Brunton compass and inclinometer, or a laser range finder
Landscape position	Ridge, plunging divide, colluvial slope, mass wasting deposit	Observed from local topographic form and materials
Hillslope form – **latitudinal (normal to fall line)** **longitudinal (along fall line)**	Convex, concave, planar, planar hummocky	Observed at the ~10^0 m scale
Understory vegetation type	Semi arid, grasses, leafy, coniferous, none	Dominant understory observed, categorized by leaves semi arid – yucca, cacti, and Sage observed in abundance grasses, leafy (herbaceous), and coniferous recognized by leaf or needle form
Understory vegetation thickness	Sparse (0-30%), medium (30-50%), dense (50-100%)	Qualitative description of %groundcover extent
Tree type	Mixed conifer, aspen, fir (Includes spruce), pine, no forest	Dominant type of tree. Conifers identified by needle shape and association.
Tree density	Full, patchy, no forest	Qualitative description of forest density. Full – canopy mostly covered, trees usually have a meter or less space between them Patchy – trees have over a meter of space between them
Forest age	Mature, multi aged, young, old growth	Qualitative estimate of forest age from largest breast diameters

Disturbance	Fire, tree throw, frost action, periglacial processes, soil creep, surface runoff, mass wasting, bioturbation	Qualitative estimate of dominant disturbance processes from observations (i.e. Fallen trees for tree throw, Large amounts of float and talus or frost heave scars, rill deposit, Burned Logs and ash for fire)
Underlying material	Bedrock, saprolite (grus), coarse colluvium, mass wasting deposit	Qualitative description of material below the regolith layer. Coarse colluvium- sample appeared to be >50% coarse colluvial clasts, which prevented pit digging. Saprolite – gruss that appeared unmixed with coarse colluvium or organic material Mass Wasting – Clast supported, unsorted deposit, Inferred landform was also used in choosing this category Bedrock – solid bedrock underneath the regolith.
Horizons	O, A, E,B,C,R and any combinations, including their thicknesses, colors, structures, and notes	Horizons chosen to match the standard descriptions (Birkeland et al., 2003) as closely as possible

Table 7: Raw CRN data used to calculate N's as well as N's and their uncertainty

Sample	Quartz Weight (g)	Mass of ^{9}Be carrier added (g)	[^{9}Be] in carrier	^{10}Be/^{9}Be AMS measurement	^{10}Be/^{9}Be measurement error	N_{10Be} (Atoms per g Qtz)	Err
11JLG01TRx	24.07	0.35531	998	7.16E-13	1.2E-14	6.93E+05	1.43E+04
11JLG02TRc	24.09	0.8496	372.5	7.18E-13	2.2E-14	6.23E+05	2.06E+04
11JLG04BHFx	22.241	0.86605	372.5	1.3E-12	1.5E-14	1.25E+06	1.66E+04
11JLG05BHFc	12.1100	0.86932	372.5	1.84E-12	4E-14	3.27E+06	7.30E+04
11JLG03BBα	24.892	0.86155	372.5	1.54E-12	7E-14	1.31E+06	6.04E+04
11JLG07BGα	28.245	0.91218	372.5	1.27E-12	9E-14	1.01E+06	7.24E+04
11JLG08BHCα	41.836	0.84899	372.5	2.29E-12	2.6E-14	1.15E+06	1.32E+04
11JLG09WRα	17.225	0.91004	372.5	6.65E-13	2.7E-14	8.55E+05	3.57E+04
11JLG10CCα	24.85	0.86642	372.5	1.59E-12	6E-14	1.37E+06	5.21E+04
11JLG11RCα	22.48	0.86497	372.5	1.02E-12	5.00E-14	9.63E+05	4.80E+04
11JLG13JGα	35.198	0.86731	372.5	1.58E-12	4E-14	9.60E+05	2.46E+04
11JLG14SGα	41.691	0.86637	372.5	1.18E-12	1.9E-14	6.01E+05	9.95E+03
11JLG18SkGα	17.089	0.86327	372.5	7.2E-13	5E-14	8.86E+05	6.30E+04
11JLG20GRCα	36.166	0.85148	372.5	8.18E-13	1.4E-14	4.71E+05	8.39E+03
Blanks (11JLG01TRx used 11FDBL01, the rest used 12CSRB02)							
11FDBL01	0	0.34738	998	1.18E-14	1.2E-15	-	-
12CSRB02	0	0.86736	372.5	1.5E-14	3E-15	-	-

Table 8: Measurements of shielding in the field, as well as production rate factors. Only snow and chipping length corrections were used to scale production rates for peak sites, since surface angle and topographic shielding are so low.

Sample	Dip angle (degrees) (shielding factor)	Topographic shielding factor	SWE(cm) (shielding factor)	Total shielding factor	Chipping length (cm)
11JLG01TRx	-	0.00015°	28±8 (0.84±0.04)	0.84	6
11JLG02TRc	-	0.00015°	28±8 (0.84±0.04)	0.84	-
11JLG04BHFx	11 (0.000483°)	0.000702°	0[3]	00.84 0	~100
11JLG05BHFc	-	0.000702°	33±12 (0.81±0.06)	0.81	-
Calculated shielding was so small that it was ignored; [3]Snow shielding assumed to be 0 because sample protrudes 1 m above the surface, which is higher than mean SWE.					

Table 9: Denudation rates for all samples collected in this study, as well as timescales, calculated exposure ages, and the percent of ^{10}Be's radioactive mean life that T spans (T/τ_{10Be}).[a] This term is important, in that it suggests that the basin average denudation rates may fail the assumption of insignificant radioactive decay.

Sample	**Elevation (m)**	**D or <D> (mm/kyr)**	**T (kyr)**	**T_e(kyr)**
11-JLG-01-TRx	3510	38.6±4 - 40.9±4.3	13.4±1.4 – 14.2±1.5	16.2
11-JLG-02-TRc	3510	45.5± 5.5	13.3±1.6	-
11-JLG-04-BHFx	3734	21.9±2.1 – 40.9±4	14.8±1.3 – 27.6±2.4	21.3
11-JLG-05-BHFc	3734	9.24±1.03	65.4±7.3	**% of τ_{10Be}**
11-JLG-03-BBα	2933	21±1.6	28.9±2.2	0.63%
11-JLG-08-BHCα	2945	23.9±1.5	25.4±1.6	0.55%
11-JLG-09-WRα	3003	33.6±2.4	18.1±1.4	0.39%
11-JLG-10-CCα	3310	24.2±1.9	25.1±2	0.54%
11-JLG-11-RCα	3078	28.8±2.2	20.2±1.6	0.46%
11-JLG-07-BGα	2309	19.1±1.8	32.0±3	0.69%
11-JLG-13-JGα	2199	18.9±1.2	32.0±2.1	0.69%
11-JLG-14-SGα	2382	33.8±2.1	17.9±1.1	0.39%
11-JLG-18-SkGα	2373	22.9±2.1	26.6±2.4	0.58%
11-JLG-20-GRCα	2082	35.7±2.1	17.0±1	0.37%

[a]This term is important, in that it suggests that the basin average denudation rates may fail the assumption of insignificant radioactive decay.

Table 10: Basin morphometric parameters,along with R^2 values for correlation with <D> for each group of basins. P values for t tests between the two groups of basins, and for inclusion in the forward stepping linear regression (FSLR) are also reported for each parameter. Uncertainties are 1 standard deviation (s). s(HS) is the standard deviation of slope within each basin, or basin roughness.

Basin	**<D> (mm/kyr)**	**HS (°)**	**s(HS) (°)**	**RVA(m)**	**C_r**	**Hind**	**Relief (m)**	**RR**	**% South facing**	**%HS>30 (°)**	**DD (m/km)**
BB	21±1.6	17.8	6.5	93.3	10.5	0.40	873	0.28	0.58	0.03	1794
BHC	23.9±1.5	18.0	7.5	32.4	7.7	0.45	846	0.30	0.73	0.07	2165
WR	33.6±2.4	18.3	7.1	68.2	6.1	0.43	1092	0.24	0.16	0.05	1647
CC	24.2±1.9	21.0	8.2	64.6	4.3	0.41	1547	0.31	0.48	0.13	2154
RC	28.8±2.2	17.9	6.2	86.3	6.6	0.45	1039	0.21	0.37	0.04	1446
UB (mean±s)	26.3±4.9	18.6±1.4	7.1±0.8	68.9±24	7.1±2.3	0.43±0.02	1080±280	0.27±0.05	0.46±0.22	0.062±0.04	1840±320
(Slope sign) R^2	--	0.01	0.027	0	0.24	0.18	0.014	0.51	0.78	0.03	0.331
BG	19.1±1.8	17.2	7.2	33.7	7.2	0.56	630	0.20	0.80	0.05	1752
JG	18.9±1.2	18.2	7.3	74.0	16.5	0.42	453	0.19	0.60	0.06	1641
SG	33.8±2.1	17.4	7.3	58.7	96.2	0.43	843	0.15	0.46	0.05	1923
SkG	22.9±2.1	18.7	8.9	79.0	7.7	0.54	674	0.17	0.30	0.11	1758
GRC	35.7±2.1	21.3	9.9	49.9	10.1	0.57	551	0.18	0.61	0.19	1725
LB (mean±s)	26.1±8.1	18.6±1.7	8.1±1.2	59.1±18	27.3±39	0.502±0.07	630±150	0.18±0.02	0.56±0.18	0.09±0.06	1760±100
R^2		0.37	0.27	0.02	0.27	0.01	0.18	0.46	0.06	0.29	0.31
T-Test p value		0.96	0.17	0.48	0.15	0.09	0.026	0.09	0.22	0.10	0.018
FSLR p value		0.45	0.60	0.19	0.31	0.84	0.84	0.53	0.07	0.47	0.69

Table 11: Zr and Ti data from BHF, as well as two potential dust sources, as well as calculated weathering rates, dust deposition rates, and weathering rates including dust deposition (W_d) (Ferrier et al., 2011, Equation 4)

Sample	**Zr (ppm)**	**Ti (ppm)**	**Ti/Zr**	**Fd**	**W_{Zr} ($t/km^2/yr$)**	**W_{Ti} ($t/km^2/yr$)**
BHF Regolith	469±130	2890±255	6.1±1.8	-	10.9±3.4	6.1±1
BHF Rock	261±25	2170±190	8.3±1.1	-	**P_d($t/km^2/yr$)**	**W_d ($t/km^2/yr$)**
NP&MPD[t]	427±103	5224±685	12.8±2.9	0.28	-	-
T25-28[o]	242±28	1112±280	4.7±1.4	0.59±0.63	36±57	~28.4

[t]North and Middle Park dust from Muhs and Benedict (2006); [o]Locations 25 – 28 in Reheis et al. (2009)

9 Figures

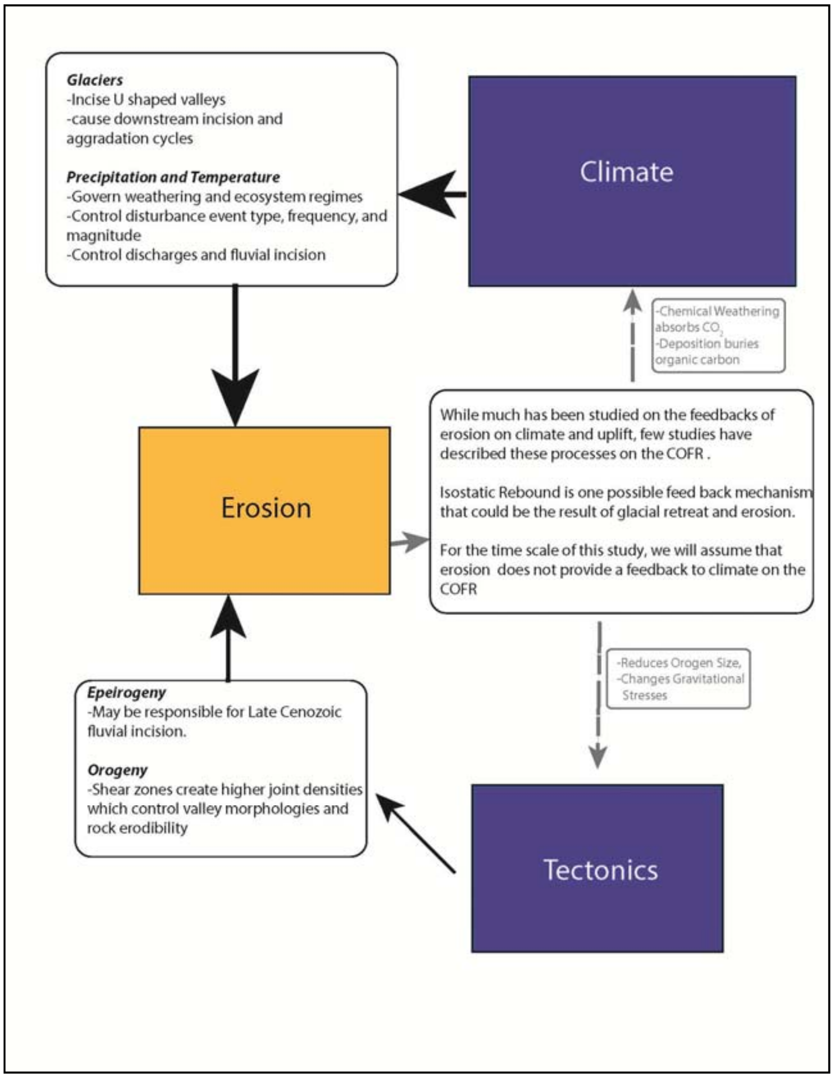

Figure 1: This figure is taken from Willet et al. (2006, Figure 1) introduction and altered to highlight the dynamics relevant to the COFR during the timescale of my study. Larger arrows indicate stronger controls on COFR erosion. Smaller, light grey arrows indicate feedbacks that may not be significant over the time scale of this study. By far the most important driver on the geomorphic regime of the COFR is climate, both through time into the colder, glaciated Pleistocene, as well as along the elevation transect of the COFR. Epeirogenic processes may be the major driver of fluvial incision on the COFR, but most of the late Pleistocene incision and aggradation seems to be linked with glacial cycles. I am leaving out the complex feedback of erosion on climate and tectonics for this study, but recognize that isostatic rebound is occurring, and that the fresh bedrock exposed from glacial and periglacial processes on the COFR may potentially be a significant absorber of carbon from chemical weathering.

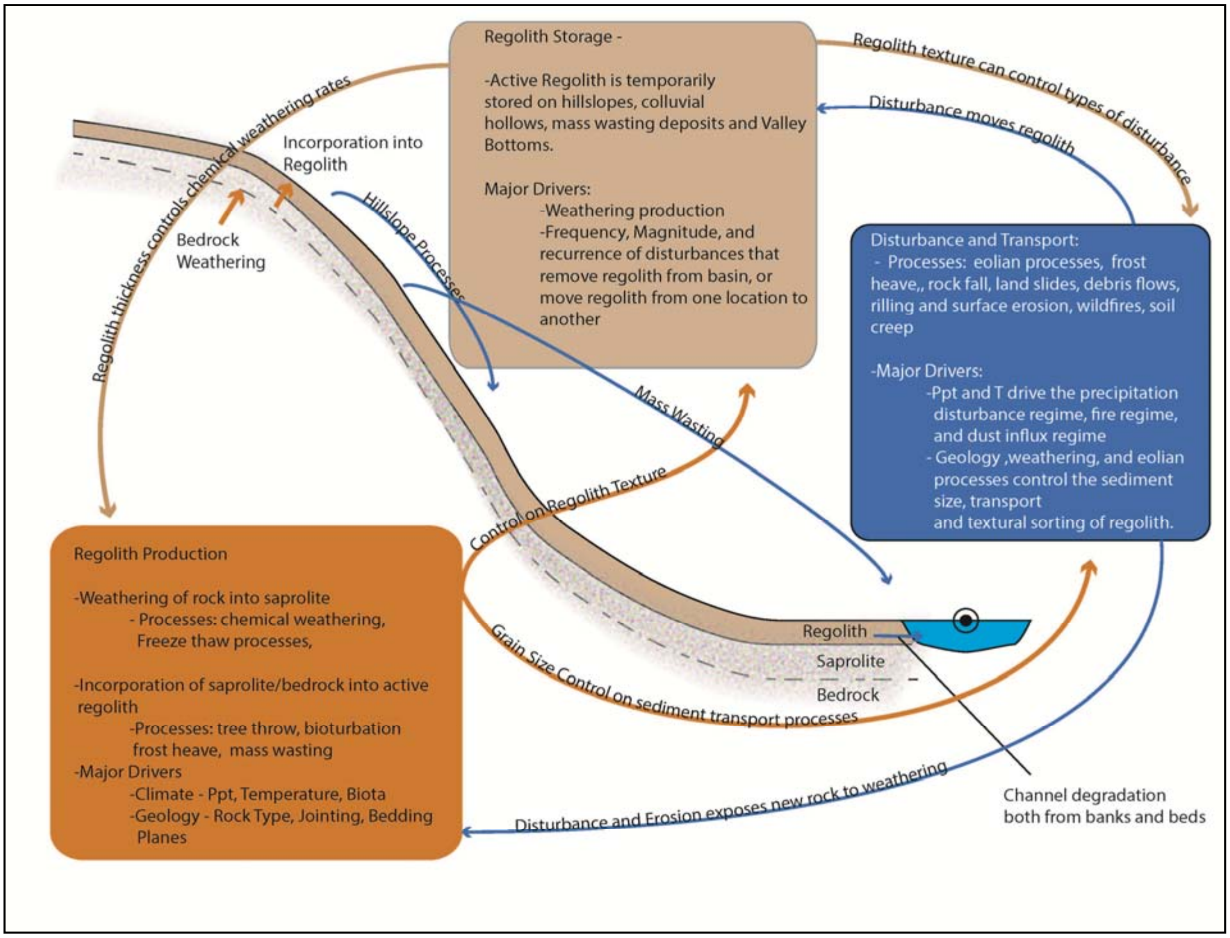

Figure 2: Conceptual illustration of the processes that a CRN-derived denudation rate integrates over long timescales. Arrows show the trajectory of each group of processes, and example feedbacks between each group of processes. Both climate and tectonics can play a significant role in each group of processes, and in turn these processes can influence each other. This speaks to the complexity in the concentration of CRNs in basin sediment, and how spatial and temporal heterogeneity in the processes and driving forces can affect the CRN signal.

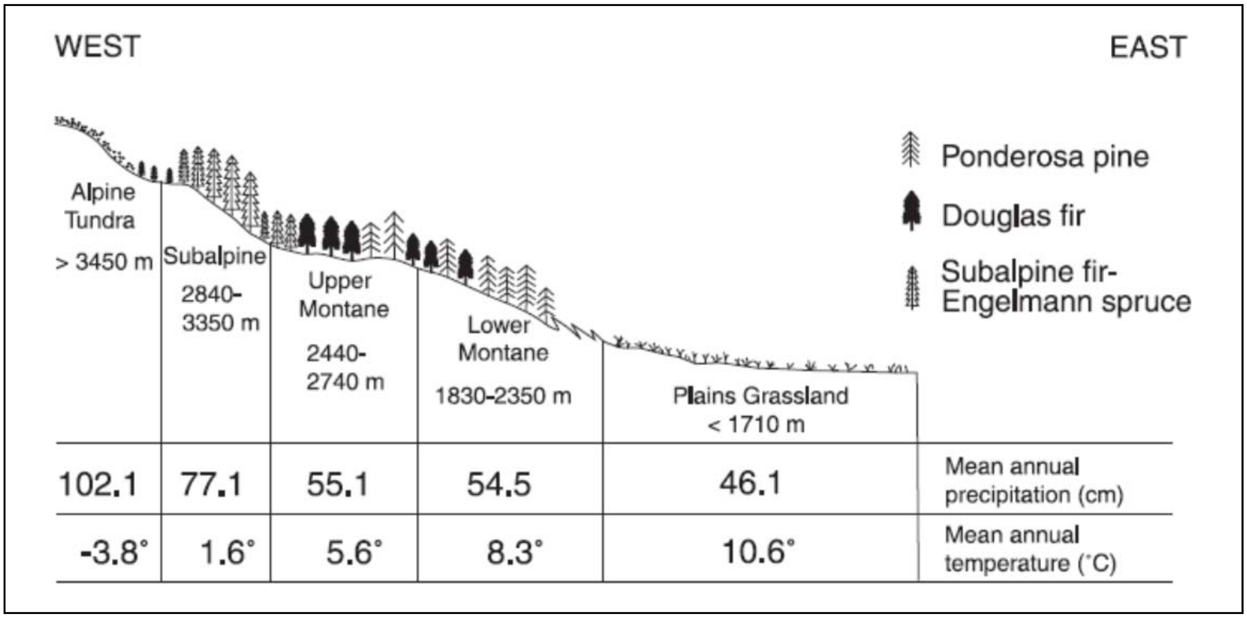

Figure 3: diagram of hydroclimatic and vegetation gradients with elevation from Birkeland et al. (2003) (Figure 2).

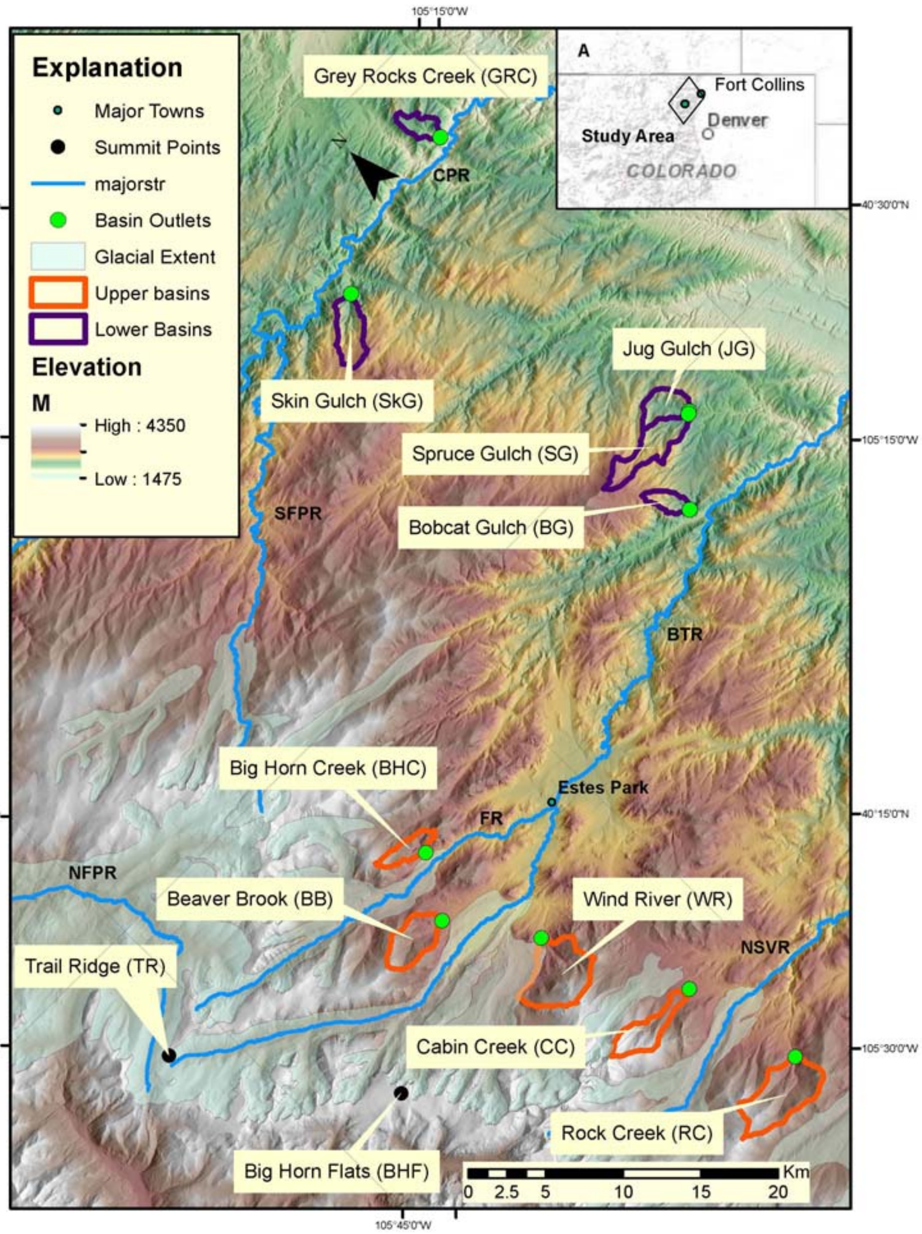

Figure 4: Study area map. Upper elevation basins are all above the farthest extent of the glacial moraine, but none lie in mapped glacial deposits (Madole et al., 1998). Note that the relief of the entire mountain range is ~3,000 m over 60 km, making it a striking topographic feature. Inset A shows the study area location within the region. Abbreviations for river names include: CPR – Cache la Poudre River, SFPR – South Fork, Cache la Poudre River, BTR – Big Thompson River, FR – Fall River, NSVR – North Saint Vrain Creek.

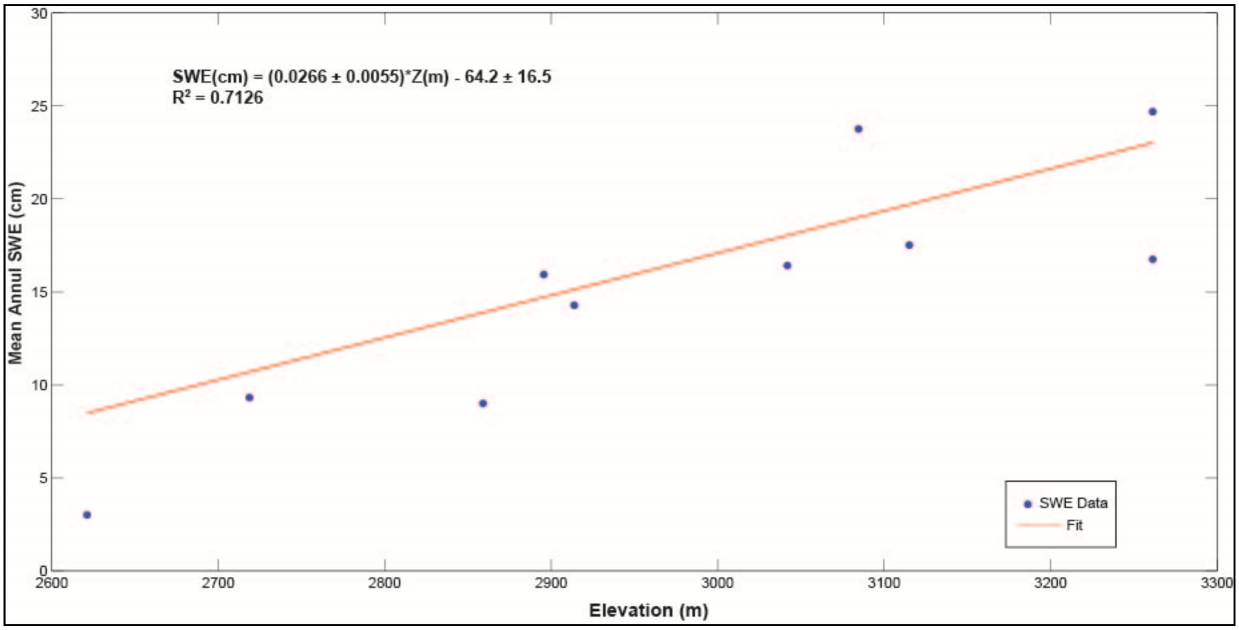

Figure 5: SWE vs elevation linear model for 10 nearby Snotels (Table 6). R^2 value shows that the SWE correlates relatively well with elevation. Use of this model assumes that the current pattern of mean annual SWE vs elevation has not changed over 10^4 yr time scales, a poor assumption but simpler than creating an SWE energy mass balance model.

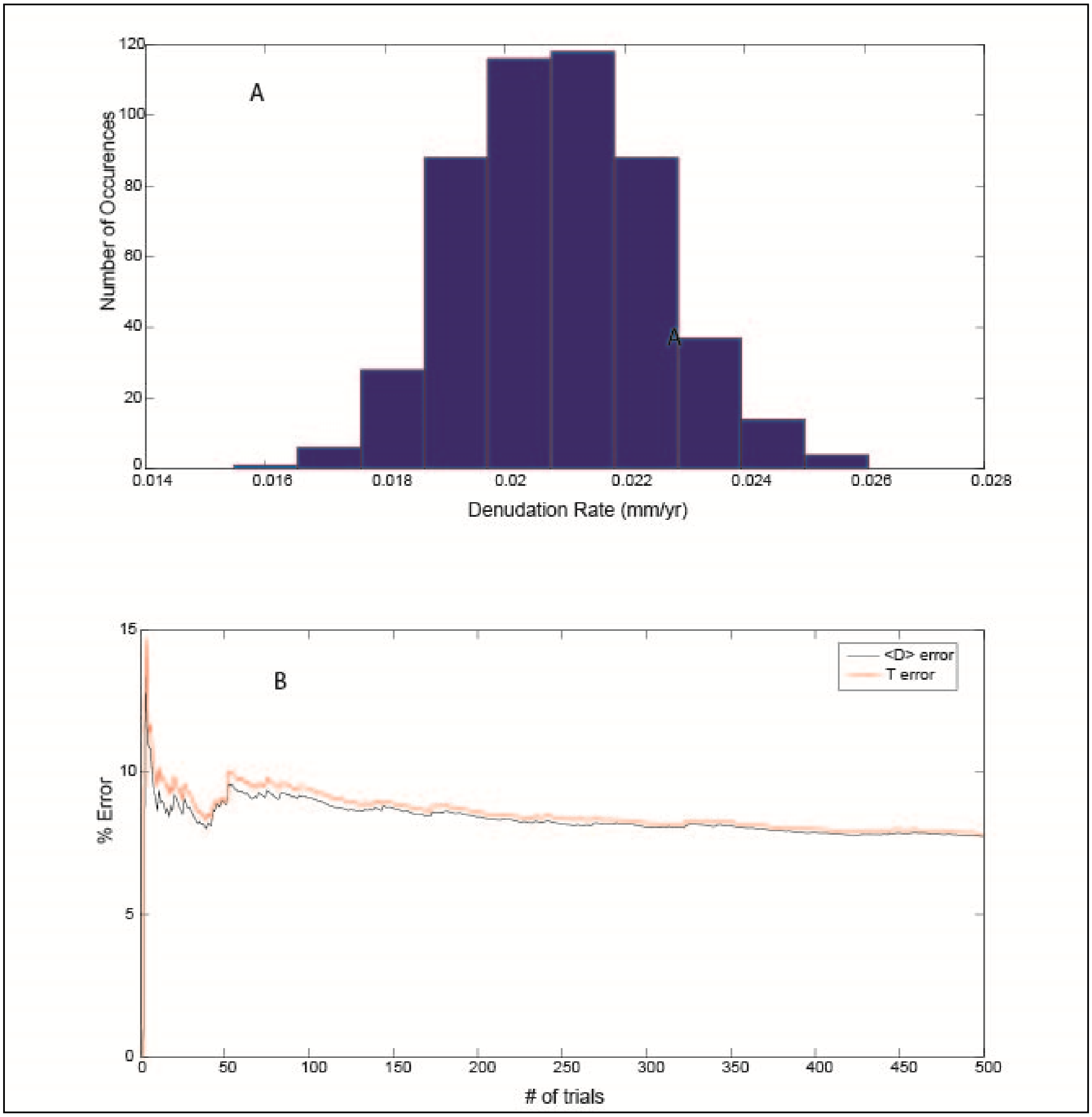

Figure 6: Monte Carlo Results from the Beaver Brook simulation. A) Histograms of Monte Carlo trial denudation rate solutions. The Monte Carlo simulations give a clearly normal grouping of solutions. B) Plot of the relative uncertainty for denudation rate (D) and timescale (T) as more trials are run during the simulation. The pattern shows clearly that the relative uncertainty is stabilizing by 500 trials.

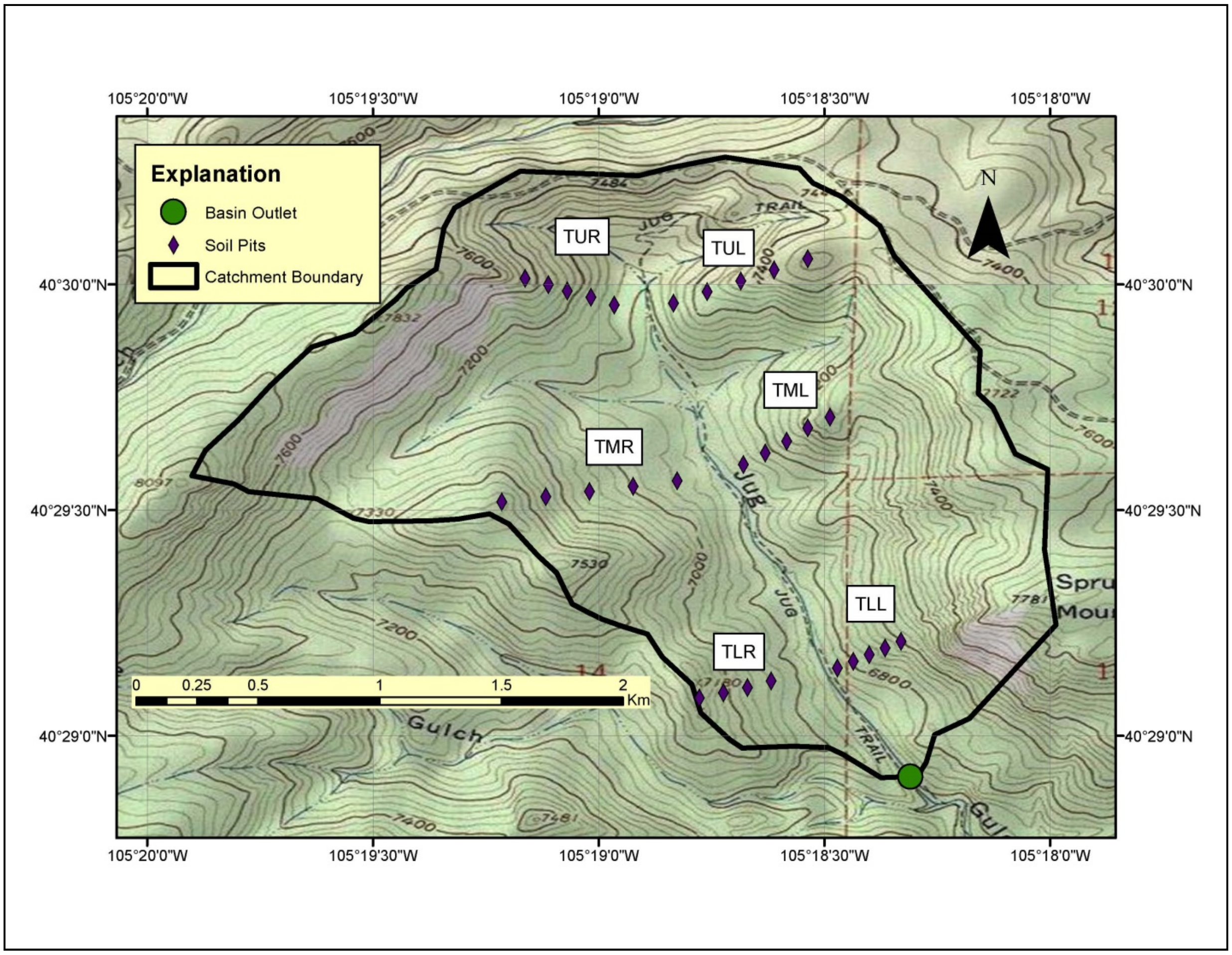

Figure 7: This map shows an example of the spatial distribution of regolith pits in the Jug Gulch study watershed. The base layer is ESRI's USA topo layer, which overlays USGS topographic quadrangle maps. Labels refer to the label of the transect. U, M, and L refer to upper, middle, and lower, while R and L correspond to river right and river left, respectively. The upper right (TUR) and lower left (TUL) transects do not proceed all the way to the top of the slope, because the slopes were capped with bedrock cliffs and very coarse talus cones. Therefore, the highest pit was placed at the base of the talus cone, assuming that was the *de facto* beginning of soil-mantled hillslope processes.

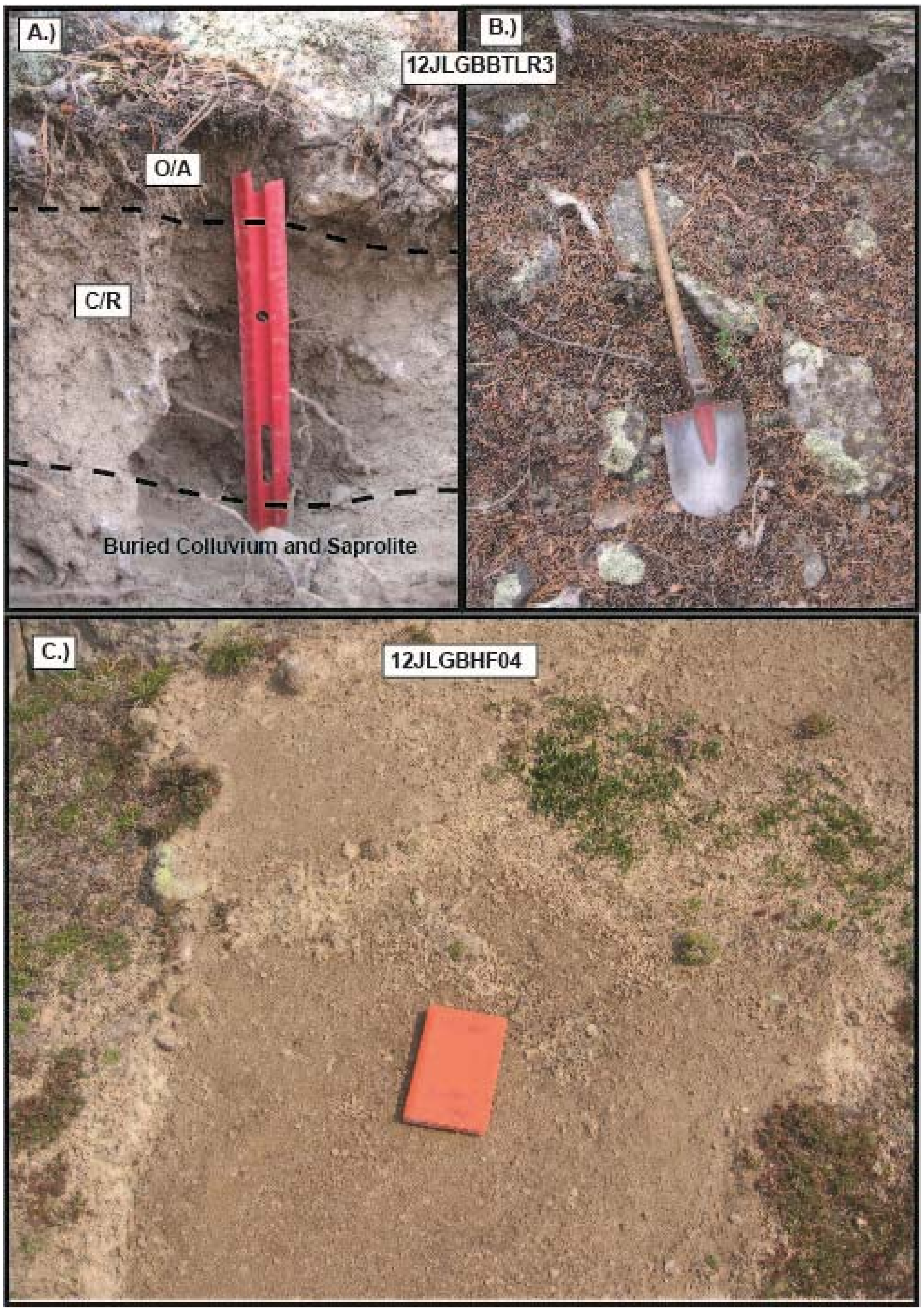

Figure 8: Example photographs of regolith pits. A) Soil profile of a Beaver Brook hillslope soil. This very undifferentiated regolith profile is the most common pattern observed in this study. B) Photo of site where A was dug. C) Example photo of surface regolith that was collected at Big Horn Flats for bulk geochemistry. Bare surface soil was collected in order to prevent disturbance of cryptobiotic soils. I also did this to collect mixed regolith at the surface, instead of surface soil that may only carry the geochemical signature of timescales much shorter than the cosmogenic regolith production rate.

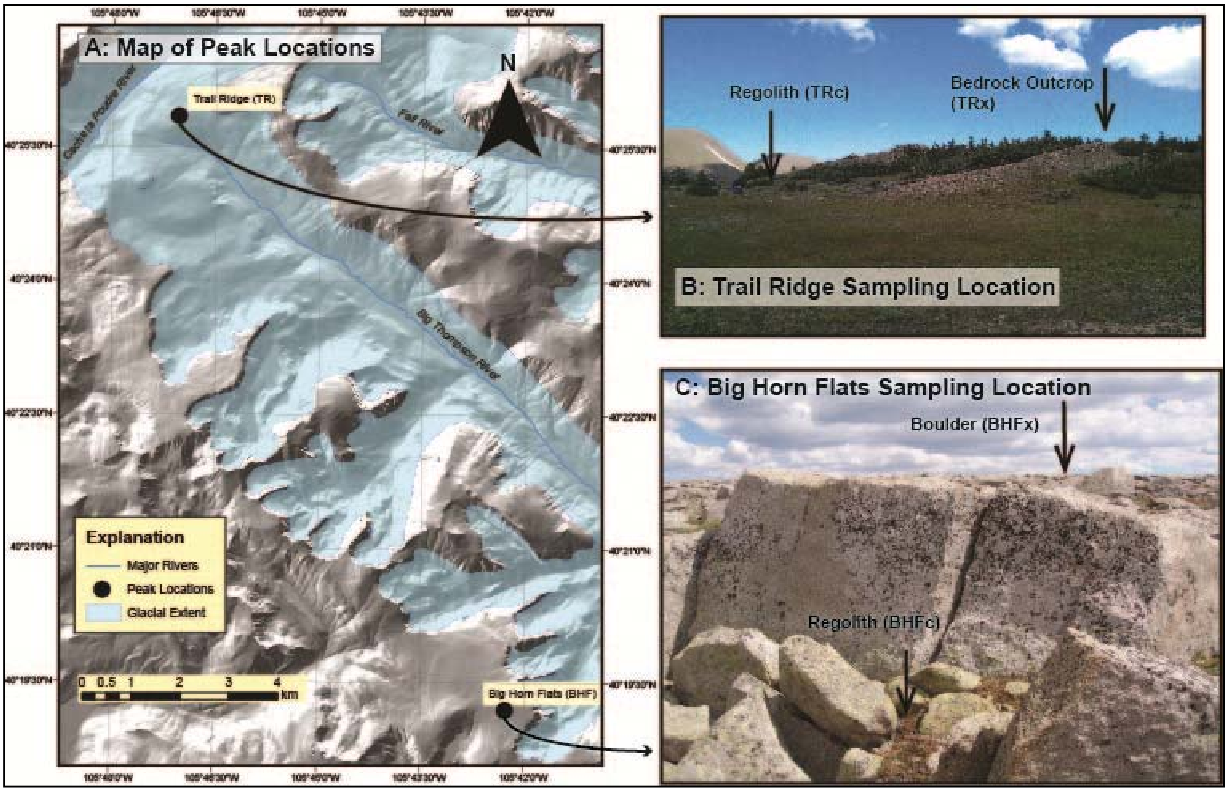

Figure 9: Peak sampling locations. A) Enlarged map of peak sampling locations. TR is mapped as Pleistocene glaciated terrain. The BHF sampling site is located at the center of a broad swath of the Rocky Mountain surface, with steep glacial cirques back wearing the location from the northeastern side. B) Photograph of TR site. Note that the outcrop is geomorphically connected to the regolith-mantled surface. The talus pile adjacent to the outcrop provides evidence of significant episodic erosion on the outcrop. C) Photograph of Big Horn Flats sampling site. The boulder is ~1 m above the surrounding surface. Large clasts show evidence of large episodic erosion on this boulder, as well as possible movement and repositioning of the boulder top.

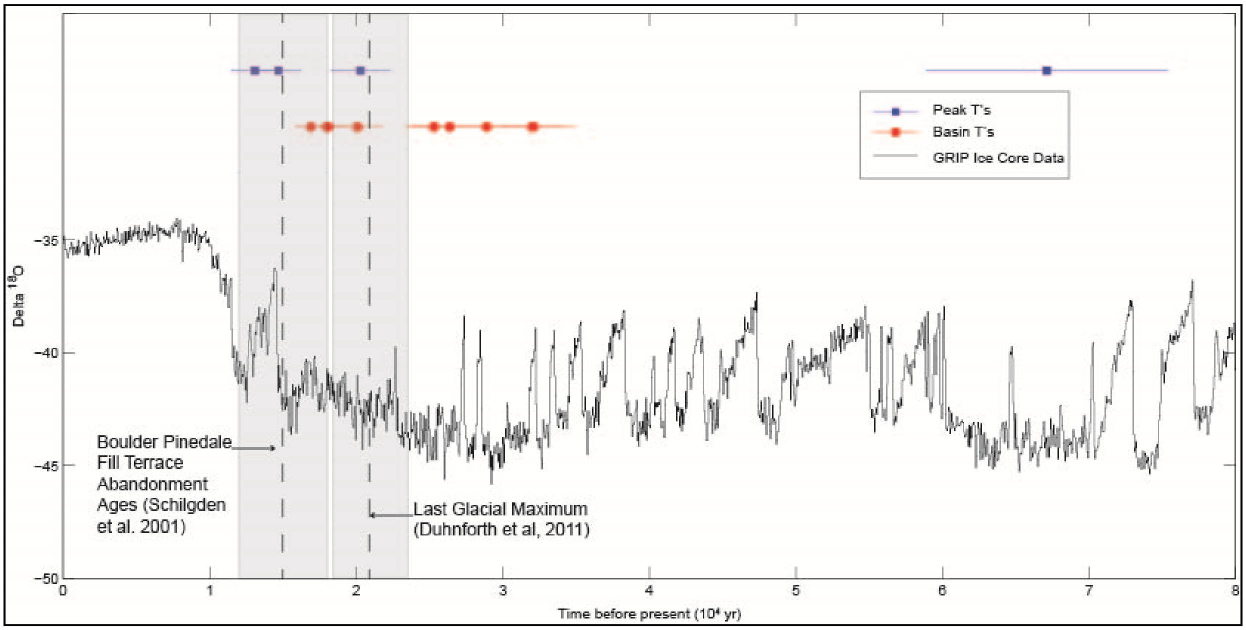

Figure 10: Time scale of denudation rates plotted against $\delta^{18}O$ from Greenland ice core data (Johnsen et al., 1997). Dotted lines show the approximate beginning of COFR glacial retreat (Duhnforth and Anderson, 2011) and abandonment of downstream canyon fill terraces (Schildgen et al., 2002). Grey bars show the standard deviation of moraine boulder ages (Duhnforth and Anderson, 2011) and the standard deviation of Pinedale fill terrace ages (Schildgen et al., 2002). Most of the basins (red data) span well into the Pleistocene glacial period, and therefore were subject to a significantly colder climate than the present. Warmer climates starting at ~11 kyr are thought to have brought greater amounts of higher intensity convective precipitation.

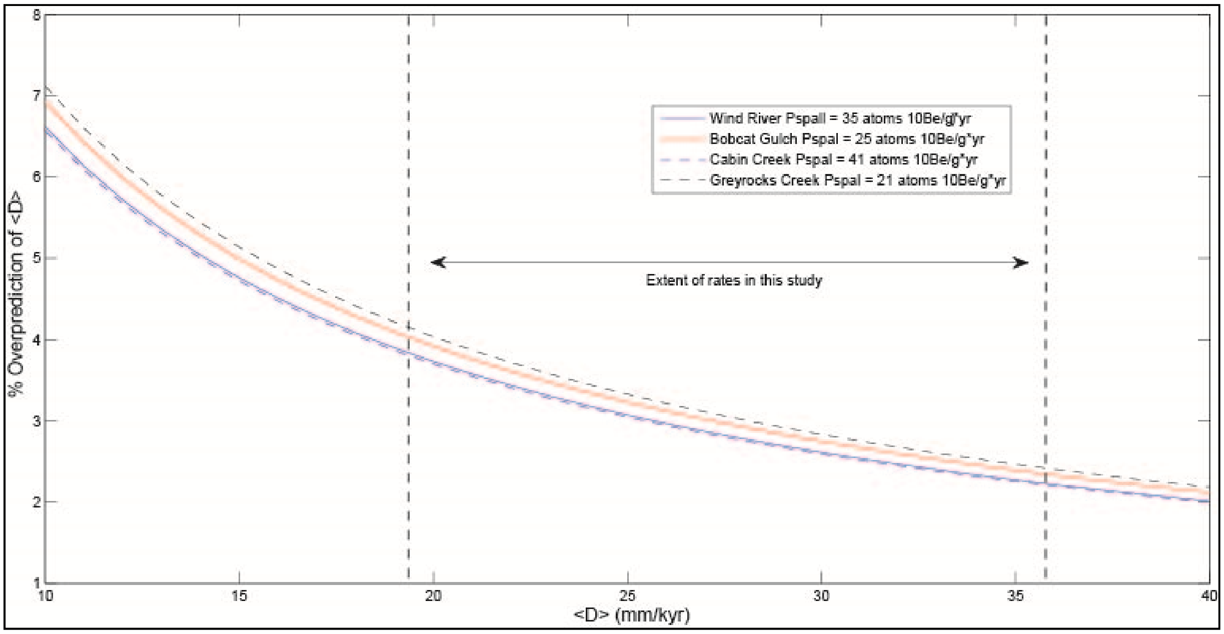

Figure 11: Percent error from the assumption of insignificant radioactive decay. The rates reported this study are overestimated by ~2-5%. Lower rates are more biased than faster rates, and the amount of uncertainty increases nonlinearly. Lower basins with lower production rates have more bias associated with the assumption of no radioactive decay.

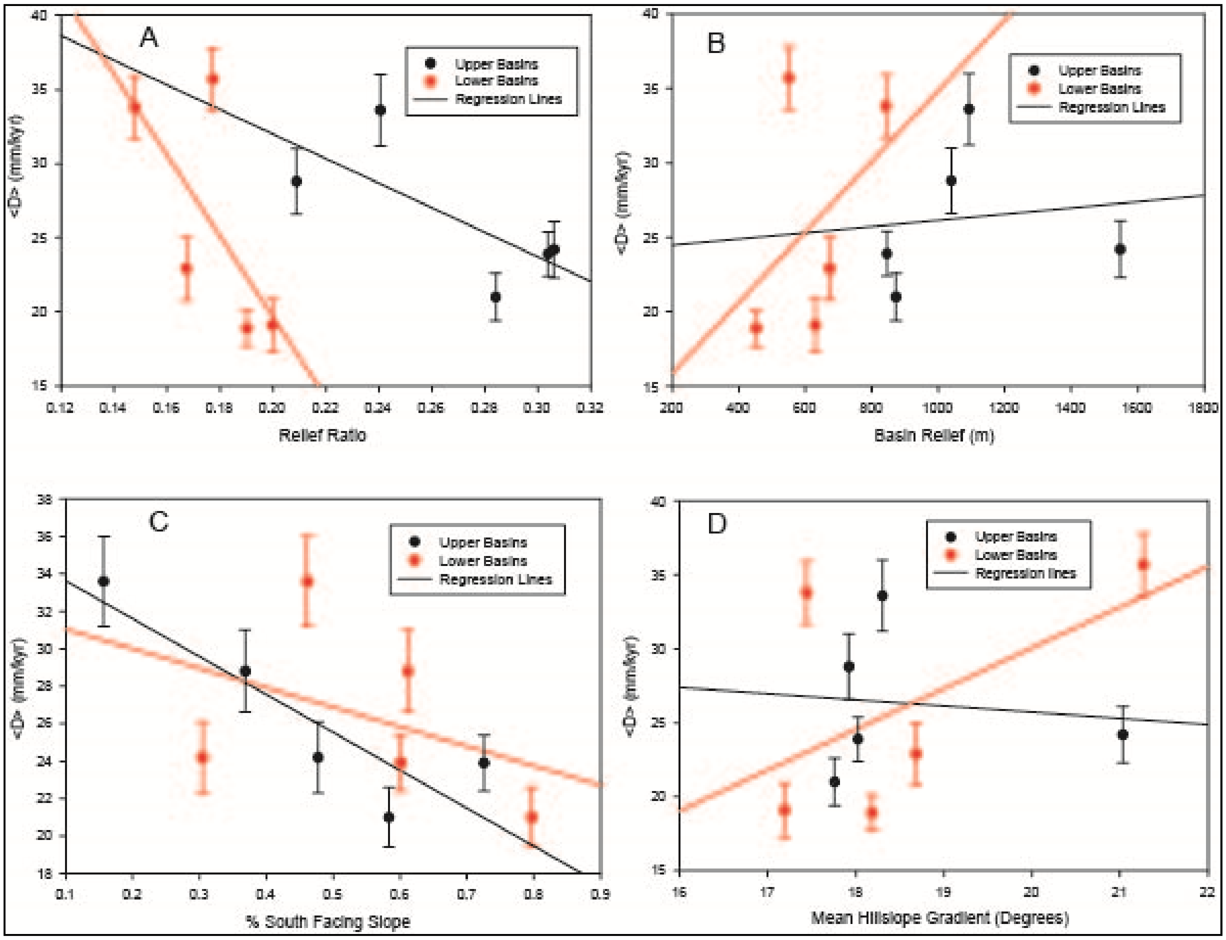

Figure 12: A comparison of selected morphometric parameters and denudation rates. Red points and best fit lines correspond to lower basins, while black corresponds to higher basins. R^2 values can be found in Table 9. RR shows good negative correlation with <D> (A), as well as upper basins and % south facing slope (C). HS and relief do not correlate well with <D>, which is contrary to several observations made elsewhere (Montgomery and Brandon, 2002).

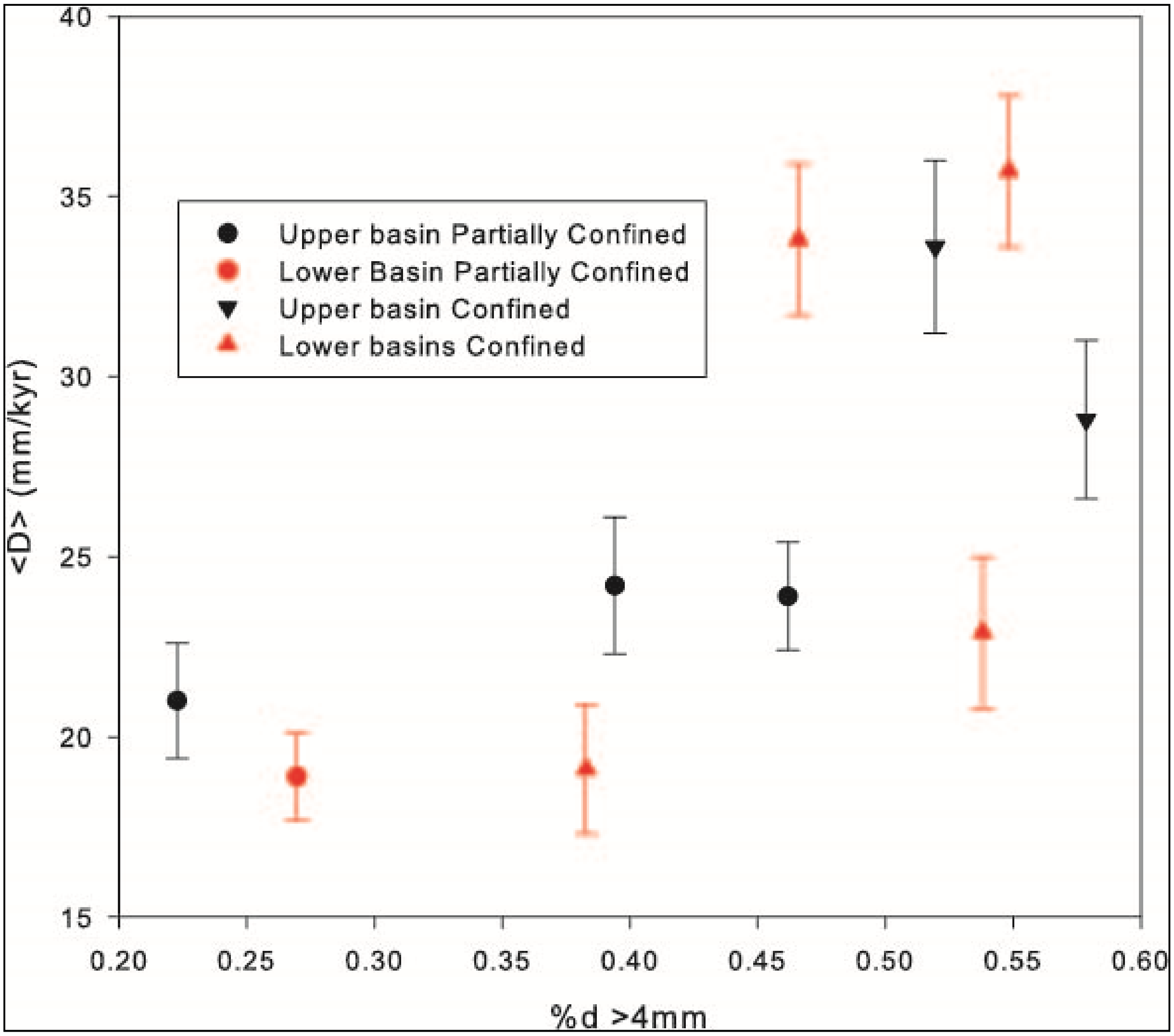

Figure 13: Relative proportions of coarse grain size fraction in CRN sample vs denudation rate. Black corresponds to upper basins and red corresponds to lower basins. Circles correspond to partially unconfined sampling locations and triangles represent confined sampling locations. The entire data set shows an increase in denudation rate with the relative fraction of coarse material, while unconfined reaches have lower denudation rates, and less coarse material that was collected. Confined reaches show much more variability in <D> and generally have coarser material.

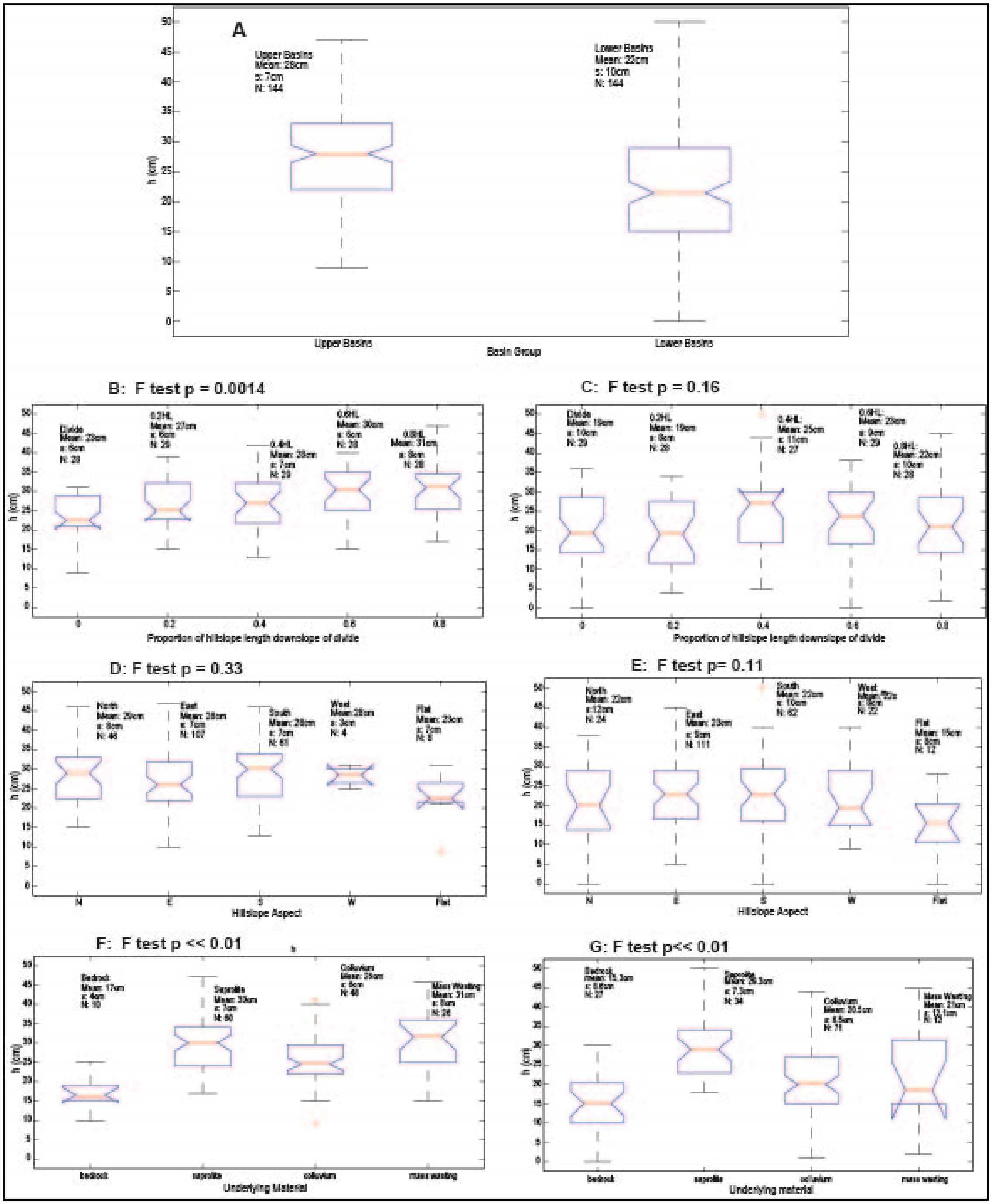

Figure 14: Box plots showing regolith distributions for the upper and lower basins, as well as along hillslope lengths. Notches in boxes delineate comparison intervals at the p = 0.05 level. Summary statistics for each box are also included in each graph. A) Upper basin h_R values are deeper with less variability. Upper basins also show a more distinct toposequence (B). Lower basin hillslopes seem mostly controlled by underlying material (G). Neither group seems to be controlled by aspect, except for lower regolith depth on flat surfaces, which equates to some divide samples. However, comparisons to flat aspect groups are limited by low sample sizes.

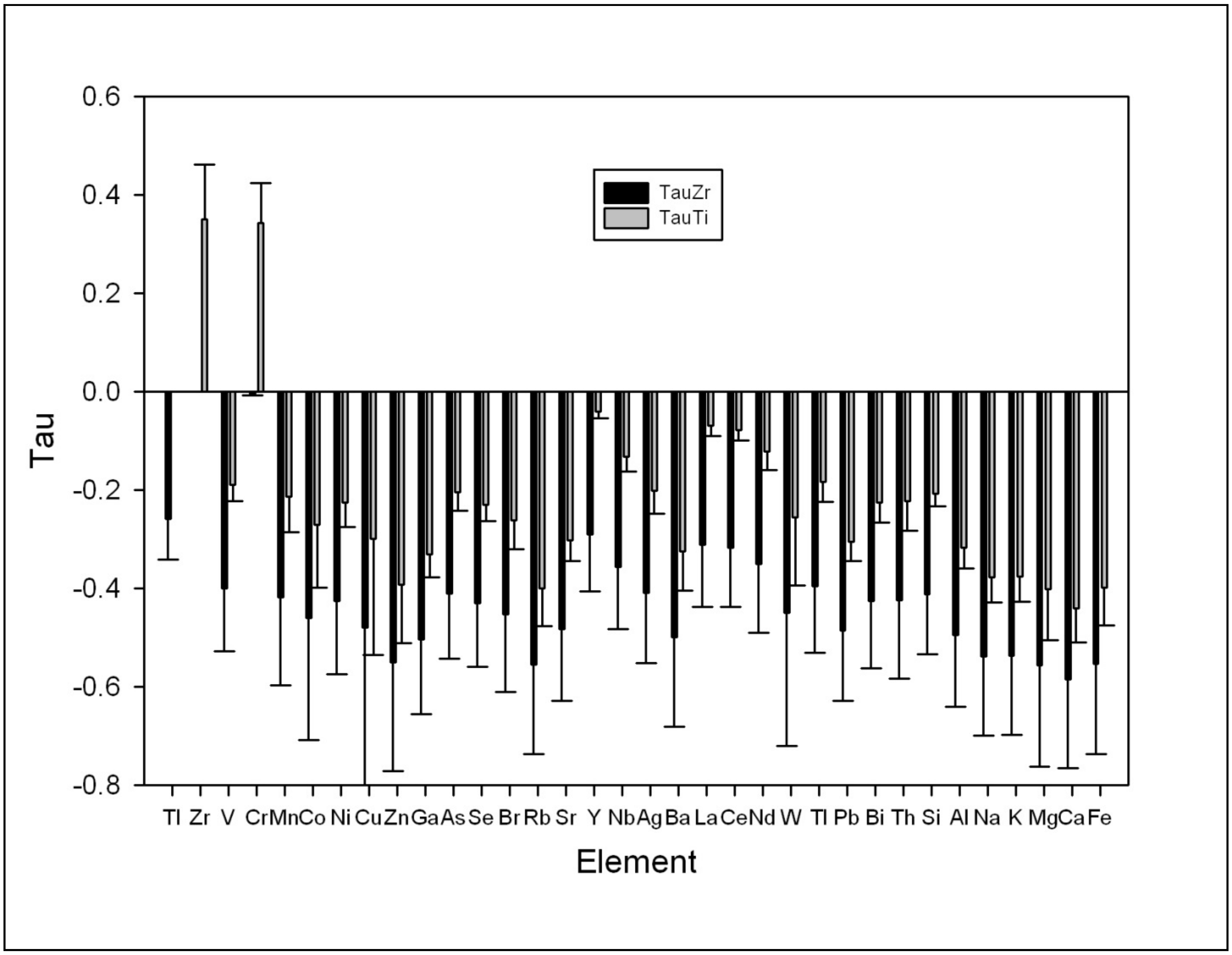

Figure 15: Values of τ calculated for each element measured in the XRF process. Dark Bars are τ values calculated with Zr, while grey bars represent τ values calculated with Ti. Values of τ calculated with Zr are much more negative, implying significant depletion and chemical weathering of these elements with respect to Zr. Ti is also significantly depleted with respect to Zr, indicating that the Ti/Zr ratio has changed.

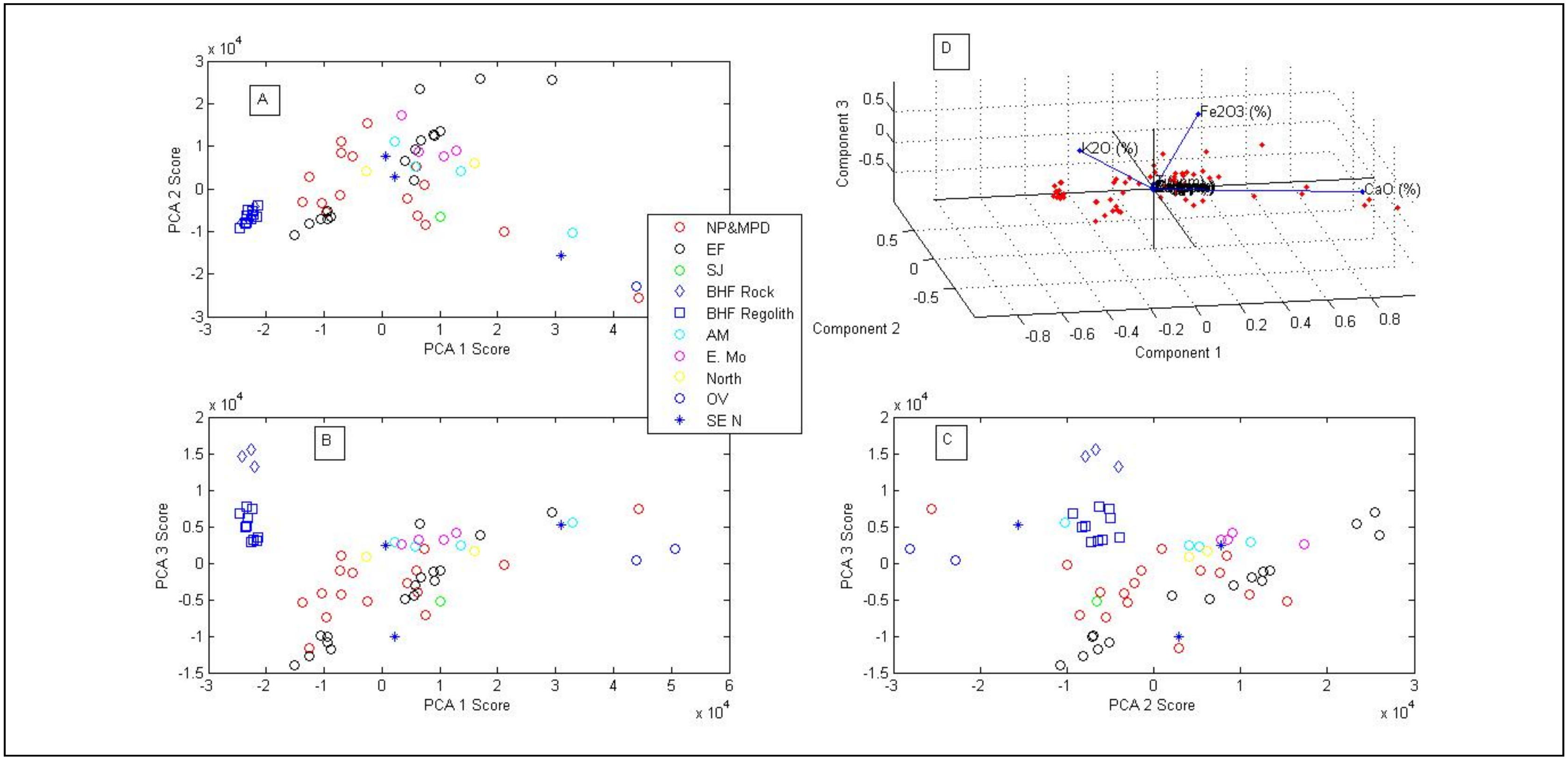

Figure 16: PCA results for trace and major elements. Results are represented as the bottom half of a scatter plot matrix (A, B and C) for the first three PC dimensions, as well as a biplot showing relative importance of variables (D). Bedrock samples are diamonds, regolith are squares, and dust are circles. A and B show that PC 1 dimension separates BHF samples from all potential dust sources, and is controlled by Ca, K and Fe. PC 3 shows separation between bedrock and regolith, and shows regolith data plotting closer to the groups of dust data. However, the relationship does not look very strong. This PC relationship is mostly governed by K concentrations.

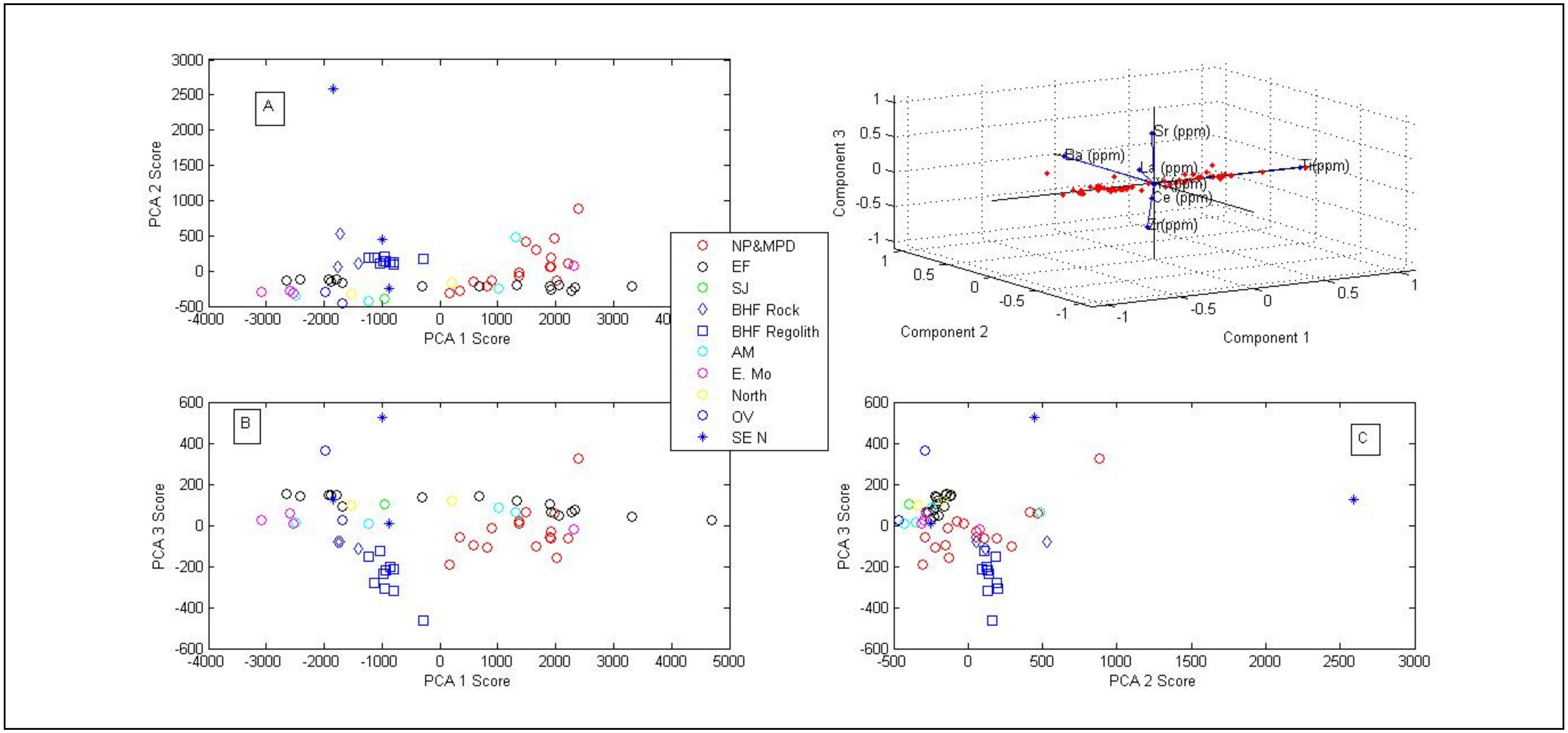

Figure 17: PCA results for trace and major elements. Results are represented as the bottom half of a scatter plot matrix (A, B and C) for the first three PC dimensions, as well as a biplot showing relative importance of variables (D). Bedrock samples are diamonds, regolith are squares, and dust are circles. Trace elements show separation between BHF samples and dust along PCA 1, which is governed by Ti concentrations. Little relationship between dust and BHF regolith composition is apparent in this analysis.

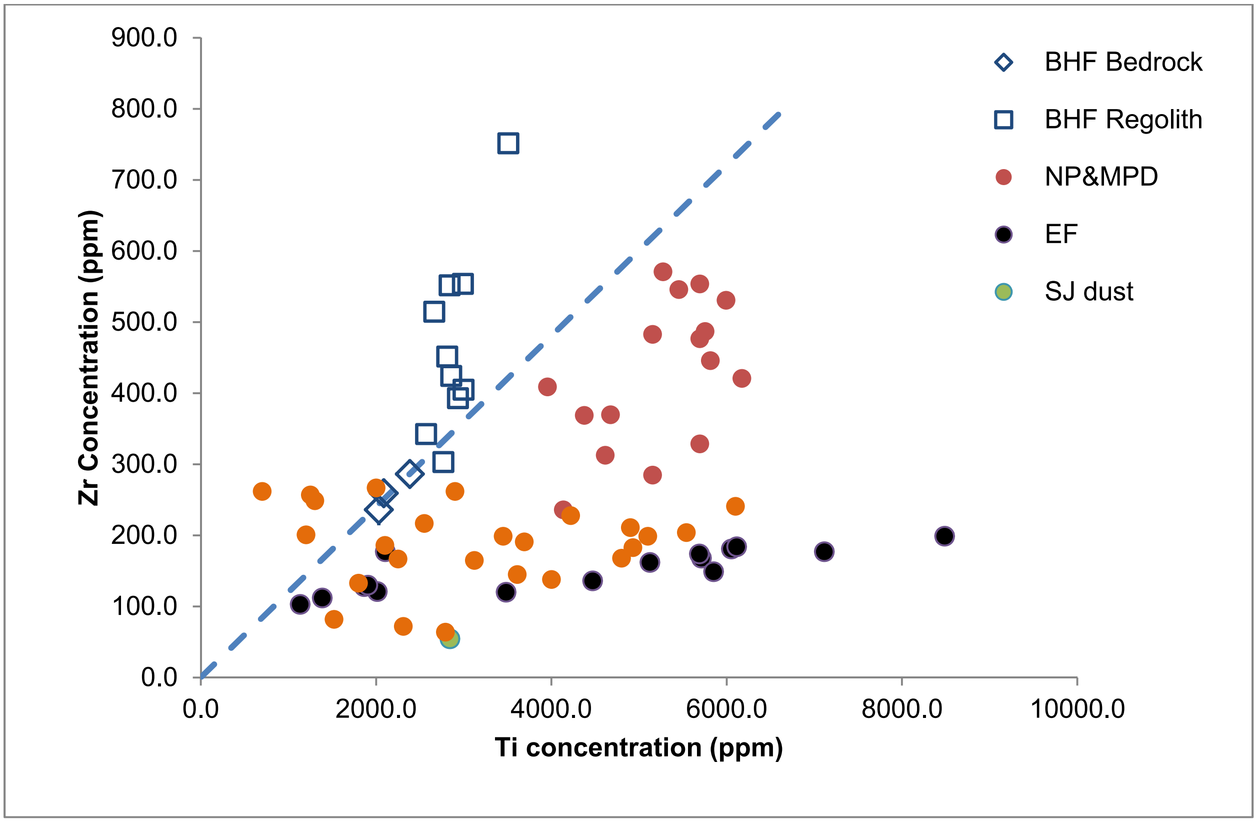

Figure 18: Plot of Zr concentrations vs Ti concentrations. Lines represent Ti/Zr ratios for BHF bedrock (blue) and SNSC dust data (Reheis, 1995). BHF Regolith generally plots above the Ti/Zr Bedrock line, implying inputs of Zr-rich dust. However, the vast majority of published dust chemistry data plot below the bedrock line, implying relative Ti enrichment.

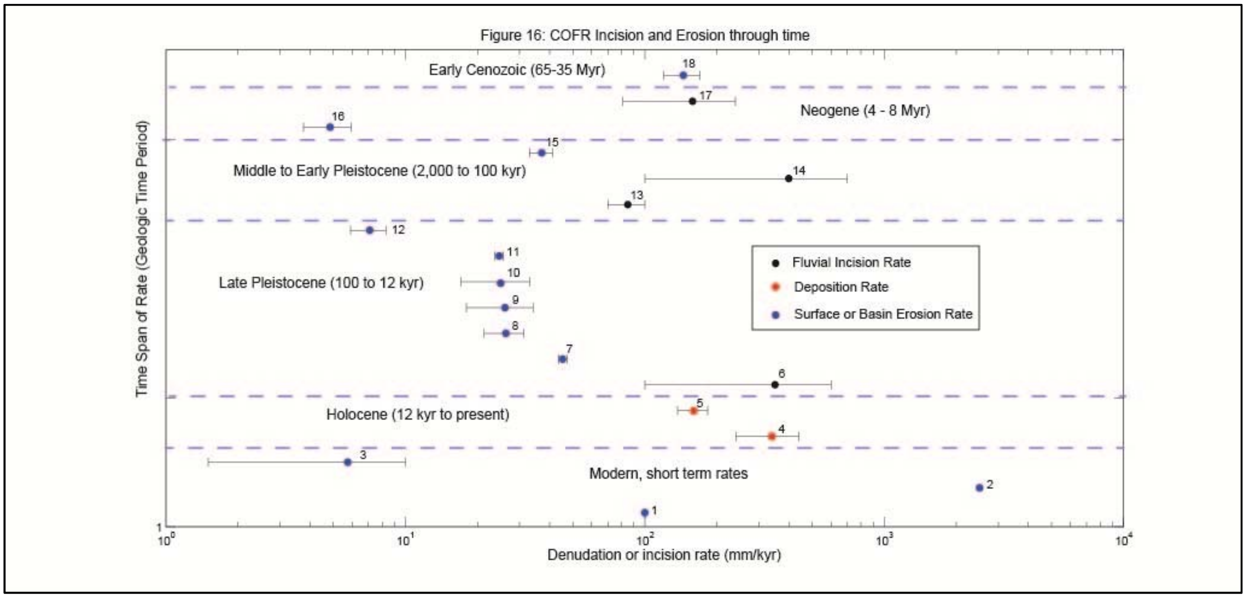

Figure 19: Comparison of regionally measured rates to rates in this study. Key for reference is below. The general trend shows higher denudation rates in the early Cenozoic, along with higher and more variable modern rates. Holocene deposition rates are also an order of magnitude higher than CRN-derived rates.

	Figure 19 KEY		
1	Bovis and Thorn 1981 (alpine soil loss)	10	Dethier and Lazarus (2006)
2	Moody and Martin 2001	11	Refsnider (2010) (Marble Mtn Summit Bedrock)
3	Moody and Martin background	12	Small et al (1997)
4	Polvi et al (2012)	13	Dethier, 2001
5	Menounos (2000)	14	Duhnforth et al (2012)
6	Schildgen et al (2002)	15	Refsnider (2010) (2 Pleistocene cave deposits)
7	Refsnider (2010) (Spanish Gulch Sediment)	16	Refsnider (2010) (Pliocene cave deposit)
8	***Upper Basins (this study)***	17	McMillan et al (2006)
9	***Lower Basins (this study)***	18	Pazzaglia and Kelley (1998)

10 Works Cited

Anderson, R. S., Anderson, S. P., & Tucker, G. E. (2012). Rock damage and regolith transport by frost: an example of climate modulation of the geomorphology of the critical zone. *Earth Surface Processes and Landforms*, *38*(3), 299-316

Anderson, R. S., Riihimaki, C. A., Safran, E. B. & MacGregor, K. R. (2006). Facing reality: Late Cenozoic evolution of smooth peaks, glacially ornamented valleys, and deep river gorges of Colorado's Front Range. *Special Papers-Geological Society of America*, *398*, 397-?.

Anderson, S. P., Dietrich, W. E., & Brimhall, G. H. (2002). Weathering profiles, mass-balance analysis, and rates of solute loss: Linkages between weathering and erosion in a small, steep catchment. *Geological Society of America Bulletin*, *114*(9), 1143-1158.

Balco, G., Stone, J. O., Lifton, N. A., & Dunai, T. J. (2008). A complete and easily accessible means of calculating surface exposure ages or erosion rates from ^{10}Be and ^{26}Al measurements. *Quaternary Geochronology*, *3*(3), 174-195.

Barry, R.G., (1973). A climatological transect on the east slope of the Front Range, Colorado. *Arctic and Alpine Research. 5*, 89– 110.

Belmont, P., Pazzaglia, F. & Gosse, J. (2007). Cosmogenic ^{10}Be as a tracer for hillslope and channel sediment dynamics in the Clearwater River, western Washington State. *Earth and Planetary Science Letters*, *264*(1), 123–135.

Binnie, S. A., Phillips, W. M., Summerfield, M. A. & Keith Fifield, L. (2006). Sediment mixing and basin-wide cosmogenic nuclide analysis in rapidly eroding mountainous environments. *Quaternary Geochronology*, *1*(1), 4–14.

Birkeland, P. W., Shroba, R. R., Burns, S. F., Price, A. B., & Tonkin, P. J. (2003). Integrating soils and geomorphology in mountains—an example from the Front Range of Colorado. *Geomorphology*, *55*(1), 329-344.

Blott, S. J., & Pye, K. (2001). GRADISTAT: a grain size distribution and statistics package for the analysis of unconsolidated sediments. *Earth surface processes and Landforms*, *26*(11), 1237-1248.

Bovis, M. (1978). Soil loss in the Colorado Front Range: Sampling design and areal variation. *Zeitschr. f. Geomorph., Suppl. Bd*, *29*, 10–21.

Bovis, M.J., Thorn, C.E., 1981. Soil loss variation within a Colorado alpine area. *Earth Surface Processes and Landforms, 6(2)*, 151– 163.

Brimhall, G. H., & Dietrich, W. E. (1987). Constitutive mass balance relations between chemical composition, volume, density, porosity, and strain in metasomatic hydrochemical systems: results on weathering and pedogenesis. *Geochimica et Cosmochimica Acta*, *51*(3), 567-587.

Burbank, D. W., Leland, J., Fielding, E., Anderson, R. S., Brozovic, N., Reid, M. R. & Duncan, C. (1996). Bedrock incision, rock uplift and threshold hillslopes in the northwestern Himalayas. *Nature*, *379*(6565), 505–510.

Butler, B.E., 1982. A new system for soil studies. *Journal of Soil Science, 33*, 581-595.

Caine, N. (1984). Elevational contrasts in contemporary geomorphic activity in the Colorado Front Range. *Studia Geomorphologica Carpatho-Balcanica*, *18*, 5–31.

Capesius, J.P., and Stephens, V.C. (2009) Regional regression equations for estimation of natural streamflow statistics in Colorado: U.S. Geological Survey Scientific Investigations Report 2009–5136.

Carson, M.A., and Kirkby, M.J. Hillslope form and process. 1973 *New York, Cambridge University Press*.

Clow, D. W., & Sueker, J. K. (2000). Relations between basin characteristics and stream water chemistry in alpine/subalpine basins in Rocky Mountain National Park, Colorado. *Water Resources Research*, *36*(1), 49-61.

Dethier, D. P. & Lazarus, E. D. (2006). Geomorphic inferences from regolith thickness, chemical denudation and CRN erosion rates near the glacial limit, Boulder Creek catchment and vicinity, Colorado. *Geomorphology*, *75*(3), 384–399.

Dethier, D. P. (2001). Pleistocene incision rates in the western United States calibrated using Lava Creek B tephra. *Geology*, *29*(9), 783-786.

Dühnforth, M., Anderson, R. S., Ward, D. J., & Blum, A. (2012). Unsteady late Pleistocene incision of streams bounding the Colorado Front Range from measurements of meteoric and in situ 10Be. *Journal of Geophysical Research: Earth Surface (2003–2012)*, *117*(F1).

Dühnforth, M. & Anderson, R. S. (2011). Reconstructing the Glacial History of Green Lakes Valley, North Boulder Creek, Colorado Front Range. *Arctic, Antarctic, and Alpine Research*, *43*(4), 527–542.

Dunai, T. J. (2000). Scaling factors for production rates of in situ produced cosmogenic nuclides: a critical reevaluation. *Earth and Planetary Science Letters*, *176*(1), 157-169.

Dunne, J., Elmore, D. & Muzikar, P. (1999). Scaling factors for the rates of production of cosmogenic nuclides for geometric shielding and attenuation at depth on sloped surfaces. *Geomorphology*, *27*(1), 3–11.

Ehlen, J., & Wohl, E. (2002). Rock Control in Geomorphological Processes. Joints and Landform Evolution in Bedrock Canyons. *Transactions*, *23*(2), 237-255.

Everitt, B. S., & Dunn, G. (2001). Applied Multivariate Data Analysis. 2001. *Arnold, London*.

Ferrier, K. L., Kirchner, J. W. & Finkel, R. C. (2011). Estimating millennial-scale rates of dust incorporation into eroding hillslope regolith using cosmogenic nuclides and immobile weathering tracers. *Journal of Geophysical Research*, *116*(F3), F03022.

Frankel, K. L. & Pazzaglia, F. J. (2006). Mountain fronts, base-level fall, and landscape evolution: Insights from the southern Rocky Mountains. *Special Papers-Geological Society of America*, *398*, 419.

Frankel, K. L. & Pazzaglia, F. J. (2005). Tectonic geomorphology, drainage basin metrics, and active mountain fronts. *Geografia Fisica e Dinamica Quaternaria (Testo stampato)*, *28*(1), 7–21.

Friedman, I., Carrara, P., & Gleason, J. (1988). Isotopic evidence of Holocene climatic change in the San Juan Mountains, Colorado. *Quaternary Research*, *30*(3), 350-353.

Granger, D. E., Kirchner, J. W., & Finkel, R. (1996). Spatially averaged long-term erosion rates measured from in situ-produced cosmogenic nuclides in alluvial sediment. *The Journal of Geology*, *104*, 249-257.

Granger, D. E. and C. S. Riebe (2007). Cosmogenic Nuclides in Weathering and Erosion. *Treatise on Geochemistry*, 5, 1-43.

Godt, J. W. & Coe, J. A. (2007). Alpine debris flows triggered by a 28 July 1999 thunderstorm in the central Front Range, Colorado. *Geomorphology*, *84*(1), 80–97.

Goldstein, H. L., Reynolds, R. L., Reheis, M. C., Yount, J. C. & Neff, J. C. (2008). Compositional trends in aeolian dust along a transect across the southwestern United States. *Journal of Geophysical Research: Earth Surface (2003-2012)*, 113(F2).

Gosse, J. C., & Phillips, F. M. (2001). Terrestrial in situ cosmogenic nuclides: theory and application. *Quaternary Science Reviews*, *20*(14), 1475-1560.

Gregory, K. M. & Chase, C. G. (1994). Tectonic and climatic significance of a late Eocene low-relief, high-level geomorphic surface, Colorado. *Journal of Geophysical Research: Solid Earth (1978-2012)*, *99*(B10), 20141–20160.

Grimm, M. M., Wohl, E. E. & Jarrett, R. D. (1995). Coarse-sediment distribution as evidence of an elevation limit for flash flooding, Bear Creek, Colorado. *Geomorphology*, *14*(3), 199–210.

Hack, J. T. (1973). Stream-profile analysis and stream-gradient index. *J. Res. US Geol. Surv*, *1*(4), 421–429.

Hadley, R. & Schumm, S. (1961). Sediment Sources and Drainage Basin Characteristincs in Upper Cheyenne River Basin. *US Geol. Survey Water-Supply Paper*.

Heimsath, A. M. (2006). Eroding the land: steady-state and stochastic rates and processes through a cosmogenic lens. *Special Papers-Geological Society of America*, 415, 111. Boulder, Colo.; Geological Society of America; 1999-?.

Henkle, J. E., Wohl, E. & Beckman, N. (2011). Locations of channel heads in the semiarid Colorado Front Range, USA. *Geomorphology*, *129*(3), 309–319.

Johnsen, S. J., Clausen, H. B., Dansgaard, W., Gundestrup, N. S., Hammer, C. U., Andersen, U., Anderson, K. K., Hvidberg, C. S., Dahl-Jensen, D., Steffensen, J. P., Shoji, H., Sveinbjörnsdóttir, A. E., White, J. W. C., Jouzel, J. & Fisher, D. (1997). The δ18O record along the Greenland Ice Core Project deep ice core and the problem of possible Eemian climatic instability. *Journal of Geophysical Research*, *102*(C12), 26397-26.

Jewell, P. W. & Nicoll, K. (2011). Wind regimes and aeolian transport in the Great Basin, USA. *Geomorphology*, *129*(1), 1–13.

Kelley, S. & Chapin, C. (2004). Denudation history and internal structure of the Front Range and Wet Mountains, Colorado, based on apatite-fission-track thermochronology. *Tectonics, geochronology, and volcanism in the Southern Rocky Mountains and Rio Grande rift: New Mexico Bureau of Geology and Mineral Resources Bulletin*, *160*, 41–77.

Kohl, C. P., & Nishiizumi, K. (1992). Chemical isolation of quartz for measurement of *in-situ* produced cosmogenic nuclides. *Geochimica et Cosmochimica Acta*, *56*(9), 3583-3587.

Lawrence, C. R., Painter, T., Landry, C. & Neff, J. (2010). Contemporary geochemical composition and flux of aeolian dust to the San Juan Mountains, Colorado, United States. *Journal of Geophysical Research: Biogeosciences (2005-2012)*, *115*(G3).

Ley, R. E., Williams, M. W. & Schmidt, S. K. (2004). Microbial population dynamics in an extreme environment: controlling factors in talus soils at 3750 m in the Colorado Rocky Mountains. *Biogeochemistry*, *68*(3), 297–311.

Madole, R.F., VanSistine, D. Paco, and Michael, J.A. (1998). Pleistocene glaciation in the upper Platte River drainage basin, Colorado. *U.S. Geological Survey Geologic Investigations Series, I-2644.*

Matmon, A., Bierman, P., Larsen, J., Southworth, S., Pavich, M., Finkel, R. & Caffee, M. (2003). Erosion of an ancient mountain range, the Great Smoky Mountains, North Carolina and Tennessee. *American Journal of Science*, *303*(9), 817–855.

McMillan, M. E., Heller, P. L. & Wing, S. L. (2006). History and causes of post-Laramide relief in the Rocky Mountain orogenic plateau. *Geological Society of America Bulletin*, *118*(3-4), 393–405.

Menounos, B. (2000). A Holocene Debris-Flow Chronology for an Alpine Catchment, Colorado Front Range. *Geomorphology, human activity, & global environmental change*, Wiley & Sons, pp. 117-149

Montgomery, D. R. (1999). PROCESS DOMAINS AND THE RIVER CONTINUUM. *JAWRA Journal of the American Water Resources Association*, *35*(2), 397-410.

Montgomery, D. R. & Brandon, M. T. (2002). Topographic controls on erosion rates in tectonically active mountain ranges. *Earth and Planetary Science Letters*, *201*(3), 481–489.

Moody, J. A., & Martin, D. A. (2001). Initial hydrologic and geomorphic response following a wildfire in the Colorado Front Range. *Earth Surface Processes and Landforms*, *26*(10), 1049-1070.

Muhs, D. R. & Benedict, J. B. (2006). Eolian additions to late quaternary alpine soils, Indian peaks wilderness area, Colorado front range. *Arctic, Antarctic, and Alpine Research*, *38*(1), 120–130.

Neff, J. C., et al. (2008), Increasing eolian dust deposition in the western United States linked to human activity, *Nature Geoscience*, *1*(3), 189–195.

Niemi, N. A., Oskin, M., Burbank, D. W., Heimsath, A. M. & Gabet, E. J. (2005). Effects of bedrock landslides on cosmogenically determined erosion rates. *Earth and Planetary Science Letters*, *237*(3), 480–498.

Ott, L., & Longnecker, M. (2010). *An introduction to statistical methods and data analysis*. Brooks/Cole.

Ouimet, W. B., Whipple, K. X. & Granger, D. E. (2009). Beyond threshold hillslopes: Channel adjustment to base-level fall in tectonically active mountain ranges. *Geology*, *37*(7), 579–582.

Parker, G. & Perg, L. (2005). Probabilistic formulation of conservation of cosmogenic nuclides: effect of surface elevation fluctuations on approach to steady state. *Earth Surface Processes and Landforms*, *30*(9), 1127–1144.

Pazzaglia, F. J., & Kelley, S. A. (1998). Large-scale geomorphology and fission-track thermochronology in topographic and exhumation reconstructions of the Southern Rocky Mountains. *Rocky Mountain Geology*, *33*(2), 229-257.

Polvi, L. E., & Wohl, E. (2012). The beaver meadow complex revisited–the role of beavers in post-glacial floodplain development. *Earth Surface Processes and Landforms*, *37*(3), 332-346.

Reheis, M. C., Budahn, J. R., Lamothe, P. J. & Reynolds, R. L. (2009). Compositions of modern dust and surface sediments in the Desert Southwest, United States. *Journal of Geophysical Research: Earth Surface (2003-2012)*, *114*(F1).

Reheis, M. C., & Kihl, R. (1995). Dust deposition in southern Nevada and California, 1984–1989: Relations to climate, source area, and source lithology.*Journal of Geophysical Research: Atmospheres (1984–2012)*, *100*(D5), 8893-8918.

Refsnider, K. A. (2010). Dramatic increase in late Cenozoic alpine erosion rates recorded by cave sediment in the southern Rocky Mountains. *Earth and Planetary Science Letters*, *297*(3), 505–511.

Reusser, L. J., Bierman, P. R., Pavich, M. J., Zen, E. A., Larsen, J., & Finkel, R. (2004). Rapid Late Pleistocene incision of Atlantic passive-margin river gorges. *Science*, *305*(5683), 499-502.

Rossi, B. (1948). Interpretation of cosmic-ray phenomena. *Reviews of Modern Physics*, *20*(3), 537.

Riebe, C. S., Kirchner, J. W. & Finkel, R. C. (2003). Long-term rates of chemical weathering and physical erosion from cosmogenic nuclides and geochemical mass balance. *Geochimica et Cosmochimica Acta*, *67*(22), 4411–4427.

Riebe, C. S., & Granger, D. E. (2012). Quantifying effects of deep and near-surface chemical erosion on cosmogenic nuclides in soils, saprolite, and sediment. *Earth Surface Processes and Landforms*, *38*(5), 523-533.

Ritter, D. F., Kochel, R. C., & Miller, J. R. (2002). *Process geomorphology* (4th ed., p. 546). Dubuque, IA: Wm. C. Brown.

Safran, E. B., Bierman, P. R., Aalto, R., Dunne, T., Whipple, K. X. & Caffee, M. (2005). Erosion rates driven by channel network incision in the Bolivian Andes. *Earth Surface Processes and Landforms*, *30*(8), 1007–1024.

Schaller, M. & Ehlers, T. (2006). Limits to quantifying climate driven changes in denudation rates with cosmogenic radionuclides. *Earth and Planetary Science Letters*, *248*(1), 153–167.

Schildgen, T., Dethier, D. P., Bierman, P. & Caffee, M. (2002). 26Al and 10Be dating of late pleistocene and holocene fill terraces: A record of fluvial deposition and incision, Colorado front range. *Earth Surface Processes and Landforms*, *27*(7), 773–787.

Schildgen, T., Phillips, W. & Purves, R. (2005). Simulation of snow shielding corrections for cosmogenic nuclide surface exposure studies. *Geomorphology*, *64*(1), 67–85.

Schwanghart, W., & Kuhn, N. J. (2010). TopoToolbox: A set of Matlab functions for topographic analysis. *Environmental Modelling & Software*, *25*(6), 770-781.

Scott, G.R., and Taylor, R.B., 1986, Map showing late Eocene erosion surface, Oligocene-Miocene paleovalleys, and Tertiary deposits in the Pueblo, Denver, and Greeley 1′ × 2′quadrangles, Colorado: U.S. Geological Survey Miscellaneous Investigations Map I-1626, scale 1:250,000.

Small, E. E., Anderson, R. S., Repka, J. L. & Finkel, R. (1997). Erosion rates of alpine bedrock summit surfaces deduced from in situ ^{10}Be and ^{26}Al. *Earth and Planetary Science Letters*, *150*(3), 413–425.

Small, E. E., Anderson, R. S., & Hancock, G. S. (1999). Estimates of the rate of regolith production using 10Be and 26Al from an alpine hillslope. *Geomorphology*, *27*(1), 131-150.

Stock, G. M., Frankel, K. L., Ehlers, T. A., Schaller, M., Briggs, S. M. & Finkel, R. C. (2009). Spatial and temporal variations in denudation of the Wasatch Mountains, Utah, USA. *Lithosphere*, *1*(1), 34–40.

Stone, J. O. (2000). Air pressure and cosmogenic isotope production. *Journal of Geophysical Research*, *105*(B10), 23753–23.

Sueker, J. K., Clow, D. W., Ryan, J. N. & Jarrett, R. D. (2001). Effect of basin physical characteristics on solute fluxes in nine alpine/subalpine basins, Colorado, USA. *Hydrological processes*, *15*(14), 2749–2769.

Sweeney, M. R., Gaylord, D. R., & Busacca, A. J. (2007). Evolution of Eureka Flat: A dust-producing engine of the Palouse loess, USA. *Quaternary International*, *162*, 76-96.

Tonkin, P. J., & Basher, L. R. (1990). Soil-stratigraphic techniques in the study of soil and landform evolution across the Southern Alps, New Zealand. *Geomorphology*, *3*(3), 547-575.

Thorn, C. E. (1979). Bedrock freeze-thaw weathering regime in an alpine environment, Colorado Front Range. *Earth Surface Processes*, *4*(3), 211–228.

Thorn, C. E. & Darmody, R. G. (1985). Grain-size distribution of the insoluble component of contemporary eolian deposits in the alpine zone, Front Range, Colorado, USA. *Arctic and Alpine Research*, *17*(4), 433–442.

Veblen, T. T., & Donnegan, J. A. (2005). *Historical range of variability for forest vegetation of the national forests of the Colorado Front Range*. USDA Forest Service, Rocky Mountain Region.

Welter SP. (1995). Topographic influences on erosion and soil development in hollows of the Rampart Range, Colorado. PhD Dissertation, Department of Geography, University of Colorado, Boulder.

Willett, S. D., Hovius, N., Brandon, M. T., & Fisher, D. M. (2006). *Tectonic, Climate, And Landscape Evolution* (398). Geological Society of America. pages?

Willgoose, G., & Hancock, G. (1998). Revisiting the hypsometric curve as an indicator of form and process in transport-limited catchment. *Earth Surface Processes and Landforms*, *23*(7), 611-623.

Williams, G. P., Rosgen, D. L. (1989). Measured total sediment loads (suspended and bedload) for 93 United States streams: *US Geological Survey, Open-File Report 89–67*.

Wohl, E. (2010). A brief review of the process domain concept and its application to quantifying sediment dynamics in bedrock canyons. *Terra Nova*, *22*(6), 411–416.

Wohl, E. (2008). The effect of bedrock jointing on the formation of straths in the Cache la Poudre River drainage, Colorado Front Range. *Journal of Geophysical Research: Earth Surface (2003–2012)*, *113*(F1).

Yoo, K., Mudd, S. M., Sanderman, J., Amundson, R. & Blum, A. (2009). Spatial patterns and controls of soil chemical weathering rates along a transient hillslope. *Earth and Planetary Science Letters*, *288*(1), 184–193.

Yoo, K., Weinman, B., Mudd, S. M., Hurst, M., Attal, M. & Maher, K. (2011). Evolution of hillslope soils: The geomorphic theater and the geochemical play. *Applied Geochemistry*, *26*, S149–S153.

Appendix A Supplemental CRN Data

This appendix contains additional data used to calculate CRN derived denudation rates as well matlab scripts used to analyze these data. Contents include: Chipping lengths of bedrock samples, measurements of topographic shielding, grain sizes measurements for soil and sediment, CRONUS (Balco et al., 2008) inputs and outputs for peak samples.

Table 12: Chipping Length measurements taken surround the TRx outcrop

long axis(cm)	intermediate axis (cm)
10.5	5
16	9
8.5	2.5
9.5	6.5
6.5	3.5
5	10.5
8.5	3.5
7	6
10.5	8
13	11
13	7
10	4
16	7.5
6.5	5
6.5	2.5
5.5	2
12.5	8
12	9
12	6.5
10.5	10
10.5	7
9.5	11
10	4.5
4.5	3
5	5
7	4
9	4.5
8.5	3.5

12	5.5
6	2.5
Mean: 9.4	***Mean: 6***

Table 13: Trail Ridge topographic shielding measurements (11JLG01TRx)

Trail Ridge Outcrop 11JLG01TRX					
Bearing	**horizon inclination(%)**	**angle (rads)**	**sin(angle)^3.5/2pi())**	**trapezoidal integration**	
180	8	8.0E-02	2.3E-05	1.5E-05	
225	7	7.0E-02	1.4E-05	1.0E-05	
270	6.5	6.5E-02	1.1E-05	3.1E-05	
315	11	1.1E-01	6.9E-05	2.7E-05	
360	0	0.0E+00	0.0E+00	1.7E-06	
045	5	5.0E-02	4.4E-06	2.9E-05	
090	11	1.1E-01	6.9E-05	2.7E-05	**Sum**
135	2.5	2.5E-02	3.9E-07	9.1E-06	***0.00015***

Table 14: Topographic and slope shielding measurements for 11JLGBHFX

Big Horn Flats Boulder 11JLG04BHFx					
Bearing (°)	**Horizon Inclination (%)**	**angle (radians)**	**sin(angle)^3.5/2pi())**	**trapezoidal integration**	
000	5	5.0E-02	4.4E-06	1.5E-05	
045	9	9.0E-02	3.4E-05	1.4E-05	
090	4	4.0E-02	2.0E-06	2.1E-04	
135	20	2.0E-01	5.3E-04	2.9E-04	
180	15	1.5E-01	2.0E-04	8.8E-05	
225	8	8.0E-02	2.3E-05	2.8E-05	
270	10	1.0E-01	4.9E-05	3.9E-05	**Sum**
315	10	1.0E-01	4.9E-05	2.1E-05	***7.0E-04***
Dip Angle (°)	Slope Scaling Factor				
11	***0.000483***				

Table 15: Sample size measurements and masses used for sediment and soil CRN geochemistry. Yellow shading indicates the masses of each fraction and total mass used for CRN geochemistry.

11-JLG-08-BHCa							
Sieve sizes (mm)	***Sieve wt (g)***	***Seive+sample (g)***	***Sample (g)***	***Fraction of total***	***What's left (g)***	***Possible sample wt (g)***	***Sample added***
>4	484.66	1445.70	961.04	0.46	490.40	1061.97	**230.89**
2-4	463.18	874.90	411.72	0.20	230.80	1166.64	**98.92**
1-2	400.15	694.00	293.85	0.14	173.80	1230.91	**70.60**
0.5-1	369.88	636.60	266.72	0.13	165.40	1290.58	**64.08**
.25 -5	345.78	493.60	147.82	0.07	146.50	2062.57	**35.51**
PAN	346.76	383.20	36.44		**Max sample (g)**		
		Total (g)	2081.15			**Total (g)**	**500.00**
11-JLG-07-Bga							
>4	484.68	899.69	415.01	0.38	176.76	461.67	**155.40**
2-4	463.25	702.16	238.91	0.22	89.46	405.88	**89.46**
1-2	400.19	592.55	192.36	0.18	96.51	543.83	**72.03**
0.5-1	369.86	496.65	126.79	0.12	65.63	561.08	**47.48**
.25 -5	337.25	448.12	110.87	0.10	71.15	695.61	**41.52**
PAN	347.52	442.40	94.88		**Max sample (g)**	405.88	
		Total (g)	1083.94			**Total (g)**	**405.88**
11-JLG-02-TRc							
>4	484.75	1216.30	731.55	0.52	373.14	720.83	**238.64**
2-4	463.39	872.50	409.11	0.29	205.15	708.65	**133.46**
1-2	400.22	590.80	190.58	0.13	84.95	629.93	**62.17**
0.5-1	369.41	427.95	58.54	0.04	28.51	688.25	**19.10**
.25 -5	339.39	362.81	23.42	0.02	7.64	461.01	**7.64**
PAN	347.45	371.43	23.98		**Max sample (g)**	461.01	
		Total (g)	1413.20			**Total (g)**	**461.01**
11-JLG-03-BBa							
>4	484.67	662.13	177.46	0.22	97.36	436.93	**87.36**

2-4	463.25	589.76	126.51	0.16	62.28	392.07	**62.28**	
1-2	400.17	568.88	168.71	0.21	93.48	441.28	**83.05**	
0.5-1	369.87	577.75	207.88	0.26	124.99	478.85	**102.34**	
.25 -5	335.80	451.65	115.85	0.15	94.38	648.81	**57.03**	
PAN	347.45	374.82	27.37		**Max sample (g)**	392.07		
		Total (g)	796.41			**Total (g)**	**392.07**	
11-JLG-09-WRa	sieve	seive+sample	sample	percent of total	what's left	what's possible	Maximum Sample	**500g sample**
>4	484.68	1456.30	971.62	0.52	465.99	896.95	465.99	**259.76**
2-4	463.19	731.31	268.12	0.14	140.94	983.09	128.59	**71.68**
1-2	400.17	699.58	299.41	0.16	148.17	925.51	143.60	**80.05**
0.5-1	369.38	593.67	224.29	0.12	120.52	1004.93	107.57	**59.96**
.25 -5	337.27	444.03	106.76	0.06	93.95	1645.80	51.20	**28.54**
PAN	346.68	385.82	39.14		**Max sample (g)**	896.95		
		Total (g)	1870.20			**Total (g)**	896.95	**500.00**
11-JLG-10-CCa							how much to add	for 500g
>4	484.67	987.60	502.93	0.39	277.74	704.82	272.94	**197.03**
2-4	463.21	671.87	208.66	0.16	113.24	692.64	113.24	**81.75**
1-2	400.19	663.26	263.07	0.21	149.60	725.78	142.77	**103.06**
0.5-1	369.35	583.59	214.24	0.17	136.99	816.08	116.27	**83.93**
.25 -5	335.78	423.16	87.38	0.07	69.01	1007.97	47.42	**34.23**
PAN	346.67	363.24	16.57		**Max sample (g)**	692.64		
		Total (g)	1276.28			**Total (g)**		**500.00**
11-JLG-20-GRCa								**for 650 g**
>4	484.65	1719.50	1234.85	0.55	463.49	845.06	463.49	**356.51**
2-4	463.20	904.50	441.30	0.20	233.29	1190.21	165.64	**127.41**
1-2	400.15	743.97	343.82	0.15	176.99	1158.99	129.05	**99.26**
0.5-1	369.88	537.24	167.36	0.07	101.28	1362.49	62.82	**48.32**
.25 -5	337.25	401.36	64.11	0.03	35.23	1237.22	24.06	**18.51**
PAN	346.60	383.48	36.88		**Max sample (g)**	845.06		
		Total (g)	2251.44			**Total (g)**		**650.00**

11-JLG-18-SkG2a								**for 400 g**
>4	484.64	1816.40	1331.76	0.54	389.75	724.38	363.12	**215.22**
2-4	463.23	968.80	505.57	0.20	137.85	674.89	137.85	**81.70**
1-2	400.21	673.55	273.34	0.11	140.03	1268.02	74.53	**44.17**
0.5-1	369.85	577.50	207.65	0.08	120.78	1439.70	56.62	**33.56**
.25 -5	335.93	492.80	156.87	0.06	128.93	2034.34	42.77	**25.35**
PAN	346.40	434.54	88.14		**Max sample (g)**	674.89		
		Total (g)	2475.19			**Total (g)**		**400.00**
11-JLG-14-SGa								**for 400 g**
>4	484.61	1424.00	939.39	0.47	284.96	611.45	284.96	**186.42**
2-4	463.23	730.70	267.47	0.13	117.33	884.21	81.14	**53.08**
1-2	400.16	813.90	413.74	0.21	223.57	1089.21	125.51	**82.10**
0.5-1	369.33	678.42	309.09	0.15	184.55	1203.52	93.76	**61.34**
.25 -5	337.23	423.23	86.00	0.04	61.47	1440.75	26.09	**17.07**
PAN	346.40	434.54	88.14		**Max sample (g)**	611.45		
		Total (g)	2015.69			**Total (g)**		**400.00**
11-JLG-13-JGa								**for 400 g**
>4	484.64	905.20	420.56	0.27	168.85	626.13	168.85	**121.35**
2-4	463.24	788.31	325.07	0.21	140.91	676.02	130.51	**93.80**
1-2	400.21	860.60	460.39	0.30	250.90	849.90	184.84	**132.84**
0.5-1	369.35	630.03	260.68	0.17	147.88	884.70	104.66	**75.22**
.25 -5	337.23	430.06	92.83	0.06	66.66	1119.88	37.27	**26.79**
PAN	347.00	434.54	87.54		**Max sample (g)**	626.13		
		Total (g)	1559.53			**Total (g)**		**450.00**
11-JLG-11-RCa								for 400 g
>4	484.61	1624.50	1139.89	0.58	437.74	756.53	437.74	**260.38**
2-4	463.23	798.93	335.70	0.17	174.62	1024.74	128.92	**76.68**
1-2	400.16	665.91	265.75	0.13	145.23	1076.60	102.05	**60.70**
0.5-1	369.84	533.54	163.70	0.08	97.77	1176.60	62.86	**37.39**
.25 -5	335.81	400.79	64.98	0.03	45.71	1385.81	24.95	**14.84**

PAN	347.00	377.95	30.95		**Max sample (g)**	756.53		
		Total (g)	1970.02			**Total (g)**		**450.00**
11-JLG-05-BHFc								
>4	484.78	733.43	248.65	0.531814779	133.52	251.0648542	**120.31**	
2-4	463.21	617.71	154.5	0.330445942	79.26	239.8576893	**74.68**	
1-2	400.99	454.28	53.29	0.113977115	26.2	229.8707074	**26.2**	
0.5-1	369.88	378.19	8.31	0.0177735	4.41	248.1222022	**4.02**	
.25 -5	335.82	338.62	2.8	0.005988664	1.76	293.8885714	**1.35**	
PAN	347.48	351.51	4.03		**Max sample (g)**	229.8707074		
		Total (g)	467.55			**Total (g)**	**226.56**	

Table 16: Calculation steps taken to convert $^{10}Be/^{9}Be$ ratio reported from AMS measurement into a ^{10}Be concentration. Blanks used have been highlighted in yellow.

Sample #	Sample mass	Mass 9Be spike	[9Be]	10Be/9Be	Err	10Be/9Be - blank	blank subtract Err	Mass 9Be added	Moles 9Be	atoms 9Be	atoms 10/be	[10Be]	error
	(g)	(g)	ppm					g				Atoms/g	
11JLG04BHFx	22.2	0.866	373	1.30E-12	1.50E-14	1.29E-12	1.71E-14	3.23E-04	3.58E-05	2.16E+19	2.78E+07	1.25E+06	1.66E+04
11JLG01TRx	24.1	0.355	998	7.16E-13	1.20E-14	7.04E-13	1.45E-14	3.55E-04	3.93E-05	2.37E+19	1.67E+07	6.93E+05	1.43E+04
11JLGBL01	24.1	0.849	373	8.20E-15	2.20E-15	-1.83E-12	8.49E-15	3.16E-04	3.51E-05	2.11E+19	-3.87E+07	-1.61E+06	-7.45E+03
11JLG05BHFc	12.1	0.869	373	1.84E-12	4.00E-14	1.83E-12	4.08E-14	3.24E-04	3.59E-05	2.16E+19	3.96E+07	3.27E+06	7.30E+04
11JLG02TRe	24.1	0.850	373	7.18E-13	2.20E-14	7.10E-13	2.35E-14	3.16E-04	3.51E-05	2.11E+19	1.50E+07	6.23E+05	2.06E+04
11FDBL01	0	0.347	998	1.18E-14	1.20E-15								
11JLG13	35.2	0.867	373	1.58E-12	4.00E-14	1.57E-12	4.01E-14	3.23E-04	3.58E-05	2.16E+19	3.38E+07	9.60E+05	2.46E+04
12CSRB02	0	0.867	373	1.50E-14	3.00E-15								
11JLG18	17.1	0.863	373	7.20E-13	5.00E-14	7.05E-13	5.01E-14	3.22E-04	3.57E-05	2.15E+19	1.51E+07	8.86E+05	6.30E+04
11JLG14	41.7	0.866	373	1.18E-12	1.90E-14	1.16E-12	1.92E-14	3.23E-04	3.58E-05	2.16E+19	2.51E+07	6.01E+05	9.95E+03
11JLG07	28.2	0.912	373	1.27E-12	9.00E-14	1.26E-12	9.00E-14	3.40E-04	3.77E-05	2.27E+19	2.85E+07	1.01E+06	7.24E+04
11JLG03	24.9	0.862	373	1.54E-12	7.00E-14	1.53E-12	7.01E-14	3.21E-04	3.56E-05	2.14E+19	3.27E+07	1.31E+06	6.04E+04
11JLG09	17.2	0.910	373	6.65E-13	2.70E-14	6.50E-13	2.72E-14	3.39E-04	3.76E-05	2.27E+19	1.47E+07	8.55E+05	3.57E+04

11JLG10	24.9	0.866	373	1.59E-12	6.00E-14	1.58E-12	6.01E-14	3.23E-04	3.58E-05	2.16E+19	3.40E+07	1.37E+06	5.21E+04
11JLG08	41.8	0.849	373	2.29E-12	2.60E-14	2.27E-12	2.62E-14	3.16E-04	3.51E-05	2.11E+19	4.80E+07	1.15E+06	1.32E+04
11JLG20	36.2	0.851	373	8.18E-13	1.40E-14	8.03E-13	1.43E-14	3.17E-04	3.52E-05	2.12E+19	1.70E+07	4.71E+05	8.39E+03
11JLG11	22.5	0.865	373	1.02E-12	5.00E-14	1.01E-12	5.01E-14	3.22E-04	3.58E-05	2.15E+19	2.16E+07	9.63E+05	4.80E+04

Table 17: CRONUS model inputs

name	latitude	longitude	Elev	Elev flag	sample thickness (cm)	sample density (g/cm^3)	shielding	N10Be	10Be err	standard	N26Al	26Al err	Standard
11-JLG-01	40.43117	-105.783	3511	std	5	2.65	0.843	6.85E+05	1.41E+04	07KNSTD	0	0	KNSTD
11-JLG-02	40.59761	-105.783	3510.6	std	5	2.65	0.843	6.16E+05	2.04E+04	07KNSTD	0	0	KNSTD
11-JLG-04	40.32003	-105.703	3734	std	5	2.65	1	1.24E+06	16372.83	07KNSTD	0	0	KNSTD
11-JLG-05	40.32003	-105.703	3734	std	5	2.65	0.81	3.23E+06	7.20E+04	07KNSTD	0	0	KNSTD
11-JLG-042	40.32003	-105.703	3734	std	100	2.65	1	1.24E+06	16372.83	07KNSTD	0	0	KNSTD

CRONUS-Earth ^{10}Be - ^{26}Al erosion rate calculator -- results

Version information --

Component	Version
Wrapper script:	2.2
Main calculator:	2.1
Objective function:	2.0
Constants:	2.2.1

Muons: 1.1

Production rate calibration information: Using default calibration data set

^{10}Be results:

Results not dependent on spallogenic production rate model: / *Erosion rates -- constant production rate model:*

Sample name	Shielding factor	Production rate (muons) (atoms/g/yr)	Internal uncertainty (m/Myr)	Erosion rate (g/cm2/yr)	Erosion rate (m/Myr)	External uncertainty (m/Myr)	Production rate (spallation) (atoms/g/yr)
				Scaling scheme for spallation: Lal(1991) / Stone(2000)			
11-JLG-01	0.8430	0.526	0.83	0.01051	39.66	3.30	43.21
11-JLG-02	0.8430	0.526	1.49	0.01176	44.37	3.87	43.40
11-JLG-04	1.0000	0.559	0.38	0.00756	28.53	2.39	57.75
11-JLG-05	0.8100	0.559	0.20	0.00229	8.65	0.76	46.78
11-JLG-04-2 (100cm thickness)	1.0000	0.450	0.20	0.00395	14.91	1.23	57.75

Erosion rates -- time-varying production models:

Scaling scheme for spallation:	Desilets and others (2003,2006)			Dunai (2001)			Lifton and others (2005)			Time-dependent Lal (1991)/Stone (2000)		
Sample name	Erosion rate (g/cm2/yr)	Erosion rate (m/Myr)	External uncertainty (m/Myr)	Erosion rate (g/cm2/yr)	Erosion rate (m/Myr)	External uncertainty (m/Myr)	Erosion rate (g/cm2/yr)	Erosion rate (m/Myr)	External uncertainty (m/Myr)	Erosion rate (g/cm2/yr)	Erosion rate (m/Myr)	External uncertainty (m/Myr)
11-JLG-01	0.01181	44.58	4.99	0.01193	45.00	5.02	0.01221	46.08	4.36	0.01093	41.24	3.35
11-JLG-02	0.01316	49.65	5.70	0.01327	50.07	5.73	0.01359	51.29	5.02	0.01217	45.94	3.91
11-JLG-04	0.00878	33.14	3.76	0.00890	33.58	3.80	0.00911	34.36	3.27	0.00797	30.08	2.45
11-JLG-05	0.00277	10.44	1.23	0.00282	10.64	1.25	0.00289	10.90	1.08	0.00249	9.41	0.81
11-JLG-042	0.00468	17.64	1.97	0.00475	17.94	2.00	0.00486	18.35	1.72	0.00424	15.99	1.28

Appendix B Supplementary Snow depth data

This appendix contains the data used to calculate SWE for the samples, including graphs that show no correlation between coefficient of variance and number of record years, and tables containing the monthly means for each record year.

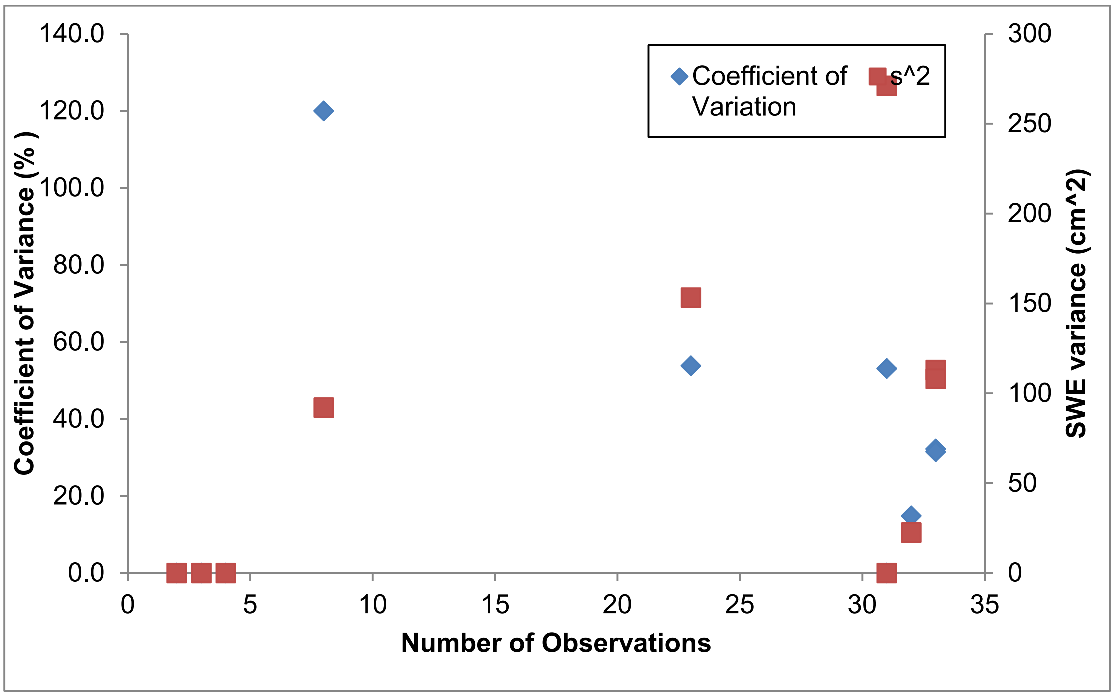

Figure 21: Plot of Coefficient of variation and Variance of the mean SWE's of each station. Plotted against the number of observation years. There is no clear increase in variability with decrease in sample size, implying that it is acceptable to compare these stations with different years of record.

B.1 Snow Data

Below are tables showing the monthly Mean SWE depths for the 10 snotel sites used in this study (NRCS) and standard deviations of each population (s). The bottom right corner of each table contains the mean and standard deviation of the yearly means used in this study.

Tables 18-27: The following tables contain the monthly mean snow depth in SWE from the snotel sites used in this study for each water year reported.

Bear Lake														
year	***oct (in)***	***nov (in)***	***dec (in)***	***jan (in)***	***feb (in)***	***mar (in)***	***apr (in)***	***may (in)***	***jun (in)***	***Jul (in)***	***Aug (in)***	***Sep (in)***	***Yearly Mean (in)***	***Yearly mean (cm)***
1981	0.56	2.66	4.39	5.38	7.72	13.06	17.28	0.78	0.03	0	0	0	4.32	10.98
1982	0.21	1.53	3.78	10.24	12.06	15.39	18.94	15.18	2.01	0	0	0	6.61	16.79
1983	0.06	1.15	3.42	4.8	6.33	10.92	17.22	19.17	7	0	0	0	5.84	14.83
1984	0.06	1.73	8.57	12.76	13.06	15.46	21.22	19.03	0.37	0	0	0	7.69	19.53
1985	0.76	2.76	4.82	6.22	8.07	10.87	15.08	8.65	0	0	0	0.05	4.77	12.12
1986	1.39	3.8	11.07	11.93	16.92	25.27	31.07	23.75	4.54	0	0	0.04	10.82	27.47
1987	0.45	3.51	5.15	6.32	8.2	10.33	11.53	3.18	0	0	0	0	4.06	10.30
1988	0	0.98	3.37	7.72	10.7	13.84	18.1	12.75	0.04	0	0	0	5.63	14.29
1989	0	1.11	3.85	6.73	10.43	14.1	16.11	9.52	0	0	0	0	5.15	13.09
1990	0.16	1.25	3.65	6.02	8.55	14.21	18.89	17.96	1.31	0	0	0	6.00	15.24
1991	0.42	1.1	2.61	4.95	7.87	10.97	13.84	10.73	0.06	0	0	0	4.38	11.12
1992	0.03	2.98	6.15	6.81	7.84	11.59	14.28	3.98	0	0	0	0	4.47	11.36
1993	0.01	2.18	4.93	7.85	12.17	18.28	23.88	19.16	0.82	0	0	0	7.44	18.90
1994	0.6	2.8	5.16	7.47	10.44	14.87	18.46	11.25	0	0	0	0	5.92	15.04
1995	0.35	1.56	4.08	6.56	9.78	13.74	18.44	24.24	11.78	0	0	0.02	7.55	19.17
1996	0.28	2.96	7.28	10.78	18.22	24.27	28.29	20.1	1.17	0	0	0.05	9.45	24.00
1997	0.11	2.65	8	14.47	18.76	21.38	25.76	24.7	2.95	0	0	0	9.90	25.14
1998	0.35	3.13	4.73	6.68	9.29	13.33	17.98	13.96	0.08	0	0	0	5.79	14.72
1999	0.09	1.86	3.74	9.43	13.01	15.04	18.95	22.91	4.19	0	0	0.11	7.44	18.91
2000	0	0.38	2.97	6.73	11.27	16.33	21.02	11.72	0	0	0	0.1	5.88	14.93
2001	0	1.67	3.94	5.73	7.48	9.79	13.17	8.19	0	0	0	0.07	4.17	10.59
2002	0.12	0.21	2.14	4.14	5.89	8.69	9.04	3.61	0	0	0	0	2.82	7.16
2003	0.24	3.37	4.85	6.7	9.73	17.72	23.49	20.3	1.05	0	0	0	7.29	18.51
2004	0	2.35	5.33	8.18	10.01	12.23	16.73	10.75	0.02	0	0	0	5.47	13.89
2005	0.03	1.35	4.32	7.28	10.14	13.26	15.36	14.53	0.56	0	0	0	5.57	14.15

2006	0.22	1.55	6.26	10.55	13.71	15.64	16.53	9.81	0	0	0	0.03	6.19	15.73
2007	1.14	4.49	7.51	12.65	15.22	19.18	21.33	13.11	0.1	0	0	0	7.89	20.05
2008	0	0.22	2.87	7.02	12.22	14.43	17.84	16.77	1.64	0	0	0	6.08	15.45
2009	0.1	0.77	2.92	7.87	12.85	15.38	21.87	20.09	1.27	0	0	0	6.93	17.59
2010	0.6	1.75	4.14	6.6	8.67	11.53	13.25	14.46	1.33	0	0	0	5.19	13.19
2011	0.28	1.69	5.93	11.33	15.07	18.68	23.82	27.66	11.38	0	0	0	9.65	24.52
2012	0.29	2.56	4.57	6.73	10.6	14.04	12.02	2.5	0	0	0	0	4.44	11.28
mean	0.28	2.00	4.89	7.96	11.01	14.81	18.46	14.20	1.68	0.00	0.00	0.01	**6.28**	**15.94**
s	0.33	1.06	1.93	2.58	3.27	3.89	4.87	7.11	3.06	0.00	0.00	0.03	**1.87**	**4.74**

Black Mountain

year	***oct (in)***	***nov (in)***	***dec (in)***	***jan (in)***	***feb (in)***	***mar (in)***	***apr (in)***	***may (in)***	***jun (in)***	***Jul (in)***	***Aug (in)***	***Sep (in)***	***Yearly Mean (in)***	***Yearly Mean (cm)***
2011	0.00	1.33	3.95	5.55	7.68	9.51	11.36	10.02	0.21	0.00	0.00	0.00	4.13	10.50
2012	0.42	2.91	4.94	5.99	8.55	9.91	5.76	0.00	0.00	0.00	0.00	0.00	3.21	8.14
mean	0.21	2.12	4.45	5.77	8.12	9.71	8.56	5.01	0.11	0.00	0.00	0.00	**3.67**	**9.32**
s	0.30	1.12	0.70	0.31	0.62	0.28	3.96	7.09	0.15	0.00	0.00	0.00	**0.66**	**1.67**

Copeland Lake

year	***oct (in)***	***nov (in)***	***dec (in)***	***jan (in)***	***feb (in)***	***mar (in)***	***apr (in)***	***may (in)***	***jun (in)***	***Jul (in)***	***Aug (in)***	***Sep (in)***	***Yearly Mean (in)***	***Yearly Mean (cm)***
1981	0.01	0.14	0.11	0.66	1.14	0.65	0.01	0.00	0.00	0.00	0.00	0.00	0.23	0.58
1982	0.02	0.03	0.36	2.64	2.99	1.17	0.00	0.00	0.00	0.00	0.00	0.00	0.60	1.53
1983	0.04	0.74	4.33	6.17	5.99	5.95	5.03	0.87	0.00	0.00	0.00	0.00	2.43	6.16
1984	0.36	0.39	0.95	1.58	2.38	1.58	0.23	0.00	0.00	0.01	0.00	0.00	0.62	1.58
1985	0.00	1.54	4.18	4.58	5.68	4.72	0.78	0.08	0.00	0.00	0.00	0.06	1.80	4.58
1986	0.01	1.19	0.71	1.68	3.01	2.20	0.59	0.00	0.00	0.00	0.00	0.00	0.78	1.99
1987	0.00	0.33	1.57	3.82	5.01	5.70	1.29	0.00	0.00	0.00	0.00	0.00	1.48	3.75

1988	0.00	0.22	1.42	2.36	4.22	2.11	0.45	0.00	0.00	0.00	0.00	0.00	0.90	2.28
1989	0.00	0.09	0.95	1.58	2.50	3.87	0.74	0.00	0.00	0.00	0.00	0.00	0.81	2.06
1990	0.02	0.37	0.71	1.57	2.36	1.73	0.23	0.01	0.00	0.00	0.00	0.00	0.58	1.48
1991	0.00	0.72	1.65	1.92	2.11	1.91	0.14	0.00	0.00	0.00	0.00	0.00	0.70	1.79
1992	0.00	0.68	2.03	3.19	4.45	4.90	1.67	0.00	0.00	0.00	0.00	0.00	1.41	3.58
1993	0.13	1.17	2.14	3.44	5.44	2.93	0.27	0.02	0.00	0.00	0.00	0.00	1.30	3.29
1994	0.01	0.00	0.00	0.69	1.82	1.19	1.41	1.34	0.06	0.00	0.00	0.00	0.54	1.38
1995	0.00	0.91	2.29	4.24	8.27	8.93	2.11	0.00	0.00	0.00	0.00	0.04	2.23	5.67
1996	0.02	0.24	2.19	4.94	6.85	5.25	0.74	0.40	0.00	0.00	0.00	0.00	1.72	4.37
1997	0.08	0.37	1.03	2.04	2.65	3.00	0.15	0.00	0.00	0.00	0.00	0.00	0.78	1.97
1998	0.00	0.10	0.16	2.10	3.85	2.30	0.97	0.85	0.00	0.00	0.00	0.02	0.86	2.19
1999	0.02	0.23	1.04	2.42	4.74	4.73	0.64	0.00	0.00	0.00	0.00	0.02	1.15	2.93
2000	0.01	0.02	0.48	1.22	2.08	2.48	0.61	0.23	0.00	0.00	0.00	0.03	0.60	1.52
2001	0.00	0.49	1.54	2.41	3.21	3.75	0.06	0.00	0.00	0.00	0.00	0.00	0.96	2.43
2002	0.02	1.65	1.87	2.39	3.46	6.13	3.05	0.10	0.00	0.00	0.00	0.00	1.56	3.95
2003	0.00	0.69	1.77	2.69	3.31	1.56	0.28	0.00	0.00	0.00	0.00	0.00	0.86	2.18
2004	0.00	0.26	2.18	3.51	5.64	5.85	1.28	0.35	0.00	0.00	0.00	0.00	1.59	4.04
2005	0.03	0.27	1.90	3.91	5.52	4.25	0.49	0.00	0.00	0.00	0.00	0.00	1.36	3.46
2006	0.63	0.40	1.69	5.35	6.87	5.12	0.59	0.00	0.00	0.00	0.00	0.00	1.72	4.37
2007	0.01	0.14	1.82	3.75	5.77	5.95	3.51	0.01	0.00	0.00	0.00	0.00	1.75	4.44
2008	0.00	0.01	1.30	3.41	5.52	2.42	0.51	0.00	0.00	0.00	0.00	0.00	1.10	2.79
2009	0.13	0.30	1.49	2.89	3.72	4.42	1.79	0.34	0.00	0.00	0.00	0.00	1.26	3.19
2010	0.00	0.20	1.79	4.51	6.24	6.51	0.70	0.16	0.00	0.00	0.00	0.00	1.68	4.26
2011	0.16	0.61	2.18	3.80	6.18	3.65	0.03	0.00	0.00	0.00	0.00	0.00	1.38	3.52
mean	0.06	0.47	1.54	2.95	4.29	3.77	0.98	0.15	0.00	0.00	0.00	0.01	***1.18***	***3.01***
s	0.13	0.44	0.99	1.36	1.79	1.98	1.13	0.32	0.01	0.00	0.00	0.01	***0.53***	***1.35***

Dead Mans

year	***oct (in)***	***nov (in)***	***dec (in)***	***jan (in)***	***feb (in)***	***mar (in)***	***apr (in)***	***may (in)***	***jun (in)***	***Jul (in)***	***Aug (in)***	***Sep (in)***	***Yearly Mean (in)***	***Yearly Mean (cm)***

1979	0.46	2.24	6.07	10.38	12.75	15.55	20.16	19.19	4.27	0.00	0.00	0.00	7.59	19.28
1980	0.25	2.74	5.53	8.87	13.78	16.93	20.64	21.17	3.98	0.00	0.00	0.00	7.82	19.87
1981	1.18	3.65	5.55	6.07	7.90	10.87	13.06	9.78	1.11	0.00	0.00	0.00	4.93	12.52
1982	0.74	3.15	5.96	11.26	14.33	16.56	19.12	21.42	12.39	0.00	0.00	0.00	8.74	22.21
1983	1.65	4.05	7.47	10.29	11.50	17.08	22.77	25.51	19.05	0.10	0.00	0.00	9.96	25.29
1984	0.95	3.84	9.86	13.47	14.82	17.00	21.18	20.78	3.64	0.00	0.00	0.00	8.80	22.34
1985	1.40	4.24	7.66	9.96	11.70	13.49	16.47	12.53	0.45	0.00	0.00	0.12	6.50	16.51
1986	3.83	8.88	14.16	14.29	17.20	21.47	27.14	24.22	6.35	0.00	0.00	0.18	11.48	29.15
1987	1.44	5.22	7.03	7.80	9.00	10.64	12.25	4.44	0.00	0.00	0.00	0.00	4.82	12.24
1988	0.33	2.46	4.47	8.24	11.78	14.64	19.78	19.86	2.39	0.00	0.00	0.00	7.00	17.77
1989	0.00	1.95	4.79	7.56	10.77	13.59	17.60	11.38	0.34	0.00	0.00	0.00	5.67	14.39
1990	0.08	1.37	3.96	5.94	8.65	13.16	16.54	16.70	0.95	0.00	0.00	0.00	5.61	14.26
1991	2.00	4.20	5.78	7.87	9.72	12.98	16.40	14.46	0.68	0.00	0.00	0.00	6.17	15.68
1992	0.08	2.47	4.74	6.92	8.23	12.48	15.87	8.55	0.06	0.00	0.00	0.00	4.95	12.57
1993	0.05	2.28	4.31	6.97	11.03	14.69	19.60	19.54	3.96	0.00	0.00	0.00	6.87	17.45
1994	1.48	4.86	7.96	10.28	13.00	15.98	18.59	12.99	0.00	0.00	0.00	0.00	7.10	18.02
1995	0.69	2.23	3.53	4.93	7.70	10.23	13.57	23.35	18.09	0.33	0.00	0.27	7.08	17.97
1996	2.60	7.57	10.94	13.91	17.72	21.16	24.35	20.93	2.83	0.00	0.00	0.26	10.19	25.88
1997	0.79	3.58	6.85	10.28	12.96	15.02	18.92	19.38	2.47	0.00	0.00	0.01	7.52	19.11
1998	1.02	4.46	6.81	8.54	10.38	12.64	15.94	14.20	0.33	0.00	0.00	0.00	6.19	15.73

1999	1.35	4.60	6.23	10.59	13.93	15.47	17.67	19.74	3.14	0.00	0.00	0.05	7.73	19.64
2000	0.08	0.33	2.25	4.87	7.94	11.44	16.02	16.29	0.51	0.00	0.00	0.29	5.00	12.70
2001	0.16	2.52	5.60	7.54	9.36	11.13	14.90	11.46	0.27	0.00	0.00	0.02	5.25	13.33
2002	0.36	1.20	2.95	4.26	6.05	8.92	10.36	6.95	0.00	0.00	0.00	0.00	3.42	8.69
2003	0.03	1.89	2.96	4.17	5.46	10.25	16.18	18.33	2.49	0.00	0.00	0.00	5.15	13.07
2004	0.00	2.18	4.07	6.22	7.61	9.96	13.84	10.86	0.34	0.00	0.00	0.11	4.60	11.68
2005	2.12	4.34	7.35	9.81	11.61	13.77	16.13	15.51	3.39	0.00	0.00	0.00	7.00	17.79
2006	0.79	3.42	7.03	9.75	12.15	14.78	16.40	12.11	0.04	0.00	0.00	0.31	6.40	16.25
2007	0.67	3.19	6.17	10.01	11.95	14.15	14.49	11.66	0.00	0.00	0.00	0.00	6.02	15.30
2008	1.87	3.91	6.35	9.24	12.71	15.60	19.69	20.56	5.99	0.00	0.00	0.00	7.99	20.30
2009	1.00	2.54	5.09	8.69	11.87	14.12	19.36	17.52	1.23	0.00	0.00	0.00	6.79	17.23
2010	1.25	2.99	4.59	6.37	8.15	11.17	17.02	21.86	3.66	0.00	0.00	0.00	6.42	16.31
2011	1.35	3.57	6.36	10.65	15.38	19.62	25.38	31.28	14.99	0.00	0.00	0.00	10.72	27.22
mean	0.97	3.40	6.07	8.67	11.18	14.14	17.80	16.80	3.62	0.01	0.00	0.05	**6.89**	**17.51**
s	0.87	1.68	2.36	2.60	3.00	3.09	3.71	5.84	5.13	0.06	0.00	0.10	**1.86**	**4.73**

Hour Glass Lake

year	***oct (in)***	***nov (in)***	***dec (in)***	***jan (in)***	***feb (in)***	***mar (in)***	***apr (in)***	***may (in)***	***jun (in)***	***Jul (in)***	***Aug (in)***	***Sep (in)***	***Yearly Mean (in)***	***Yearly Mean (cm)***
2009	0.00	0.15	1.54	3.65	5.21	6.35	9.63	2.96	0.00	0.00	0.00	0.00	2.46	6.24
2010	0.64	2.52	3.94	5.19	5.89	7.48	8.98	6.68	0.00	0.00	0.00	0.00	3.44	8.75
2011	0.23	1.53	3.99	5.97	8.29	10.32	13.07	12.95	0.79	0.00	0.00	0.00	4.76	12.09

2012	0.40	3.09	5.12	6.69	9.16	10.33	7.28	0.06	0.00	0.00	0.00	0.00	3.51	8.92
mean	0.32	1.82	3.65	5.38	7.14	8.62	9.74	5.66	0.20	0.00	0.00	0.00	**3.54**	**9.00**
s	0.27	1.29	1.51	1.30	1.89	2.02	2.43	5.56	0.40	0.00	0.00	0.00	**0.94**	**2.40**

Joe Wright

year	*oct (in)*	*nov (in)*	*dec (in)*	*jan (in)*	*feb (in)*	*mar (in)*	*apr (in)*	*may (in)*	*jun (in)*	*Jul (in)*	*Aug (in)*	*Sep (in)*	*Yearly Mean (in)*	*Yearly Mean (cm)*
1979	0.25	1.60	7.65	16.18	22.73	26.35	0.00	0.00	0.00	0.00	0.00	0.00	6.23	15.82
1980	0.08	3.56	6.95	11.52	16.26	21.75	26.17	26.34	6.63	0.00	0.00	0.00	9.94	25.24
1981	1.02	3.64	5.46	6.27	8.20	12.22	14.95	11.86	0.86	0.00	0.00	0.00	5.37	13.65
1982	1.18	5.14	8.18	14.62	16.94	19.91	22.88	24.76	14.52	0.01	0.00	0.00	10.68	27.12
1983	2.25	6.94	10.76	13.20	15.75	22.31	30.12	36.29	29.03	2.07	0.00	0.00	14.06	35.71
1984	1.41	6.36	12.79	18.64	21.47	24.53	30.26	31.79	11.47	0.00	0.00	0.00	13.23	33.60
1985	1.50	5.45	9.13	11.19	14.34	16.91	21.36	19.63	3.08	0.00	0.00	0.18	8.56	21.75
1986	2.76	8.11	14.72	15.76	19.54	25.74	34.30	29.72	10.42	0.00	0.00	0.22	13.44	34.14
1987	3.72	7.93	10.17	12.11	14.18	16.85	17.94	10.54	0.16	0.00	0.00	0.00	7.80	19.81
1988	0.19	3.45	6.24	10.91	15.95	21.25	25.20	23.41	5.30	0.00	0.00	0.00	9.33	23.69
1989	0.00	2.58	6.04	9.64	13.30	16.22	19.02	13.45	0.09	0.00	0.00	0.00	6.70	17.01
1990	0.74	3.93	8.58	11.90	14.19	21.00	26.94	28.30	7.61	0.00	0.00	0.00	10.27	26.08
1991	1.45	3.48	5.49	9.10	11.85	17.06	21.37	21.89	4.29	0.00	0.00	0.00	8.00	20.32
1992	0.11	3.72	6.49	9.09	11.58	16.24	20.01	13.13	2.06	0.00	0.00	0.00	6.87	17.45
1993	0.02	5.11	8.00	11.41	15.92	20.56	28.95	28.33	11.83	0.03	0.00	0.01	10.85	27.55
1994	1.49	5.61	8.92	12.31	15.38	18.87	20.46	12.83	0.06	0.00	0.00	0.00	7.99	20.31
1995	0.53	2.48	4.76	6.62	10.29	13.04	17.42	29.90	23.96	1.97	0.00	0.12	9.26	23.51
1996	1.54	6.43	9.99	15.12	21.36	26.33	31.08	29.02	8.28	0.00	0.00	0.19	12.45	31.61
1997	0.65	4.75	9.82	15.99	19.76	22.11	28.99	29.39	8.73	0.00	0.00	0.00	11.68	29.67
1998	0.90	4.46	7.43	10.90	14.12	17.94	22.09	19.19	4.69	0.00	0.00	0.00	8.48	21.53
1999	1.00	4.11	6.57	11.01	15.85	18.97	21.52	22.25	7.10	0.00	0.00	0.00	9.03	22.94
2000	0.23	2.09	5.18	9.38	14.14	19.76	23.59	18.51	0.87	0.00	0.00	0.06	7.82	19.86
2001	0.09	3.77	7.49	10.34	12.79	15.67	19.78	14.49	0.10	0.00	0.00	0.04	7.05	17.90

mean	1.00	4.55	8.12	11.88	15.47	19.63	22.80	21.52	7.01	0.18	0.00	0.04	**9.35**	**23.75**
s	0.95	1.76	2.47	3.07	3.63	3.92	7.06	8.70	7.57	0.58	0.00	0.07	**2.41**	**6.13**

Long Draw Reservoir

year	*oct (in)*	*nov (in)*	*dec (in)*	*jan (in)*	*feb (in)*	*mar (in)*	*apr (in)*	*may (in)*	*jun (in)*	*Jul (in)*	*Aug (in)*	*Sep (in)*	*Yearly Mean (in)*	*Yearly Mean (cm)*
2010	1.02	3.01	4.73	6.85	8.54	10.77	13.59	15.52	2.03	0.00	0.00	0.00	5.51	13.98
2011	0.46	3.54	7.80	10.96	15.33	19.73	25.70	28.67	14.12	0.00	0.00	0.00	10.53	26.74
2012	0.58	2.86	4.12	5.70	8.22	10.66	7.82	0.34	0.00	0.00	0.00	0.00	3.36	8.53
mean	0.69	3.14	5.55	7.84	10.70	13.72	15.70	14.84	5.38	0.00	0.00	0.00	**6.46**	**16.42**
s	0.29	0.36	1.97	2.77	4.02	5.21	9.13	14.18	7.63	0.00	0.00	0.00	**3.68**	**9.34**

Wild Basin

year	*oct (in)*	*nov (in)*	*dec (in)*	*jan (in)*	*feb (in)*	*mar (in)*	*apr (in)*	*may (in)*	*jun (in)*	*Jul (in)*	*Aug (in)*	*Sep (in)*	*Yearly Mean (in)*	*Yearly Mean (cm)*
2004	0.00	3.17	6.55	12.13	9.76	14.99	22.83	12.11	3.46	1.09	0.89	0.00	7.25	18.41
2005	0.34	1.23	5.33	8.50	10.77	13.58	14.39	4.75	0.00	0.00	0.00	0.00	4.91	12.47
2006	0.95	3.50	5.77	9.76	11.73	14.60	17.22	5.91	0.00	0.00	0.00	0.00	5.79	14.70
2007	0.48	0.93	3.25	6.30	10.29	12.46	15.49	8.78	0.00	0.00	0.00	0.00	4.83	12.27
2008	0.06	0.48	2.69	6.62	10.20	12.11	15.79	7.06	0.00	0.00	0.00	0.00	4.58	11.64
2009	0.75	2.44	4.60	6.65	7.99	10.45	13.36	11.28	0.00	0.00	0.00	0.00	4.79	12.18
2010	0.38	2.20	6.10	10.50	13.68	17.79	22.11	23.58	4.08	0.00	0.00	0.00	8.37	21.26
2011	0.36	2.88	5.10	7.24	10.87	13.63	12.34	0.92	0.00	0.00	0.00	0.00	4.45	11.29
mean	0.42	2.10	4.92	8.46	10.66	13.70	16.69	9.30	0.94	0.14	0.11	0.00	**5.62**	**14.28**
s	0.32	1.11	1.35	2.14	1.63	2.20	3.87	6.80	1.75	0.39	0.31	0.00	**1.44**	**3.66**

Willow Park

year	*oct (in)*	*nov (in)*	*dec (in)*	*jan (in)*	*feb (in)*	*mar (in)*	*apr (in)*	*may (in)*	*jun (in)*	*Jul (in)*	*Aug (in)*	*Sep (in)*	*Yearly Mean (in)*	*Yearly Mean (cm)*

1981	0.79	2.58	3.11	3.31	4.40	6.72	9.26	0.17	0.00	0.00	0.00	0.00	2.53	6.42
1982	0.52	2.20	4.06	10.04	13.12	15.71	20.12	18.99	3.44	0.00	0.00	0.00	7.35	18.67
1983	0.25	2.14	4.69	8.06	10.04	15.10	21.98	28.62	14.56	0.00	0.00	0.00	8.79	22.32
1984	0.44	2.27	11.23	16.03	16.57	18.91	24.83	21.64	0.77	0.00	0.00	0.00	9.39	23.85
1985	0.84	3.57	6.73	9.20	11.19	13.90	19.37	12.19	0.02	0.00	0.00	0.03	6.42	16.31
1986	1.52	4.12	11.19	12.39	16.70	24.02	29.96	22.93	1.48	0.00	0.00	0.08	10.37	26.33
1987	1.24	5.06	7.50	9.29	11.05	12.17	12.24	2.39	0.00	0.00	0.00	0.00	5.08	12.90
1988	0.08	2.56	6.46	12.41	16.23	20.60	24.45	18.26	0.86	0.00	0.00	0.00	8.49	21.57
1989	0.00	1.24	4.52	7.32	11.20	14.74	17.58	7.68	0.00	0.00	0.00	0.01	5.36	13.61
1990	0.16	1.76	5.17	7.70	10.70	15.16	18.67	16.33	0.28	0.00	0.00	0.00	6.33	16.07
1991	0.45	1.61	3.84	6.04	7.31	10.69	13.95	10.08	0.00	0.10	0.00	0.01	4.51	11.45
1992	0.17	4.03	7.41	8.36	9.49	13.20	15.21	3.32	0.00	0.00	0.00	0.00	5.10	12.95
1993	0.04	2.91	5.35	8.52	12.52	17.49	23.52	18.15	0.63	0.00	0.00	0.03	7.43	18.87
1994	0.69	2.89	5.27	7.48	10.33	13.78	17.46	8.06	0.00	0.00	0.00	0.00	5.50	13.96
1995	0.29	3.13	4.79	6.65	8.99	10.71	13.49	23.44	13.85	0.00	0.00	0.04	7.12	18.07
1996	0.39	3.83	8.48	12.17	16.87	21.30	23.67	14.95	0.25	0.00	0.00	0.08	8.50	21.59
1997	0.37	3.24	9.10	15.95	20.00	21.32	26.10	26.55	1.97	0.00	0.00	0.00	10.38	26.37
1998	0.45	3.12	5.53	8.52	11.55	14.86	19.36	13.14	0.07	0.00	0.00	0.00	6.38	16.21
1999	0.24	2.39	4.41	7.97	11.99	14.03	18.03	26.44	5.38	0.00	0.00	0.00	7.57	19.24
2000	0.06	0.72	4.04	8.35	12.50	17.73	20.62	7.22	0.00	0.00	0.00	0.04	5.94	15.09
2001	0.02	2.27	5.47	7.67	10.12	12.43	17.31	9.26	0.00	0.00	0.00	0.01	5.38	13.67
2002	0.22	0.79	3.90	5.75	7.69	10.78	8.80	1.31	0.00	0.00	0.00	0.00	3.27	8.31
2003	0.36	3.25	4.74	6.58	9.60	14.85	19.00	16.45	0.14	0.00	0.00	0.00	6.25	15.87
2004	0.00	2.36	4.62	7.25	9.69	10.84	13.53	4.36	0.00	0.00	0.00	0.05	4.39	11.15
2005	0.14	2.81	5.09	8.14	9.99	12.25	14.07	11.32	0.31	0.00	0.00	0.00	5.34	13.57
2006	0.09	2.16	6.25	9.76	12.08	14.24	15.31	6.32	0.00	0.00	0.00	0.04	5.52	14.02
2007	1.11	3.40	6.14	10.49	11.94	14.83	16.72	10.69	0.22	0.00	0.00	0.00	6.30	15.99
2008	0.55	0.99	4.54	8.25	13.18	15.64	19.23	15.78	1.14	0.00	0.00	0.00	6.61	16.79
2009	0.25	2.12	5.95	9.98	12.82	15.07	19.89	14.05	0.31	0.00	0.00	0.03	6.71	17.03
2010	1.15	3.43	6.31	9.47	10.94	13.15	15.16	16.96	1.00	0.00	0.00	0.00	6.46	16.42

2011	0.49	3.42	8.52	13.39	18.69	23.18	31.09	38.00	17.39	0.00	0.00	0.00	12.85	32.63
2012	0.39	2.66	5.22	6.86	9.29	10.70	6.00	0.03	0.00	0.00	0.00	0.00	3.43	8.71
mean	0.43	2.66	5.93	9.04	11.84	15.00	18.31	13.91	2.00	0.00	0.00	0.01	**6.59**	**16.75**
s	0.39	0.99	2.00	2.78	3.35	3.94	5.68	9.06	4.51	0.02	0.00	0.02	**2.19**	**5.57**

Lake Irene

year	*oct (in)*	*nov (in)*	*dec (in)*	*jan (in)*	*feb (in)*	*mar (in)*	*apr (in)*	*may (in)*	*jun (in)*	*Jul (in)*	*Aug (in)*	*Sep (in)*	*Yearly Mean (in)*	*Yearly Mean (cm)*
1980	0.03	2.62	7.71	16.07	24.24	31.13	35.92	37.05	10.69	0.00	0.00	0.00	13.79	35.02
1981	0.76	2.14	3.74	5.20	8.13	10.88	13.07	5.39	0.06	0.00	0.00	0.00	4.11	10.45
1982	0.63	3.21	8.44	17.75	23.35	28.85	34.40	33.75	16.45	0.01	0.00	0.00	13.90	35.31
1983	1.03	3.57	8.05	12.56	15.63	23.49	31.16	36.62	24.86	0.28	0.00	0.00	13.10	33.28
1984	1.06	3.00	12.40	19.73	22.85	26.52	31.53	32.12	10.72	0.00	0.00	0.00	13.33	33.85
1985	1.15	5.04	9.53	14.39	17.68	22.04	27.47	21.17	2.31	0.00	0.00	0.17	10.08	25.60
1986	2.71	7.41	16.39	19.47	25.34	33.28	39.51	33.65	8.51	0.00	0.00	0.23	15.54	39.48
1987	2.07	5.61	9.48	11.16	14.64	16.75	18.28	6.93	0.00	0.00	0.00	0.00	7.08	17.97
1988	0.17	2.93	6.51	13.65	20.49	26.76	30.29	24.45	2.00	0.00	0.00	0.00	10.60	26.93
1989	0.00	3.15	7.42	13.16	17.90	22.10	25.54	15.03	0.00	0.00	0.00	0.00	8.69	22.08
1990	0.10	1.18	4.86	9.47	13.88	19.53	23.96	23.10	3.03	0.00	0.00	0.00	8.26	20.98
1991	0.64	2.30	4.28	7.77	10.51	15.29	18.69	17.20	2.43	0.00	0.00	0.00	6.59	16.74
1992	0.26	4.16	8.04	10.45	13.37	18.33	22.14	9.48	0.13	0.00	0.01	0.00	7.20	18.28
1993	0.09	3.70	7.41	13.19	19.30	25.85	32.58	29.92	10.52	0.00	0.00	0.04	11.88	30.18
1994	1.61	4.25	7.68	12.81	17.04	21.97	24.43	15.81	0.01	0.00	0.00	0.02	8.80	22.36
1995	0.66	2.70	5.56	8.99	15.28	19.94	23.38	31.85	21.82	0.70	0.00	0.02	10.91	27.71
1996	0.69	5.23	11.57	16.89	24.35	30.82	35.51	27.01	3.53	0.00	0.00	0.06	12.97	32.95
1997	0.54	4.04	10.54	18.87	24.10	27.26	31.57	29.08	7.84	0.00	0.00	0.00	12.82	32.56
1998	0.30	2.94	6.11	9.95	15.03	19.50	22.32	16.85	0.72	0.00	0.00	0.00	7.81	19.84
1999	0.51	2.99	5.14	13.13	19.89	22.84	23.64	22.24	4.31	0.00	0.00	0.00	9.56	24.28
2000	0.08	0.72	4.26	9.34	16.58	22.31	23.31	12.75	0.00	0.00	0.00	0.07	7.45	18.93

2001	0.13	2.47	7.81	11.71	15.30	19.02	22.40	11.75	0.00	0.00	0.00	0.06	7.55	19.19
2002	0.62	1.22	5.09	8.35	11.66	15.70	14.17	4.15	0.00	0.00	0.00	0.00	5.08	12.90
2003	0.44	4.65	7.71	11.19	15.73	23.10	27.23	24.62	2.32	0.00	0.00	0.00	9.75	24.76
2004	0.00	2.48	5.79	9.38	11.86	14.41	16.41	5.53	0.00	0.00	0.00	0.00	5.49	13.94
2005	0.22	2.43	6.80	11.99	14.76	17.82	19.42	16.39	2.13	0.00	0.00	0.00	7.66	19.46
2006	0.14	3.44	9.82	15.47	19.62	22.45	24.00	12.54	0.00	0.00	0.00	0.11	8.97	22.77
2007	1.05	4.41	8.57	13.77	17.06	21.37	23.37	14.45	0.49	0.00	0.00	0.00	8.71	22.13
2008	0.77	1.86	5.86	11.59	18.19	21.80	26.11	22.42	3.65	0.00	0.00	0.00	9.35	23.76
2009	0.17	1.86	7.02	14.16	19.17	22.96	27.64	21.04	0.88	0.00	0.00	0.08	9.58	24.34
2010	1.04	3.54	6.43	10.24	13.00	16.40	19.17	21.13	2.26	0.00	0.00	0.00	7.77	19.73
2011	0.87	5.84	12.69	18.65	24.50	30.66	38.55	43.21	23.40	0.14	0.00	0.00	16.54	42.02
Mean	0.64	3.35	7.77	12.83	17.51	22.22	25.85	21.21	5.16	0.04	0.00	0.03	**9.72**	**24.68**
s	0.62	1.46	2.77	3.64	4.50	5.33	6.81	10.24	7.23	0.13	0.00	0.05	**3.05**	**7.73**

Appendix C Additional regolith data visualization and scripts

This appendix contains graphs of relevant soil data visually showing normality for the statistical tests presented in this thesis.

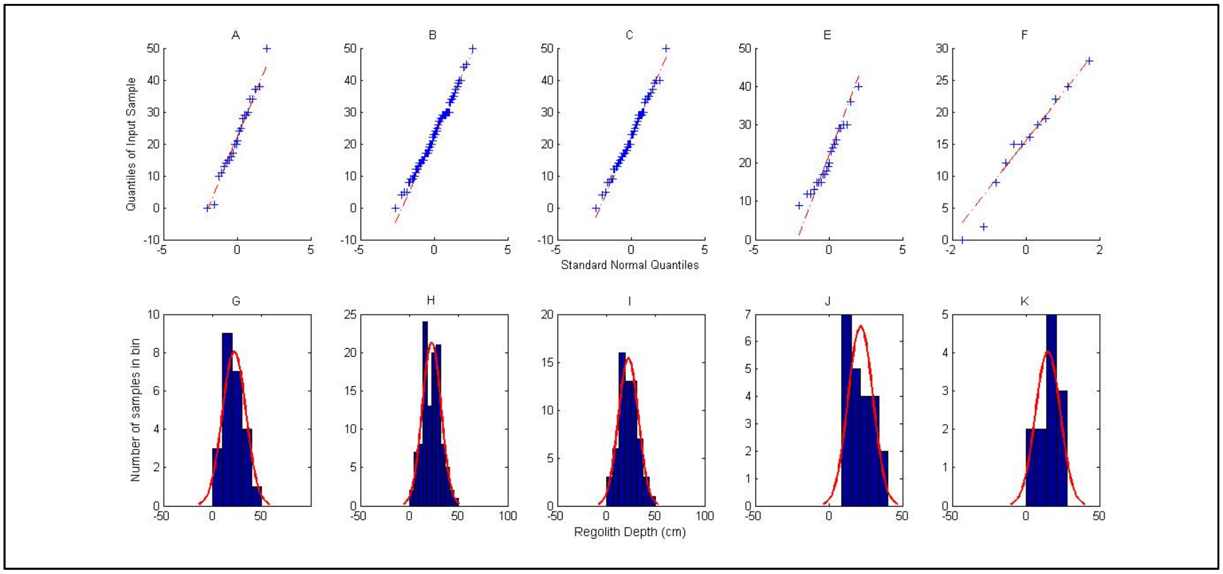

Figure 22: QQ plots and histograms of lower basin regolith depth data separated into populations based on aspect. A and G correspond to North aspects, B and H correspond to east aspects, C and I correspond to South sspects, E and J correspond to West aspects, and F and K correspond to flat sampling locations.

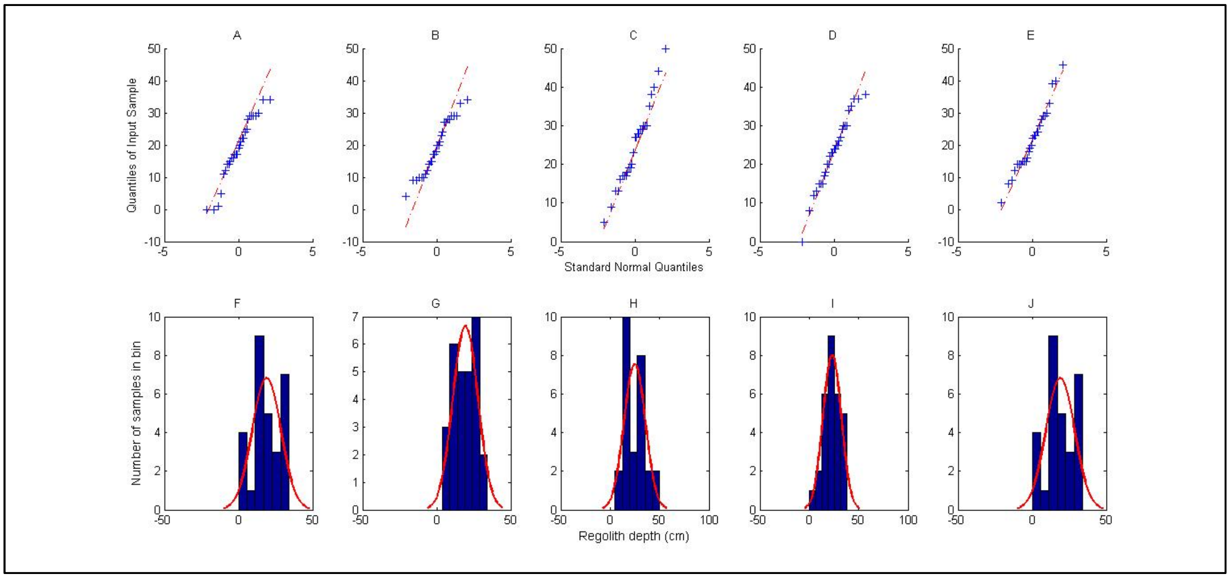

Figure 23: QQ plots and histograms of lower basin regolith depth data separated into populations based on hillslope position. A and F correspond to hilltop positions, B and G correspond to 20% of the hillslope length from the divide, C and H correspond to 40% of the hillslope length from the divide, D and I correspond to 60% of the hillslope length from the divide, and E and J correspond to 80% of the hillslope length from the divide.

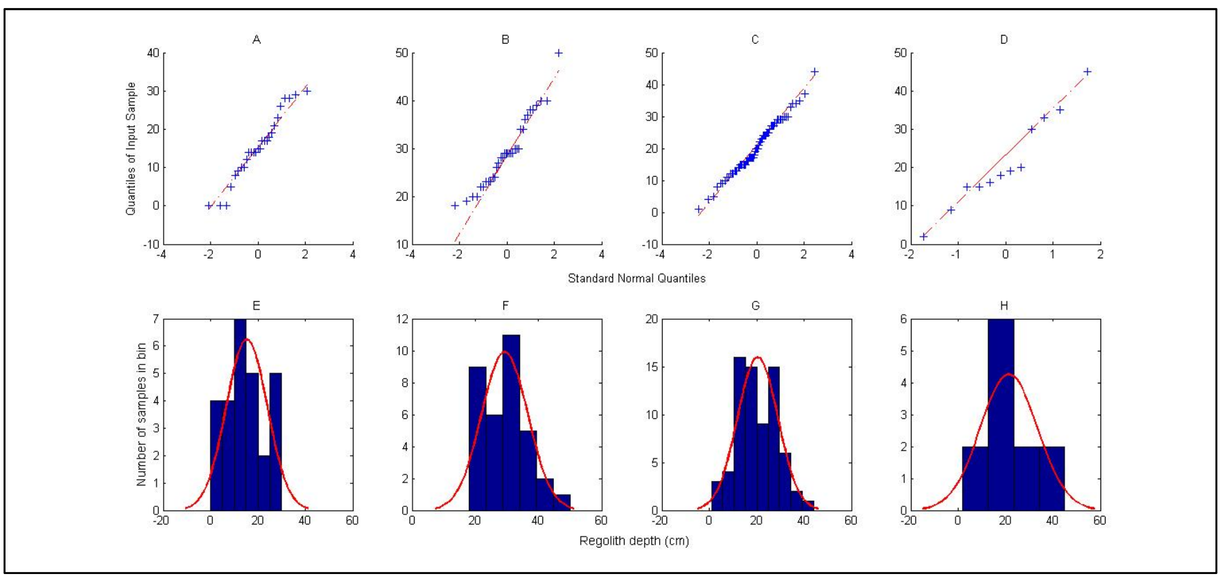

Figure 24: QQ plots and histograms of lower basin regolith depth data separated into populations based on underlying materials. A and E correspond to dedrock, B and F correspond to saprolite, C and G correspond to colluvium, and D and H correspond to mass wasting deposits.

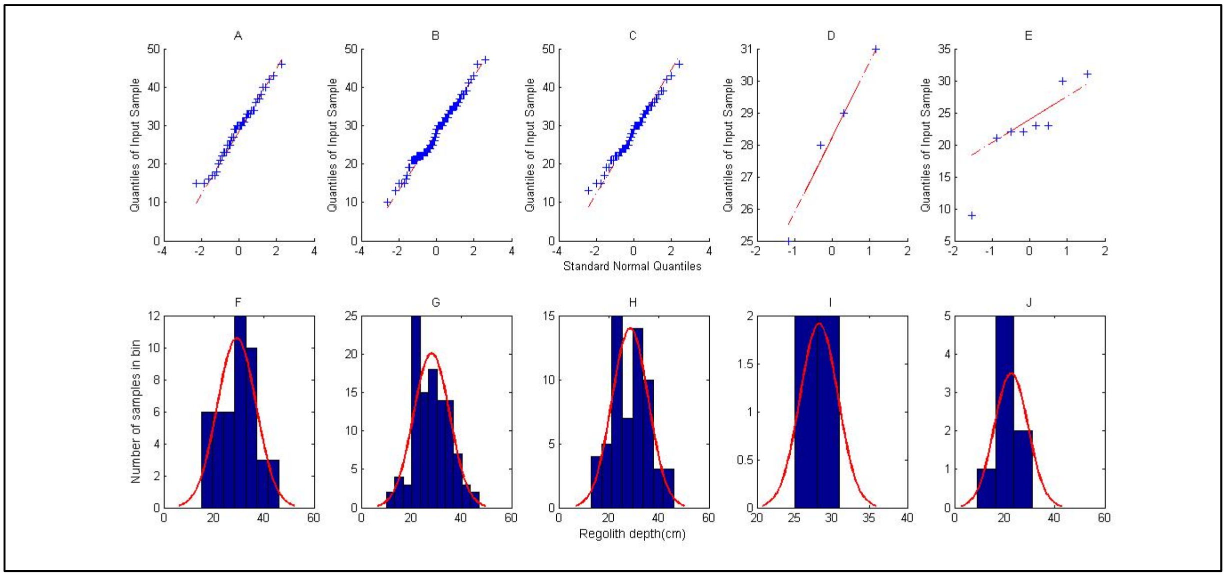

Figure 25: QQ plots and histograms of upper basin regolith depth data separated into populations based on aspect. A and F correspond to North aspects, B and G correspond to east aspects, C and H correspond to South aspects, D and I correspond to West aspects, and E and J correspond to Flat sampling locations.

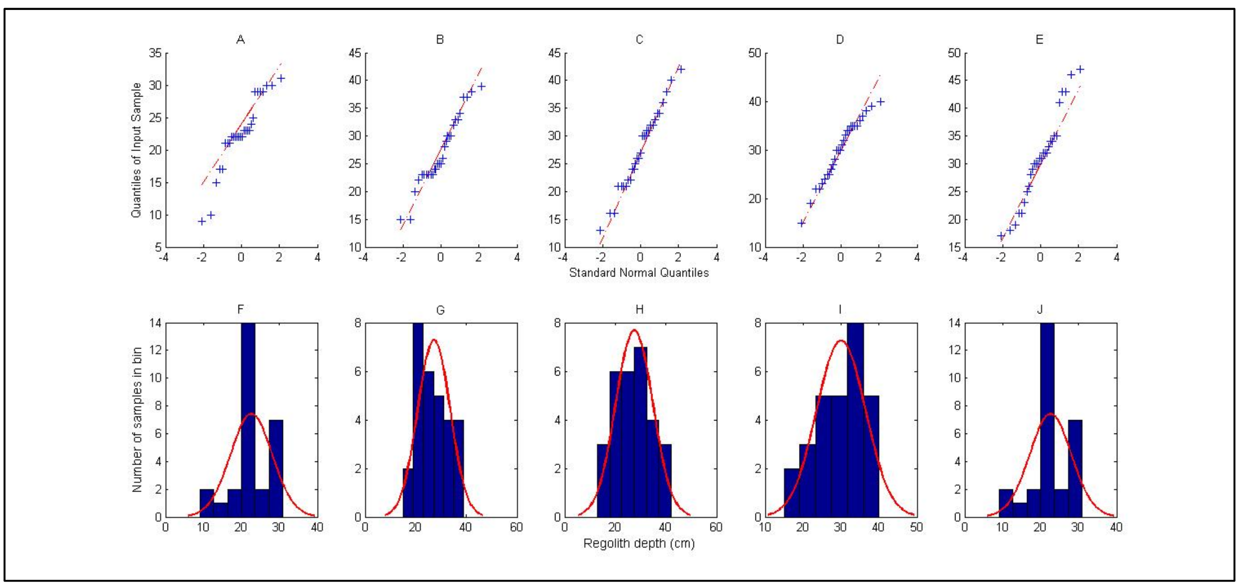

Figure 26: QQ plots and histograms of upper basin regolith depth data separated into populations based on hillslope position. A and F correspond to hilltop positions, B and G correspond to 20% of the hillslope length from the divide, C and H correspond to 40% of the hillslope length from the divide, D and I correspond to 60% of the hillslope length from the divide, and E and J correspond to 80% of the hillslope length from the divide.

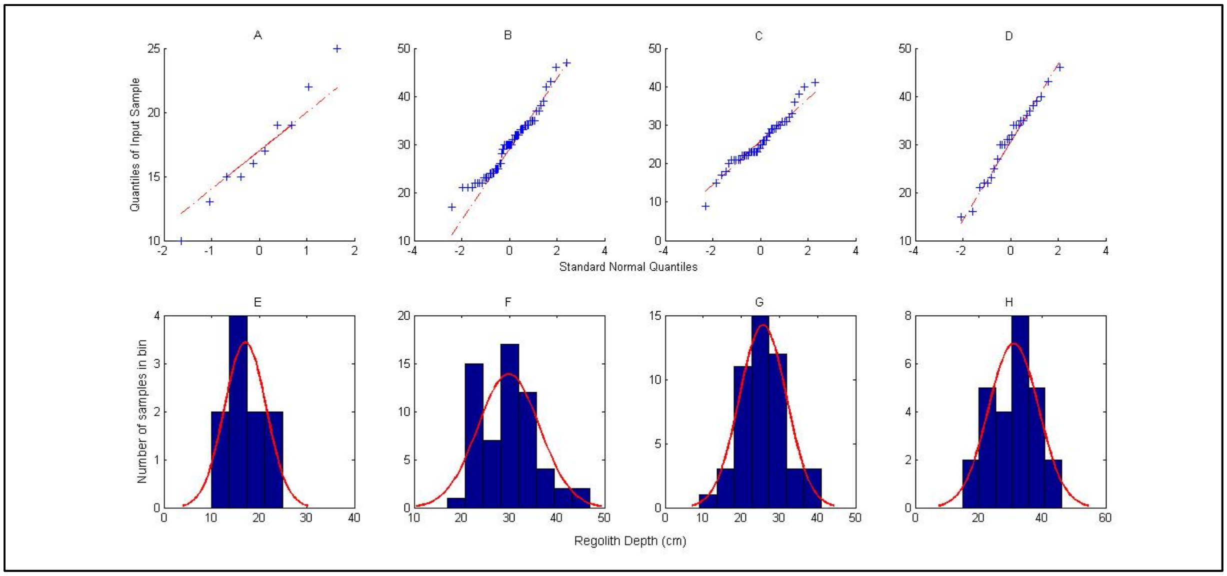

Figure 27: QQ plots and histograms of upper basin regolith depth data separated into populations based on underlying materials. A and E correspond to dedrock, B and F correspond to saprolite, C and G correspond to colluvium, and D and H correspond to mass wasting deposits.

Appendix D Supplemental Morphometric Parameter Data

This appendix contains all of the relevant morphometric characteristics extracted from basins, as well as a MATLAB script used to extract most of the parameters.

Table 28: Table of morphometric parameters measured for each basin, as well as correlation coefficients comparing each parameter to denudation rates for the whole population, as well as the upper and lower basins separately.

	D (mm/kyr)	Mean Hillslope (degs) (GIS)	stdev (degs)	Basin Length (Flowpath)	Basin Length (straight)	RVA (m)	RVA (m) sans protrusions	mean hillslope S(deg)	stdev S (deg)	Area (km^2)	outlet str slope (m/m)	Ksn at outlet	Concavity ratio
BB	21	18.0	6.4	3287	3074	92.1	93.3	17.8	6.5	7.4	0.070	86.1	10.5
BHC	23.9	18.1	7.5	3032	2784	32.2	32.4	18.0	7.5	3.7	0.089	80.2	7.7
WR	33.6	18.5	6.9	4892	4539	62.5	68.2	18.3	7.1	13.6	0.327	529.9	6.1
CC	24.2	21.1	8.1	5055	5055	63.9	64.6	21.0	8.2	6.6	0.056	65.5	4.3
RC	28.8	18.0	6.2	5335	4974	83.4	86.3	17.9	6.2	13.5	0.106	170.7	6.6
BG	19.1	16.7	7.1	3156	3156	33.4	33.7	17.2	7.2	2.7	0.240	188.7	7.2
JG	18.9	18.5	7.0	3791	2381	72.8	74.0	18.2	7.3	5.0	0.049	50.5	16.5
SG	33.8	17.5	7.3	5698	5698	58.4	58.7	17.4	7.3	8.3	0.067	87.1	96.2
SkG	22.9	18.6	8.8	4029	4029	78.8	79.0	18.7	8.9	6.3	0.108	124.3	7.7
GRC	35.7	21.7	9.4	3108	3108	48.8	49.9	21.3	9.9	2.9	0.043	34.9	10.1
	R^2 whole pop	0.139	0.069	0.196	0.280	0.010	0.004	0.105	0.079	0.164	0.010	0.091	0.149
	UB mean	*18.740*	*7.028*	*4320.170*	*4085.136*	*66.824*	*69.0*	*18.6*	*7.1*	*9.0*	*0.129*	*186*	*7.06*
	ubstdev	1.32385	0.793663	1075.393354	1078.578967	23.11741	23.7	1.4	0.8	4.4	0.112	196	2.29
	t stat p val	0.883	0.185	0.603	0.597	0.544	0.483	0.956	0.168	0.129	0.665	0.378	0.300
	upper R	-0.102	-0.169	0.646	0.562	-0.075	0.012	-0.115	-0.163	0.812	0.881	0.904	-0.487
	upper R^2	0.010	0.028	0.417	0.315	0.006	0.000	0.013	0.027	0.660	0.775	0.816	0.238
	low mean	18.582	7.912	3956.354	3674.442	58.451	59.1	18.6	8.1	5.0	0.101	97.1	27.6
	low stdev	1.903	1.095	1051.779	1272.848	18.314	18.4	1.6	1.2	2.4	0.082	61.8	38.6
	lower r	0.574	0.516	0.347	0.532	-0.144	-0.143	0.554	0.522	0.228	-0.545	-0.533	0.518
	lower R^2	0.330	0.267	0.120	0.283	0.021	0.020	0.307	0.272	0.052	0.297	0.284	0.268

Appendix E Bulk Geochemical Data

This appendix contains tables with the trace element and major element concentrations measured from powdered pellets on an X Ray Fluorescence spectroscope at the University of Wyoming Department of Geology and Geophysics.

Table 29: This table contains the major element concentrations measured from the XRF pellets by running a general scan.

	SiO2 (%)	Al2O3 (%)	Na2O (%)	K2O (%)	MgO (%)	CaO (%)	Fe2O3 (%)	P2O5 (%)	Cl (%)	SO3 (%)
12JLGBHFR5-2	68.12	16.86	3.55	5.80	0.86	1.09	2.81	0.27	0.04	0.01
12JLGBHFR3	68.94	16.71	3.33	6.15	0.71	1.12	2.31	0.20	0.03	0.00
12JLGBHFR4	68.82	16.26	3.28	6.16	0.67	1.26	2.58	0.37	0.04	0.01
12JLGBHF06	72.93	14.91	2.85	5.09	0.56	0.88	1.88	0.20	0.03	0.02
12JLGBHF08	71.01	16.06	2.70	5.23	0.79	0.90	2.36	0.20	0.03	0.03
12JLGBHF01	73.45	14.71	2.70	4.79	0.59	0.83	2.07	0.18	0.02	0.02
12JLGBHF09	71.59	15.84	2.72	5.11	0.71	0.76	2.29	0.21	0.03	0.05
12JLGBHF03	71.43	15.79	2.87	5.33	0.66	0.87	2.19	0.19	0.03	0.03
12JLGBHF11	72.58	15.08	3.04	4.76	0.54	0.93	2.03	0.22	0.02	0.02
12JLGBHF02	73.93	14.33	2.81	4.80	0.50	0.86	1.88	0.17	0.02	0.02
12JLGBHF10	72.66	15.14	2.73	4.72	0.66	0.83	2.36	0.18	0.02	0.03
12JLGBHF07	73.56	14.49	2.85	5.09	0.46	0.88	1.82	0.18	0.02	0.01
12JLGBHF04	72.92	14.84	2.87	5.36	0.49	0.90	1.73	0.20	0.03	0.01

Table 30: Trace element Geochemistry of samples taken at Big Horn Flats. R in front of the sample number in the sample name designates rock samples.

	12JLGB HFR5	12JLGB HFR3	12JLGB HFR4	12JLG BHF06	12JLG BHF08	12JLG BHF01	12JLG BHF09	12JLG BHF03	12JLG BHF11	12JLGB HFR3	12JLGB HFR4	12JLG BHF02	12JLG BHF10	12JLG BHF07	12JLG BHF04	
initial mass (g)	4	4	4	3.99	4	4	4	4.01	4	4	4	4	4	4	4	
final mass (g)	5	5	5	4.99	5	5.01	5.01	5.01	5	5	5	5	5.01	5.01	5.01	
	4.696	4.158	4.733	3.708	4.083	4.089	4.079	3.980	4.176	4.158	4.733	3.846	4.370	3.759	3.484	mean LLD (ppm)
Sc (ppm)	<d.l.	<d.l.	<d.l.	<d.l.	<d.l.	<d.l.	<d.l.	<d.l.	<d.l.	<d.l.	<d.l.	<d.l.	<d.l.	<d.l.	<d.l.	3.4
Ti (ppm)	3979.2	3390.1	3484.2	4688.9	4617.4	4765.7	4893.3	4286.8	5851.9	3390.1	3484.2	4988.1	5000.3	4734.6	4443.5	6.0
V (ppm)	27.8	25.2	25.1	24.7	28.3	29.0	33.1	30.3	27.0	25.2	25.1	27.4	32.4	26.0	23.3	4.0
Cr (ppm)	14.7	16.0	19.2	25.6	23.5	31.5	36.4	35.9	31.6	16.0	19.2	30.9	25.1	28.6	28.8	2.5
Mn (ppm)	246.1	129.5	196.7	173.3	192.9	203.5	220.7	207.7	194.7	129.5	196.7	211.9	196.8	205.4	194.5	4.7
Co (ppm)	55.9	42.9	79.9	61.1	36.3	81.5	30.8	42.7	50.8	42.9	79.9	70.5	71.5	86.1	48.7	4.0
Ni (ppm)	8.1	6.4	8.3	6.6	8.9	8.5	8.2	8.2	7.4	6.4	8.3	7.4	9.1	8.3	6.0	2.1
Cu (ppm)	12.4	7.4	7.0	5.9	6.4	6.6	24.8	6.5	9.9	7.4	7.0	6.1	6.2	5.8	5.4	0.8
Zn (ppm)	47.6	36.6	47.5	28.9	35.8	38.6	54.5	35.6	38.4	36.6	47.5	29.7	39.7	29.0	25.3	0.6
Ga (ppm)	16.0	15.3	15.9	13.0	14.5	14.2	14.7	14.6	15.0	15.3	15.9	13.6	15.2	12.6	13.2	0.6
Ge (ppm)	<d.l.	<d.l.	<d.l.	<d.l.	<d.l.	<d.l.	<d.l.	<d.l.	<d.l.	<d.l.	<d.l.	<d.l.	<d.l.	<d.l.	<d.l.	0.7
As (ppm)	38.9	42.1	47.4	47.5	48.8	42.2	42.1	48.4	49.2	42.1	47.4	45.4	47.1	45.2	38.0	5.5
Se (ppm)	7.5	7.7	7.6	8.3	8.6	6.8	7.7	8.5	7.5	7.7	7.6	7.5	7.7	7.6	7.8	1.3
Br (ppm)	5.7	6.6	6.9	6.4	7.7	4.8	6.8	7.9	6.6	6.6	6.9	6.1	6.4	5.3	5.1	1.0
Rb (ppm)	176.6	190.2	230.8	151.8	161.4	162.1	161.6	165.9	158.1	190.2	230.8	155.3	166.9	156.9	154.8	0.6
Sr (ppm)	159.5	151.4	170.8	150.0	151.0	149.0	143.3	151.5	149.4	151.4	170.8	150.7	144.9	153.6	151.3	0.5
Y (ppm)	20.5	18.9	28.2	29.0	23.1	28.0	24.6	23.8	38.9	18.9	28.2	31.8	26.0	32.3	30.8	1.0

Zr (ppm)	286.4	236.0	259.2	451.6	303.3	424.5	393.0	342.7	751.7	236.0	259.2	554.0	405.0	552.0	514.8	0.8
Nb (ppm)	11.2	9.2	12.8	12.3	11.4	13.2	12.4	11.1	15.5	9.2	12.8	14.0	14.3	12.8	11.2	0.7
Mo (ppm)	<d.l.	<d.l.	<d.l.	<d.l.	<d.l.	<d.l.	<d.l.	<d.l.	<d.l.	<d.l.	<d.l.	<d.l.	<d.l.	<d.l.	<d.l.	0.6
Ag (ppm)	20.1	16.8	16.8	19.0	20.4	20.1	19.6	16.6	17.8	16.8	16.8	24.2	19.9	12.3	20.7	4.8
Cd (ppm)	17.2	<d.l.	15.9	13.5	13.6	17.0	17.2	13.5	<d.l.	<d.l.	15.9	18.6	15.0	<d.l.	16.5	5.2
Sn (ppm)	<d.l.	<d.l.	<d.l.	<d.l.	<d.l.	<d.l.	<d.l.	<d.l.	<d.l.	<d.l.	<d.l.	<d.l.	<d.l.	<d.l.	<d.l.	3.1
Sb (ppm)	<d.l.	<d.l.	<d.l.	<d.l.	<d.l.	<d.l.	<d.l.	<d.l.	<d.l.	<d.l.	<d.l.	<d.l.	<d.l.	<d.l.	<d.l.	5.7
Te (ppm)	<d.l.	<d.l.	<d.l.	<d.l.	<d.l.	<d.l.	<d.l.	<d.l.	<d.l.	<d.l.	<d.l.	<d.l.	<d.l.	<d.l.	<d.l.	4.6
I (ppm)	<d.l.	<d.l.	<d.l.	<d.l.	<d.l.	<d.l.	<d.l.	<d.l.	<d.l.	<d.l.	<d.l.	<d.l.	<d.l.	<d.l.	<d.l.	5.1
Cs (ppm)	<d.l.	<d.l.	<d.l.	<d.l.	<d.l.	<d.l.	<d.l.	<d.l.	<d.l.	<d.l.	<d.l.	<d.l.	<d.l.	<d.l.	<d.l.	7.2
Ba (ppm)	1130.9	1083.6	1564.9	1131.2	1123.8	1128.3	1121.8	1197.3	1102.1	1083.6	1564.9	1105.7	1089.4	1176.6	1179.2	12.0
La (ppm)	78.2	57.2	66.5	84.6	65.5	76.8	66.8	70.0	131.4	57.2	66.5	92.5	66.6	91.9	89.6	14.5
Ce (ppm)	165.9	135.5	150.6	167.9	130.4	177.1	159.5	148.4	271.7	135.5	150.6	226.7	177.6	210.9	183.0	21.6
Nd (ppm)	68.9	53.3	60.0	63.3	48.6	67.0	63.3	49.8	102.7	53.3	60.0	93.4	69.5	80.8	72.8	11.6
Sm (ppm)	<d.l.	<d.l.	<d.l.	<d.l.	<d.l.	<d.l.	<d.l.	<d.l.	<d.l.	<d.l.	<d.l.	<d.l.	<d.l.	<d.l.	<d.l.	9.5
Yb (ppm)	<d.l.	<d.l.	<d.l.	<d.l.	<d.l.	<d.l.	<d.l.	<d.l.	<d.l.	<d.l.	<d.l.	<d.l.	<d.l.	<d.l.	<d.l.	3.1
Hf (ppm)	<d.l.	<d.l.	<d.l.	<d.l.	<d.l.	<d.l.	<d.l.	<d.l.	<d.l.	<d.l.	<d.l.	<d.l.	<d.l.	<d.l.	<d.l.	4.5
Ta (ppm)	<d.l.	<d.l.	<d.l.	<d.l.	<d.l.	<d.l.	<d.l.	<d.l.	<d.l.	<d.l.	<d.l.	<d.l.	<d.l.	<d.l.	<d.l.	2.2
W (ppm)	447.0	378.2	784.6	531.2	300.1	750.2	285.9	375.5	487.2	378.2	784.6	661.5	659.1	788.4	486.8	1.9
Tl (ppm)	16.3	17.5	21.9	21.9	20.1	19.0	19.0	22.4	19.7	17.5	21.9	19.8	21.7	20.9	17.6	2.2
Pb (ppm)	39.8	40.7	40.1	38.3	38.0	36.1	36.5	39.7	36.0	40.7	40.1	36.5	35.7	36.7	39.2	1.9
Bi (ppm)	12.8	15.0	14.5	16.1	15.9	13.2	14.8	16.8	12.9	15.0	14.5	13.7	15.7	13.2	13.4	2.2
Th (ppm)	44.7	36.7	35.5	41.5	27.6	38.1	35.6	32.7	55.2	36.7	35.5	47.1	37.4	45.4	43.3	2.5
U (ppm)	<d.l.	<d.l.	<d.l.	<d.l.	<d.l.	<d.l.	9.9	<d.l.	<d.l.	<d.l.	<d.l.	3.7	<d.l.	<d.l.	<d.l.	1.7